THESIS FOR THE DEGREE OF DOCTOR OF PHILOSOPHY

Microscopic Theory of Exciton Dynamics in Two-Dimensional Materials

Samuel Brem

Department of Physics

Chalmers University of Technology

Göteborg, Sweden 2020

Microscopic Theory of Exciton Dynamics in Two-Dimensional Materials
Samuel Brem

ISBN 978-91-7905-391-8

Doktorsavhandlingar vid Chalmers tekniska högskola
Ny serie nr 4858
ISSN 0346-718X

Department of Physics
Chalmers University of Technology
SE-412 96 Göteborg
Sweden
Telephone + 46 (0)31-772 1000

Cover illustration: Artistic impression of momentum-indirect excitons composed of electrons and holes at different valleys of conduction and valence band. Created with the software Blender.

Printed at Chalmers Reproservice
Göteborg, Sweden 2020

Microscopic Theory of Exciton Dynamics in Two-Dimensional Materials
Samuel Brem
Department of Physics
Chalmers University of Technology

Abstract

Transition Metal Dichalcogenides (TMDs) present a giant leap forward towards the realization of nanometer-sized quantum devices. As a direct consequence of their truly two-dimensional character, TMDs exhibit a strong Coulomb-interaction, leading to the formation of stable electron-hole pairs, so-called excitons. These quasi-particles have a large impact on optical properties as well as charge-transport characteristics in TMDs. Therefore, a microscopic understanding of excitonic degrees of freedom and their interactions with other particles becomes crucial for a technological application of TMDs in a new class of optoelectronic and photonic devices. Furthermore, deeper insights into the dynamics of different types of exciton states will open the possibility to explore new quantum effects of the matter-light interaction.
The aim of this thesis is to investigate the many-particle processes governing the ultrafast dynamics of excitons in TMD mono- and bilayers. Based on the density matrix formalism we develop equations describing an interacting system of electrons, phonons and photons, and numerically simulate the time- and momentum-resolved dynamics of excitons in different TMDs.
First, we provide a detailed picture of exciton-light and exciton-phonon interactions with special focus on the impact of momentum-dark exciton states. In particular, we develop and apply quantitative models for the i) broadening of excitonic resonances in linear absorption spectra, ii) formation of side peaks in photoluminescence spectra resulting from phonon-assisted recombination of momentum-dark excitons and iii) dynamical simulations of the formation of bound excitons out of a free electron-hole gas. Then, we investigate how the exciton-light interaction is modified when two TMD monolayers are vertically stacked into homo- and hetero-bilayers. Here we focus on the modification of optical spectra in bilayer systems by controlling the stacking angle. In particular, we iv) show how the interlayer hybridization of momentum-dark excitons can be controlled through the stacking angle and v) investigate how the localization phase of moiré excitons can be tuned. Our theoretical models have allowed us to predict experimentally accessible excitonic characteristics, which have been demonstrated in several joint experiment-theory collaborations including linear absorption, photoluminescence and ultrafast pump-probe experiments. The gained microscopic insights into exciton optics, exciton dynamics and control of exciton phases is expected to contribute to the realization of TMD-based optoelectronic devices.

Keywords: excitons, density matrix formalism, 2D materials, relaxation dynamics, exciton-phonon interaction, van der Waals materials

List of publications

This thesis consists of an introductory text and the following papers:

1. **Exciton Relaxation Cascade in two-dimensional Transition Metal Dichalcogenides**
   S Brem, M Selig, G Berghäuser and E Malic
   Scientific Reports 8: 8238 (2018)

2. **Intrinsic Lifetime of Higher Excitonic States in Tungsten Diselenide Monolayers**
   S Brem, J Zipfel, M Selig, A Raja, L Waldecker, J Ziegler, T Taniguchi, K Watanabe, A Chernikov, E Malic
   Nanoscale 11, 12381-12387 (2019)

3. **Phonon-Assisted Photoluminescence from Indirect Excitons in Monolayers of Transition-Metal Dichalcogenides**
   S Brem, A Ekman, D Christiansen, F Katsch, M Selig, C Robert, X Marie, B Urbaszek, A Knorr, E Malic
   Nano Letters 20 (4), 2849–2856 (2020)

4. **Hybridized Intervalley Moiré Excitons and Flat Bands in Twisted WSe_2 Bilayers**
   S Brem, KQ Lin, R Gillen, JM Bauer, J Maultzsch, JM Lupton, E Malic
   Nanoscale 12, 11088-11094 (2020)

5. **Tunable Phases of Moiré Excitons in van der Waals Heterostructures**
   S Brem, C Linderälv, P Erhart, E Malic
   Nano Letters (2020)
   https://dx.doi.org/10.1021/acs.nanolett.0c03019

   My contribution to the appended papers
   As first-author, I developed the theoretical models, performed the numerical evaluation, analyzed the results and wrote the paper with the help of my main supervisor and other coauthors.

Publications not appended in this thesis:

6. **Microscopic modeling of tunable graphene-based terahertz Landau-level lasers**
   S Brem, F Wendler, E Malic
   Physical Review B 96 (4), 045427 (2017)

7. **Symmetry-breaking supercollisions in Landau-quantized graphene**
   F Wendler, M Mittendorff, JC König-Otto, S Brem, C Berger, WA de Heer, R Böttger, H Schneider, M Helm, S Winnerl, E Malic
   Physical Review Letters 119 (6), 067405 (2017)

8. **Carrier Dynamics in Graphene: Ultrafast Many-Particle Phenomena**
   E Malic, T Winzer, F Wendler, S Brem, R Jago, A Knorr, M Mittendorff, JC König-Otto, T Plötzing, D Neumaier, H Schneider, M Helm, S Winnerl
   Annalen der Physik 529 (11), 1700038 (2017)

9. **Dark excitons in transition metal dichalcogenides**
   E Malic, M Selig, M Feierabend, S Brem, D Christiansen, F Wendler, A Knorr, G Berghäuser
   Physical Review Materials 2 (1), 014002 (2018)

10. **Molecule signatures in photoluminescence spectra of transition metal dichalcogenides**
    M Feierabend, G Berghäuser, M Selig, S Brem, T Shegai, S Eigler, E Malic
    Physical Review Materials 2 (1), 014004 (2018)

11. **Dielectric engineering of electronic correlations in a van der Waals heterostructure**
    P Steinleitner, P Merkl, A Graf, P Nagler, K Watanabe, T Taniguchi, J Zipfel, C Schüller, T Korn, A Chernikov, S Brem, M Selig, G Berghaäuser, E Malic, R Huber
    Nano Letters 18 (2), 1402-1409 (2018)

12. **Electrically pumped graphene-based Landau-level laser**
    S Brem, F Wendler, S Winnerl, E Malic
    Physical Review Materials 2 (3), 034002 (2018)

13. **Impact of strain on the excitonic linewidth in transition metal dichalcogenides**
    Z Khatibi, M Feierabend, M Selig, S Brem, C Linderälv, P Erhart, E Malic
    2D Materials 6 (1), 015015 (2018)

14. **Interlayer exciton dynamics in van der Waals heterostructures**
S Ovesen, S Brem, C Linderälv, M Kuisma, T Korn, P Erhart, M Selig, E Malic
Communications Physics 2 (1), 23 (2019)

15. **Dielectric disorder in two-dimensional materials**
A Raja, L Waldecker, J Zipfel, Y Cho, S Brem, J Ziegler, M Kulig, T Taniguchi, K Watanabe, E Malic, T Heinz, T Berkelbach, A Chernikov
Nature Nanotechnology 14, 832–837 (2019)

16. **Spatio-temporal dynamics in graphene**
R Jago, R Perea-Causin, S Brem, E Malic
Nanoscale 11, 10017-10022 (2019)

17. **Disorder-induced broadening of excitonic resonances in transition metal dichalcogenides**
M Dwedari, S Brem, M Feierabend, E Malic
Physical Review Materials 3, 074004 (2019)

18. **Ultrafast transition between exciton phases in van der Waals heterostructures**
P Merkl, F Mooshammer, P Steinleitner, A Girnghuber, K-Q Lin, P Nagler, J Holler, C Schüller, JM Lupton, T Korn, S Ovesen, S Brem, E Malic, R Huber
Nature Materials 18, 691–696 (2019)

19. **Exciton propagation and halo formation in two-dimensional materials**
R Perea-Causin, S Brem, R Rosati, R Jago, M Kulig, JD Ziegler, J Zipfel, A Chernikov, E Malic
Nano Letters 19 (10), 7317-7323 (2019)

20. **Exciton diffusion in monolayer semiconductors with suppressed disorder**
J Zipfel, M Kulig, R Perea-Causín, S Brem, JD Ziegler, R Rosati, T Taniguchi, K Watanabe, MM Glazov, E Malic, A Chernikov
Physical Review B 101 (11), 115430 (2020)

21. **Negative effective excitonic diffusion in monolayer transition metal dichalcogenides**
R Rosati, R Perea-Causín, S Brem, E Malic
Nanoscale 12, 356-363 (2020)

22. **Suppression of intervalley exchange coupling in the presence of momentum-dark states in transition metal dichalcogenides**
M Selig, F Katsch, S Brem, GF Mkrtchian, E Malic, A Knorr
Physical Review Research 2, 023322 (2020)

23. **Optical fingerprint of bright and dark localized excitonic states in atomically thin 2D materials**

M Feierabend, S Brem, E Malic
Physical Chemistry Chemical Physics 21 (47), 26077-26083 (2020)

24. **Twist-tailoring Coulomb correlations in van der Waals homobilayers**
P Merkl, F Mooshammer, S Brem, A Girnghuber, KQ Lin, L Weigl, M Liebich, CK Yong, R Gillen, J Maultzsch, JM Lupton, E Malic, R Huber
Nature Communications 11 (1), 1-7 (2020)

25. **Microscopic modeling of pump–probe spectroscopy and population Inversion in transition metal dichalcogenides**
R Perea-Causín, S Brem, E Malic
Physica Status Solidi (b), 2000223 (2020)

26. **Criteria for deterministic single-photon emission in two-dimensional atomic crystals**
JJP Thompson, S Brem, H Fang, J Frey, SP Dash, W Wieczorek, E Malic
Physical Review Materials 4, 084006 (2020)

27. **Brightening of spin-and momentum-dark excitons in transition metal dichalcogenides**
M Feierabend, S Brem, A Ekman, E Malic
2D Materials (2020)

28. **Temporal evolution of low-temperature phonon sidebands in WSe_2 monolayers**
R Rosati, S Brem, R Perea-Causín, K Wagner, E Wietek, J Zipfel, M Selig, T Taniguchi, K Watanabe, A Knorr, A Chernikov, E Malic
ACS Photonics (2020)

29. **Strain-dependent exciton diffusion in transition metal dichalcogenides**
R Rosati, S Brem, R Perea-Causín, R Schmidt, I Niehues, S Michaelis de Vasconcellos, R Bratschitsch, E Malic
2D Materials (2020)

30. **Excitation-induced dephasing in 2D materials and van der Waals heterostructures**
D Erkensten, S Brem, E Malic
arXiv preprint 2006.08392 (2020)

31. **Phonon-assisted exciton dissociation in transition metal dichalcogenides**
R Perea-Causin, S Brem, Ermin Malic
arXiv preprint 2009.11031 (2020)

My contributions to the papers
As first-author in Papers 6 and 12, I developed the theoretical model, performed

the numerical evaluation, analyzed the results and wrote the paper with the help of my main supervisor. In Papers 11, 15 and 24 I developed the theoretical model, performed the numerical calculation and analyzed the results as leading theory author. In the other publications I contributed by developing the theoretical model and analyzing/interpreting results during the supervision or in collaboration with the leading theory authors.

CONTENTS

CHAPTER 1

INTRODUCTION

The ongoing miniaturization of electronic technologies has now reached fundamental limitations. Conventional concepts for semiconductor-based devices often break down when the length scale of critical components reaches the nanometre regime, in which quantum effects become dominant. However, a new class of so-called quantum materials presents a chance to overcome these limitations and eventually enable completely new paradigms for information storage and processing, such as spin- and valleytronics [1, 2].

In particular, two-dimensional crystals with the thickness of a few atoms, so-called monolayers, have attracted tremendous attention in research over the last ten years. The groundbreaking experiments on graphene (carbon monolayers) have been awarded with the Nobel prize in 2010 and the subsequent boom in 2D materials research has lead to the discovery of a large library of stable monolayer materials [3–5], including the semiconducting family of transition metal dichalcogenides (TMDs) [6]. The four most studied TMDs are a composite of molybdenum or tungsten with either sulfur or selenium, such as MoS_2, which is displayed in Fig. 1.1. This new class of semiconductors exhibits a variety of outstanding physical properties, which are advantageous not only for technological applications [7–10], but also for fundamental research of correlated quantum systems [11]. Since TMDs are quasi two-dimensional, they exhibit a reduced dielectric screening, which consequently leads to the formation of unusually stable excitons [13–15], i.e. Coulomb-bound electron-hole pairs. These quasi-particles dominate the optical characteristics of TMDs [16–18], so that a microscopic understanding of excitons becomes of crucial importance for TMD-based technologies. Moreover, the large exciton binding energies in TMDs facilitate the study of the exciton Rydberg series and intra-excitonic transitions [19–21], which was technologically

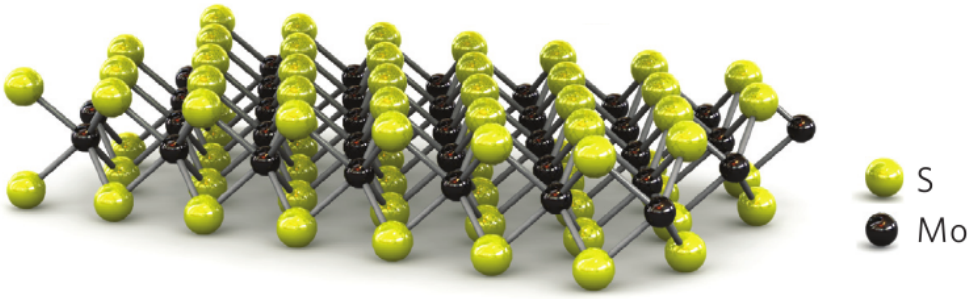

Figure 1.1: Crystal structure of Molybdenum Disulphide monolayers (MoS_2), which where the first TMD monolayers to be discovered. Figure taken from Ref. [12].

limited in conventional platforms used for the study of exciton physics, such as GaAs quantum wells. A detailed theoretical picture of the internal structure of excitons and their scattering channels might enable a controlled manipulation of TMD properties and thereby an entire new class of light emitters and absorbers.

While monolayers alone already exhibit unique properties, the possibility to artificially stack two monolayers into a van der Waals bilayer [22] further extends the playground of many-particle physics. In particular, two monolayers can be stacked with a finite twist-angle between the two crystal orientations, which gives rise to a super periodicity, also known as moiré pattern. Some superlattices exhibit a unique electronic topology leading to interesting quantum effects such as the superconductivity in magic angle bilayer graphene [23, 24]. In TMD bilayers the exceptional exciton physics of monolayers is extended by the emergence of spatially separated electron-hole pairs, also known as interlayer excitons [25–29]. These have been predicted to be captured in potential minima of the periodic moiré pattern created by a twisted bilayer, giving rise to a tunable quantum emitter array [30]. While several pioneering works [31–35] have experimentally confirmed the existence of such moiré excitons, many aspects about the nature of these excitons and the origin of their twist-angle tunability still remain unclear. A microscopic understanding of the excitonic states in play as well as their interaction mechanisms will open up the possibility to tailor excitonic moiré superlattices for optoelectronic applications.

1.1 Outline

The aim of this thesis is to theoretically investigate the many-particle processes governing the properties and dynamics of excitons in TMD mono- and bilayers. To this end, the content of this thesis is divided into two parts. First we focus on excitons in TMD monolayers (Chapter 3-7) and investigate how their properties and dynamics can be probed in optical experiments, such as linear absorption

spectroscopy (Chapter 4), photoluminescence (Chapter 6) and pump-probe experiments (Chapter 7). The aim here is to provide a sophisticated picture of exciton-phonon and exciton-photon interaction mechanisms, starting from the formation of bound excitons out of a free electron-hole gas, up to the eventual radiative decay of different exciton species. Thereby special attention is paid to the impact of momentum-dark intervalley excitons. To theoretically model the dynamics of an interacting system of electrons, phonons and photons we use a density matrix approach, which is gradually introduced throughout Chapter 2-7. This theoretical framework allows us to map the trajectory of excitons through their energy landscape which in turn enables a microscopic interpretation of recent experiments performed on TMDs. In the second part (Chapter 8-10) we apply the knowledge obtained for monolayers to model exciton properties in twisted bilayers. After introducing the concept of intra- and interlayer excitons in Chapter 8, we consider the hybridization of these two exciton species in homobilayers (Chapter 9) as well as the formation of moiré trapped exciton states in type II heterobilayers (Chapter 10). In these sections a special focus lies on the tunability of the exciton properties with the twist-angle and how this affects the optical characteristics of the material.

1.2 Key Outcomes

In the following the major outcomes of the five first-author publications and their impact on coauthored follow-up/side projects is summarized.

Paper 1: In this work, we numerically simulate the momentum-, energy- and time-resolved formation dynamics of excitons. In particular, our model provides insights into the phonon-induced relaxation of an excited electron-hole plasma into bound excitons. We predict an ultrafast relaxation into the 1s ground state on a picosecond timescale and investigate how the optical response at far-infrared frequencies evolves during the formation process. The concepts and numerical methods of this project where improved and extended to model the exciton dynamics and/or pump-probe spectra in several follow-up/side projects, where we investigated heterostructures (Paper 11, 18 and 14) as well as spatially resolved dynamics (Paper 19, 20, 21 and 29). The theoretical approach and central results are presented in Chapter 7.

Paper 2: In this joint experiment-theory study we investigate the broadening of excitonic resonances in linear absorption spectra with special focus on higher order resonances (above the 1s). Here we reveal the underlying microscopic mechanism including radiative decay and exciton-phonon scattering channels across the full Rydberg-like series of excitonic states. The model is supported by temperature-dependent reflectance contrast measurements for hBN-encapsulated WSe_2 provid-

ing the linewidths of the three lowest exciton resonances 1s, 2s and 3s. We show that the linewidth of higher exciton states is comparable to or even smaller than the ground state broadening, although they exhibit a much larger phase space for possible relaxation channels. Our model explains this behaviour with an increase of the exciton Bohr radii for excited states, resulting in a quenched exciton–phonon scattering efficiency. These findings, in combination with further arguments, have lead to the conclusion that the encapsulation of monolayers with hBN leads to a strong reduction of the dielectric disorder (Paper 15) compared to simply exfoliated samples, e.g., on SiO_2 substrates. The theoretical approach and central results are presented in Chapter 4.

Paper 3: In this joint experiment-theory work we model the photoluminescence (PL) signatures of phonon-assisted recombinations of momentum-dark intervalley excitons and compare our results to low-temperature PL experiments. For WSe_2 our model predicts pronounced signals stemming from the phonon-assisted decay of K–K' excitons between 50 and 80 meV below the bright exciton, which is in excellent agreement with the experimental observations. These peaks have been observed in several independent experiments, whereas their microscopic origin has so far remained unclear. In a follow-up project (Paper 28) we investigated the temporal evolution of these phonon sidebands after a pulsed excitation. Here we combined a simulation of the exciton relaxation dynamics with time- and spectrally resolved PL measurements. In good agreement between experiment and theory we find that the phonon sidebands undergo a red shift with time resulting from a thermalization of the optically injected hot exciton population. The theoretical approach and central results are presented in Chapter 6.

Paper 4: In this project, we combine our model with first principle calculations and optical experiments to study layer-hybridized intervalley excitons in twisted bilayer WSe_2. We find that the interlayer hybridization is small at the K point, which gives rise to pure intra- or interlayer excitons. In contrast, electrons at the Λ point are delocalized across both layers, resulting in a strong redshift of the K–Λ exciton compared to monolayers, as well as the emergence of flat moiré bands at small twist-angles. In agreement between experiment and theory, we show twist-angle dependent PL signatures stemming from the phonon-assisted recombination of the layer hybridized K–Λ exciton. In a parallel project we also investigated how the intraexcitonic 1s-2p transition of the K-Λ exciton changes with the twist-angle (Paper 24), where we show that the intra-/interlayer exciton character of the hybrid can be tuned with the stacking angle. The theoretical approach and central results are presented in Chapter 9.

Paper 5: In this work, we combine our theory with first principles calculations to model properties of moiré excitons in a twisted $MoSe_2/WSe_2$ heterostructure. Here, we calculate how the properties of intra- and interlayer excitons are modi-

fied by the potential created through the moiré pattern and investigate how the optical response changes accordingly. For small twist-angles $< 2°$, we predict the emergence of flat exciton bands for both intra- as well as interlayer excitons corresponding to an array of moiré trapped emitters. Moreover, we show that the degree of localization quickly changes with increasing twist-angle, so that already at $3°$ only delocalized excitons exist. We show that multiple moiré resonances appear in the absorption spectrum and that their spectral shift behaviour with increasing twist-angle is different for the trapped or delocalized exciton phase. The theoretical approach and central results are presented in Chapter 10.

The gained microscopic insights into the optics and dynamics of bright and dark excitons in TMD mono- and bilayers contribute to a better understanding of these technologically promising quantum materials.

CHAPTER 2

GENERAL THEORY FOR MANY-PARTICLE QUANTUM SYSTEMS

In the following section we introduce the general theoretical framework applied throughout this thesis. In the first part the many-particle density matrix approach is introduced and discussed. The second part focuses on the approximations used in this work to reduce the mathematical complexity of the problem. In principle the shown framework can be applied to model the excitation kinetics of an arbitrary system of interacting electrons, phonons and photons.

2.1 Canonical Quantization

In order to describe the quantized interaction between different degrees of freedom in condensed matter, we have to use a theoretical model unifying the different properties of light (photons), electrons and lattice vibrations (phonons). The quantum field theory has proven to be a powerful tool for treating many-particle problems in condensed matter [36–39]. Here, the canonical quantization scheme is used to transform classical field theories into a many-particle quantum theory, by replacing Poisson brackets with commutators/anti-commutators.

Photons

To obtain a quantized theory of the electromagnetic field in Coulomb gauge ($\nabla \cdot \mathbf{A} = 0$) the vector potential $\mathbf{A}$ is transformed to an operator acting on wave

functions in Fock space [40],

$$\mathbf{A}(\mathbf{r},t) \longrightarrow \hat{\mathbf{A}}(\mathbf{r},t) = \sum_{\sigma\mathbf{k}} \sqrt{\frac{\hbar}{2\epsilon_0 L^3 \omega_k}} \mathbf{e}_{\sigma\mathbf{k}} c_{\sigma\mathbf{k}}(t) e^{i\mathbf{kr}} + \text{h.c.} \tag{2.1}$$

Here $c^{(\dagger)}_{\sigma\mathbf{k}}$ annihilates (creates) a photon in mode σ, wavevector $\mathbf{k}$, polarization $\mathbf{e}_{\sigma\mathbf{k}}$ and frequency $\omega_k = ck$. From the fundamental commutation relation, $[x,p] = i\hbar$ generalized to field coordinate and field momentum [41] we find the bosonic properties of the photon

$$[c_{\sigma\mathbf{k}},c_{\sigma'\mathbf{k}'}] = [c^\dagger_{\sigma\mathbf{k}},c^\dagger_{\sigma'\mathbf{k}'}] = 0; \quad [c_{\sigma\mathbf{k}}(t),c^\dagger_{\sigma'\mathbf{k}'}(t)] = \delta_{\sigma\sigma'}\delta_{\mathbf{k}\mathbf{k}'} \tag{2.2}$$

Moreover, the Hamiltonian of the electromagnetic field obtains the convenient form

$$H = \int d^3r [\frac{1}{2}\epsilon_0 (\partial_t \hat{\mathbf{A}})^2 + \frac{1}{\mu_0}(\nabla \times \hat{\mathbf{A}})^2] \tag{2.3}$$

$$= \sum_{\sigma\mathbf{k}} \hbar\omega_k (c^\dagger_{\sigma\mathbf{k}} c_{\sigma\mathbf{k}} + \frac{1}{2}) \tag{2.4}$$

Hence, each mode of the electromagnetic field can be interpreted as a harmonic oscillator with a quantized energy given by the integer number of photons $\langle c^\dagger_{\sigma\mathbf{k}} c_{\sigma\mathbf{k}} \rangle$ in that mode. The dispersion of photons $\omega_k = c|\mathbf{k}|$ (so called light cone) is determined by the light velocity c.

Phonons

Similar to the electromagnetic field, we can quantize the collective vibrations of lattice atoms in a crystal. The motion within a lattice of N interacting atoms can be described with the classical Hamiltonian [40],

$$H = \sum_{i=1}^{N} \frac{\mathbf{p}_i^2}{2M} + \sum_{i,j} \mathbf{u}_i \cdot \underline{\Theta}^{ij} \cdot \mathbf{u}_j, \tag{2.5}$$

where $\mathbf{p}_i$ is the momentum of the ith atom and $\mathbf{u}_i$ is a small deviation from its rest position $\mathbf{R_i}$. The dynamical matrix $\underline{\Theta}^{ij}$ contains the forces between all particles resulting from the repulsion of their nuclei and the attraction mediated by the core and valence electrons. By diagonalizing the dynamical matrix, we can find the collective eigenmodes $(\alpha, \mathbf{q})$ of the system, which are subsequently quantized,

$$\mathbf{u}_i(t) \longrightarrow \hat{\mathbf{u}}_i(t) = \sum_{\alpha\mathbf{q}} \sqrt{\frac{\hbar}{2MN\Omega_{\alpha\mathbf{q}}}} \mathbf{e}_{\alpha\mathbf{q}} b_{\alpha\mathbf{q}}(t) e^{i\mathbf{q}\mathbf{R}_i} + \text{h.a.} \tag{2.6}$$

in terms of phonon operators $b_{\alpha\mathbf{q}}$, creating or annihilating energy quanta of size $\hbar\Omega_{\alpha\mathbf{q}}$ in the respective mode. The phonon mode α characterizes in which direction

and relative phase the atoms oscillate, e.g. acoustic/optical phonon and longitudinal/transverse mode. The corresponding commutation relations and the form of the quantized Hamiltonian are completely analogue to the case of photons and read,

$$H = \sum_{\alpha\mathbf{q}} \hbar\Omega_{\alpha\mathbf{q}}(b^\dagger_{\alpha\mathbf{q}} b_{\alpha\mathbf{q}} + \frac{1}{2}) \tag{2.7}$$

$$[b_{\alpha\mathbf{q}},b_{\alpha'\mathbf{q}'}] = [b^\dagger_{\alpha\mathbf{q}},b^\dagger_{\alpha'\mathbf{q}'}] = 0 \quad \text{and} \quad [b_{\alpha\mathbf{q}}(t),b^\dagger_{\alpha'\mathbf{q}'}(t)] = \delta_{\alpha\alpha'}\delta_{\mathbf{q}\mathbf{q}'} \tag{2.8}$$

Electrons in Second Quantization

For the description of interactions between, e.g., light and matter, it is convenient to express the electronic part of the system in terms of creation and annihilation operators as well. Moreover, many-particle quantum theories for massive particles have to take into account the Pauli exclusion principle. While systems of two or three particles might be treated by using anti-symmetric products of single particle wave functions, the Schrödinger equation of 10^9 particles (typical excitation number per cm^2 in a semiconductor) is simply not manageable. However, we can find a similar field theoretical description of electrons as for phonons and photons, by treating the Schrödinger equation as a classical field theory, to which the canonical quantization scheme is applied. Choosing a "classical" Hamiltonian [42],

$$H = \int d^3r \Psi^*(\mathbf{r},t)[-\frac{\hbar^2}{2m_0}\Delta + V(\mathbf{r})]\Psi(\mathbf{r},t), \tag{2.9}$$

directly yields the Schrdinger equation (and its complex conjugate) as the corresponding equation of motion with Ψ as generalized field coordinate and $i\hbar/2\Psi^*$ as field momentum. The quantization now follows from defining field operators $\Psi \to \hat{\Psi}$ with fermionic anti-commutators to obey the Pauli principle,

$$\{\hat{\Psi}(\mathbf{r},t),\hat{\Psi}^\dagger(\mathbf{r},t)\} = \delta(\mathbf{r}-\mathbf{r}') \tag{2.10}$$

$$\{a_n(t),a^\dagger_m(t)\} = \delta_{nm} \tag{2.11}$$

Here the second line is obtained when expanding the field operator $\hat{\Psi} = \sum \phi_n a_n$ in terms of an orthogonal basis $\{\phi_n\}$. From Eq. 2.9 we can directly deduce a transformation rule for Hamiltonians in second quantization for a given single particle Hamiltonian $h_1(\mathbf{r})$ in first quantization:

$$H = \sum_{nm} \langle n|h_1|m\rangle a^\dagger_n a_m \tag{2.12}$$

If we choose the eigenstates of the single particle Hamiltonian with eigenenergies ε_i as basis, the electronic Hamiltonian becomes equivalent to phonons and photons

reading

$$H = \sum_i \varepsilon_i a_i^\dagger a_i. \tag{2.13}$$

Here the quantum index i is in general a compound index, containing multiple degrees of freedom, such as momentum and spin for free electrons, and further quantum numbers such as band and valley for electrons in a crystal. Further details about the canonical quantization scheme can be found in the standard literature about quantum field theory and many-particle physics [40, 43].

2.2 Interaction Mechanisms

Based on the quantization scheme for electrons, phonons and photons described above, we can now determine interaction Hamiltonians in second quantization.

Coulomb Interaction

The quantized version of the Coulomb interaction between two electrons can be obtained in a similar manner as the single particle Hamiltonian by including non-local contributions to the action [42]. Here we obtain:

$$H = \frac{1}{2} \sum_{ijkl} V_{ijkl} a_i^\dagger a_j^\dagger a_k a_l \tag{2.14}$$

With the Coulomb matrix element,

$$V_{ijkl} = \int d^3r \int d^3r' \phi_i^*(\mathbf{r}) \phi_j^*(\mathbf{r}') V(\mathbf{r} - \mathbf{r}') \phi_k(\mathbf{r}') \phi_l(\mathbf{r}). \tag{2.15}$$

Here the classical Coulomb potential V is usually modified by a material specific screening function to describe the interaction between electrons in a solid (Sec. 3.4).

Electron-Light Interaction

Starting point for the description of matter-light interactions in second quantization is the single particle Hamiltonian. The interaction of an electron with an external classical electromagnetic field can be introduced into the Schrödinger equation via the so called minimal coupling. Here, we replace the kinetic momentum $\mathbf{p}$ with the generalized momentum $\mathbf{p} + e_0\mathbf{A}$ in the Hamiltonian introducing

the Lorentz force in classical equations of motion. Hence, we find

$$H = \frac{(\mathbf{p} + e_0\mathbf{A})^2}{2m_0} = \frac{\mathbf{p}^2}{2m_0} + \frac{e_0}{2m_0}(\mathbf{p}\cdot\mathbf{A} + \mathbf{A}\cdot\mathbf{p}) + \frac{e_0^2}{2m_0}\mathbf{A}^2, \tag{2.16}$$

where e_0 and m_0 denote the elementary charge and electron rest mass, respectively. Next we perform a dipole approximation, assuming that the vector potential only weakly varies on the length scale of the considered quantum system. For the treatment of electrons in a crystal, this approximation is good as long as the light wavelength is large compared to the unit cell. Hence, we neglect the spatial dependence of the vector potential $\mathbf{A}$. Furthermore, for weak excitations the last term in Eq. 2.16 can be neglected (linear optics regime). Finally, in the considered Coulomb gauge ($\nabla\mathbf{A}$=0) the vector potential commutes with $\mathbf{p}$ and we find the electron light interaction via

$$h_{\text{el-l}} = \frac{e_0}{m_0}\mathbf{A}\cdot\mathbf{p} \longrightarrow H_{\text{el-l}} = \frac{e_0}{m_0}\sum_{nm}\mathbf{A}\cdot\mathbf{M}_{nm}a_n^\dagger a_m, \tag{2.17}$$

where we have used the transformation rule Eq. 2.12 and the definition $\mathbf{M}_{nm} = -i\hbar\langle n|\nabla|m\rangle$. A fully quantized electron-photon interaction is now obtained by expanding the vector potential in terms of photon operators, cf. Eq. 2.1, which yields

$$H_{\text{el-pt}} = \sum_{nm,\sigma\mathbf{k}} \tilde{M}^{nm}_{\sigma\mathbf{k}} a_n^\dagger a_m c_{\sigma\mathbf{k}} + \text{h.c.}, \tag{2.18}$$

$$\text{with} \quad \tilde{M}^{nm}_{\sigma\mathbf{k}} = \frac{e_0}{m_0}\sqrt{\frac{\hbar}{2\epsilon_0 L^3\omega_k}}\mathbf{e}_{\sigma\mathbf{k}}\cdot\mathbf{M}_{nm} \tag{2.19}$$

The interpretation of the Hamiltonian is quite intuitive: the creation (emission) or annihilation (absorption) of a photon is accompanied by the transition of an electron between two states. Here, the electron-photon matrix element g, which is often referred to as oscillator strength, determines how strong a certain transition couples to the light field. While momentum conservation is implicitly included in the matrix element, the energy conservation results from resonance conditions in the equations of motion. However, it is often useful to restrict the summation in Eq. 2.18 to transitions which do not strongly violate energy conservation (rotating wave approximation).

Electron-Phonon Interaction

A similar interaction Hamiltonian as for photons can be derived for electrons and phonons. However, here the interaction term is derived from the change in the electronic energies induced by distortions of the lattice potential accompanying the vibration of the crystal. Therefore the electron-phonon matrix is strongly material

specific and one usually finds a much more complex spectrum of phonon modes than for photons. The calculation of material realistic coupling parameters between electrons and phonons requires sophisticated computational methods, such as the density functional perturbation theory (DFPT). However, the general form of the interaction Hamiltonian can be obtained by assuming that the electrostatic potential of the resting crystal lattice can be decomposed into atomic potentials $V^0_{\text{lattice}}(\mathbf{r}) = \sum_i v_{\text{atom}}(\mathbf{r} - \mathbf{R}_i)$. Hence the time dependent potential of the weakly vibrating lattice is approximated via

$$V_{\text{lattice}}(\mathbf{r},t) = V^0_{\text{lattice}}(\mathbf{r}) - \sum_i \nabla v_{\text{atom}}(\mathbf{r} - \mathbf{R}_i) \cdot \mathbf{u}_i(t) \tag{2.20}$$

with small deviations $\mathbf{u}_i$ of the atoms from their rest positions $\mathbf{R}_i$. While the first term in Eq. 2.20 is already included in the electronic eigenenergies, the second part represents the electron-phonon Hamiltonian in first quantization. To transfer this term into a fully quantized version, we use the expansion of $\mathbf{u}_i$ in terms of phonons, cf. Eq. 2.6, and apply the transformation rule Eq. 2.12 yielding

$$H_{\text{el-ph}} = \sum_{nm,\alpha\mathbf{q}} D^{nm}_{\alpha\mathbf{q}} a^\dagger_n a_m (b_{\alpha\mathbf{q}} + b^\dagger_{\alpha,-\mathbf{q}}) \tag{2.21}$$

$$\text{with} \quad D^{nm}_{\alpha\mathbf{q}} = i\sqrt{\frac{\hbar}{2MN\Omega_{\alpha\mathbf{q}}}}\mathbf{q} \cdot \mathbf{e}_{\alpha\mathbf{q}} \tilde{v}_{\text{atom}}(\mathbf{q}) \mathcal{F}_{nm}(\mathbf{q}). \tag{2.22}$$

Note that the above matrix element only holds for a simple crystal with one atom per unit cell. Moreover, the effective lattice potential seen by the electron in a many-particle system can also depend on its quantum numbers n. However, the above outlined derivation nicely illustrates the origin of this interaction mechanism and yields the right form of the electron-phonon coupling. For a quantitatively realistic matrix element in TMDs we will later resort to first principle calculations from literature.

2.3 Many-Particle Dynamics

Within the above described formalism, we can now derive the dynamics of an interacting system of electrons, phonons and photons. In particular, we are interested in the theoretical modelling of optical experiments performed on solid state systems, i.e. very large many-particle systems. Throughout this work we show how certain observables in experiments can be related to expectation values of different operator combinations.

Density Matrix Formalism

The expectation value of an observable A with respect to a pure quantum state $|\Psi\rangle$ can be expressed with the projection operator $\hat{P}_\Psi = |\Psi\rangle\langle\Psi|$

$$\langle A\rangle = \langle\Psi|A|\Psi\rangle = \sum_n \langle n|\hat{P}_\Psi A|n\rangle = \mathrm{Tr}(\hat{P}_\Psi A). \tag{2.23}$$

However, since it is practically impossible to determine the exact quantum state of all particles in the universe, we need to apply a mixture of thermodynamic statistics and quantum statistics. Here, each possible quantum states $|i\rangle$ can occur with a classical probability p_i. The expectation value of observables with respect to such a mixed state is then determined by the density matrix $\hat{\varrho}$ via

$$\langle A\rangle = \sum_i p_i \langle\Psi_i|A|\Psi_i\rangle = \mathrm{Tr}(\hat{\varrho}A). \tag{2.24}$$

Throughout this work, we apply the framework of the density matrix theory to describe particles in solid [44]. Thereby, we use the above definition of expectation values. Moreover, we use the Heisenberg picture, in which the evolution of a quantum system is described by time-dependent operators. Thereby the properties of the density matrix, e.g. if it contains certain coherences or many-particle correlations, only become apparent in an indirect way, e.g. when we factorize expectation values involving certain operator combinations.

Equations of Motion and Hierarchy Problem

To obtain the time evolution of an observable, we apply the Heisenberg equation of motion to the expectation value of the corresponding operator $\mathcal{O}$,

$$i\hbar\partial_t\langle\mathcal{O}\rangle = \langle[\mathcal{O},H]\rangle \tag{2.25}$$

Thereby all relevant operator combinations can be classified by the number of particle creations and annihilations they involve [37], i.e.

$$\mathcal{O}\{N\} = \beta_1^\dagger..\beta_n^\dagger\alpha_1^\dagger..\alpha_m^\dagger\alpha_1..\alpha_m\beta_1..\beta_l, \quad N = n+m+l. \tag{2.26}$$

Here α and β represent an arbitrary fermion and boson operator respectively. Note that the generic operator above can contain single creation or annihilation of bosons, while each creation of a fermion is accompanied by an annihilation, e.g. $\mathcal{O}\{1\} = \alpha^\dagger\alpha$. This restriction results from the fact that our Hamiltonian only contains processes which conserve the total number of fermions (canonical ensemble). If we now apply the equation of motion to an N-particle operator, the presence of many-particle interactions induces a coupling to an (N+1)-operator.

In turn, the equation of motion for (N+1)-operators couple to (N+2)-operators and so forth, giving rise to an infinite hierachy of coupled equations. If we for example want to determined the dynamics of the occupation of a certain fermionic state $|n\rangle$ the electron-phonon contribution yields

$$\partial_t \langle a_i^\dagger a_i \rangle \Big|_{\text{el-ph}} = \frac{2}{\hbar} \sum_{j,\mathbf{q}} \text{Im} \Big\{ D_{\mathbf{q}}^{ij} \langle a_i^\dagger a_j (b_{\mathbf{q}} + b_{-\mathbf{q}}^\dagger) \rangle \Big\}, \tag{2.27}$$

which connects an electronic single particle observable, to a mixed electron-phonon expectation value involving two particles. The equation of motion for $\langle a_i^\dagger a_j b_{\mathbf{q}} \rangle$ further couples to even more complex expectation values and so on. In order to solve the equations of motion of a many-particle system, we therefore need a systematic approach to truncate the hierarchy problem.

Cluster Expansion Approach

An effective way to treat the hierarchy problem is the cluster expansion scheme. Here many-particle expectation values are factorized into products of lower order expectation values and corresponding correction terms, which are a measure for the particle correlations in the system. As an example, a two-particle expectation value $\langle \mathcal{A}\{1\}\mathcal{B}\{1\} \rangle$ would be factorized into single-particle expectation values (singlets) via $\langle \mathcal{A}\mathcal{B} \rangle = \langle \mathcal{A} \rangle \langle \mathcal{B} \rangle + \delta \langle \mathcal{A}\mathcal{B} \rangle$, where $\delta \langle \mathcal{A}\mathcal{B} \rangle$ can be seen as a measure of the correlation between particle $\mathcal{A}$ and particle $\mathcal{B}$. The expansion of an arbitrary N-particle expectation value $\langle N \rangle$ is obtained recursively via [37, 39, 45, 46]

$$\langle 2 \rangle = \sum_\sigma (-1)^{\sigma_f} P_\sigma \langle 1 \rangle \langle 1 \rangle + \delta \langle 2 \rangle \tag{2.28}$$

$$\langle 3 \rangle = \sum_\sigma (-1)^{\sigma_f} P_\sigma \langle 1 \rangle \langle 1 \rangle \langle 1 \rangle + \sum_\sigma (-1)^{\sigma_f} P_\sigma \langle 1 \rangle \delta \langle 2 \rangle + \delta \langle 3 \rangle \tag{2.29}$$

$$\langle N \rangle = f(\langle 1 \rangle, \delta \langle 2 \rangle, ..., \delta \langle N \rangle), \tag{2.30}$$

where the sum symbolizes the summation over all unique factorizations of permuted operator sequences and σ_f denotes the number of involved permutations of fermionic operators. An important cluster expansion is the so-called Hartree-Fock factorization for electronic operators a:

$$\langle a_1^\dagger a_2^\dagger a_3 a_4 \rangle = \langle a_1^\dagger a_4 \rangle \langle a_2^\dagger a_3 \rangle - \langle a_1^\dagger a_3 \rangle \langle a_2^\dagger a_4 \rangle + \delta \langle a_1^\dagger a_2^\dagger a_3 a_4 \rangle \tag{2.31}$$

In principle, the above shown expansion does not represent an approximation and the hierarchy problem will now appear in terms of many-particle correlations. However, in this framework we can now systematically truncate the system of equations by consistently neglecting particle correlations of a certain order. If we

for example only take into account single particle expectations values and neglect all appearing correlations, we obtain an effective mean field theory, such as the Hartree-Fock-approximation of the Coulomb interaction. When further accounting for two-particle correlations, we can add contributions describing particle scattering as well as the formation of bound particle configurations, such as excitons. Depending on which particles are involved in a certain expectation value, there are macroscopic observables which can be used to assess the accuracy of a certain approximation order. For example, the emergence of biexcitons can be neglected, as long as the excitation density is small compared to $1/a_B^2$, where a_B is the excitons Bohr radius. Moreover, the formation of polarons/polaritons can be neglected in the weak coupling regime, i.e. when the coupling strength is small compared to the lifetime of the phonon/photon.

Markov Approximation

In addition to the cluster expansion, we can further reduce the number of relevant equations of motion by using approximated analytical solutions for many-particle correlations. One frequently used approach in the treatment of interacting open quantum systems is the Markov approximation. Here non-linearities resulting from quantum memory effects are neglected to obtain adiabatic solutions describing energy conserving scattering. In this thesis the Markov-approximation is referred to as a specific mathematical step. The generic form of a Heisenberg equation of motion reads

$$\partial_t \mathcal{X}(t) = (i\omega_0 - \gamma)\mathcal{X}(t) + \mathcal{S}(t), \tag{2.32}$$

which has the formal solution

$$\mathcal{X}(t) = \mathcal{X}(t_0)e^{(i\omega_0-\gamma)(t-t_0)} + \int_{t_0}^{t} d\tau \mathcal{S}(\tau)e^{(i\omega_0-\gamma)(t-\tau)} \tag{2.33}$$

$$= \int_0^{\infty} d\tau \mathcal{S}(t-\tau)e^{(i\omega_0-\gamma)\tau} \tag{2.34}$$

where the second line results from setting the initial time to $t_0 \longrightarrow -\infty$, so that we can neglect the first term of Eq. 2.33, assuming a fast decay of the initial value of $\mathcal{X}$. Now we assume that the source terms $\mathcal{S}$ can be split into an oscillation with a characteristic frequency ω_s and a slowly varying envelope $\tilde{\mathcal{S}}$. Hence we find [47]

$$\mathcal{X}(t) = \int_0^{\infty} d\tau \tilde{\mathcal{S}}(t-\tau)e^{[i(\omega_0-\omega_s)-\gamma]\tau + i\omega_s t} \tag{2.35}$$

$$= \tilde{\mathcal{S}}(t)e^{i\omega_s t}\int_0^{\infty} d\tau e^{[i(\omega_0-\omega_s)-\gamma]\tau} = \frac{\mathcal{S}(t)}{\gamma - i(\omega_0-\omega_s)}. \tag{2.36}$$

The Markov approximation has been performed in Eq. 2.36, where $\tilde{\mathcal{S}}(t-\tau)$ was pulled out of the integral and approximated by its value at the current time.

Here we assume that memory effects are negligible and $\mathcal{X}$ adiabatically follows the source term. This step is however only good if $\tilde{\mathcal{S}}$ varies slowly compared to the correlation life time $1/\gamma$.

The decay rate γ is often included phenomenologically, assuming that the coupling to higher order correlations is well described as a damping term. It is often beneficial to consider the limiting case $\gamma \to 0$, claiming exact resonance for the interaction between system ω_0 and bath ω_s. Here the integral identity,

$$\frac{1}{\omega \pm i\gamma} \longrightarrow \mathcal{P}(\frac{1}{\omega}) \mp i\pi\delta(\omega), \tag{2.37}$$

is applied. Usually, the first term containing the principal value of an integral is related to many-particle induced energy-renormalizations, which are usually divergent and require a self-consistent treatment. Throughout this work, we neglect those renormalizations assuming a system close to the equilibrium and only consider the terms resulting from the imaginary part, which usually reflects scattering rates.

CHAPTER 3

TRANSITION METAL DICHALCOGENIDES AND MODEL HAMILTONIAN

In the following section we consider the optical and electronic properties of TMD monolayers, which are relevant for this thesis. In particular we derive the mathematical framework used to include the material specific properties such as the band structure and interaction matrix elements introduced in Sec. 2.

3.1 Crystal Geometry and Electronic Structure

TMD monolayers are composed by a central plane of transition metal atoms (often Mo or W) sandwiched by two planes of chalcogen atoms (S or Se), which are covalently bond to the neighbouring metal atoms [48], cf. Fig. 3.1. In a top view, the atoms are arranged in a hexagonal honeycomb lattice with alternating atomic species on the lattice sites.

The corresponding hexagonal Brillouin zone of the reciprocal lattice is displayed in the inset of Fig. 3.1b showing the definition of relevant high symmetry points. There are two nonequivalent corners of the Brillouin zone denoted K and K', as well as six different Λ points. Moreover, Fig. 3.1b shows a sketch of the typical electronic band structure in TMD monolayers [49]. In particular, TMDs exhibit a direct electronic band gap at the K point [49] which shows a significant splitting between differently spin-polarized bands. This results from the large magnetic momentum of the transition metal d-orbitals constituting the corresponding Bloch

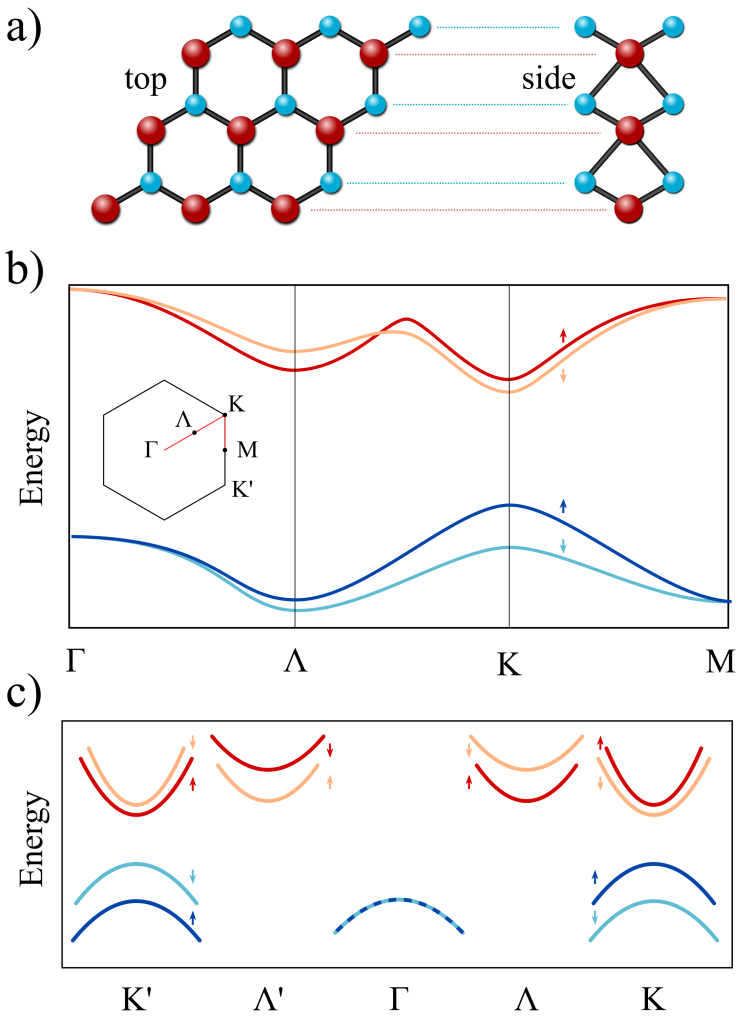

Figure 3.1: Overview of crystal properties in TMDs. a) top and side view of the hexagonal lattice structure. A layer of transition-metal atoms (blue) is sandwiched by two layers of chalcogen atoms (red). b) Sketch of the typical dispersion of valence and conduction band in TMD monolayers [49] along a high-symmetry path in the first Brillouin zone (inset). c) Sketch of the effective mass model of the electronic structure in vicinity of band extrema.

waves. Interestingly, as a result of time-reversal symmetry, the energetic ordering of the spin-split bands is inverted at K and K' (-K) points. The ordering of spin-polarized bands in Fig. 3.1b corresponds to the situation found in tungsten-based TMDs, while the two conduction bands are flipped in molybdenum-based materials. Together with the special optical selection rules discussed in Sec. 3.2 the large spin-orbit coupling facilitates the optical excitation of spin- and valley polarized excitons in TMDs [50–54]. Apart from the K point, there is another local minimum of the conduction band at the Λ point, which is also often referred to as Q or Σ point. Due to its close energetic proximity to the conduction band

edge at the K point, the Λ point can play an important role for the transport and optical characteristics in TMDs [55–59].

The goal of this thesis is to develop a theoretical model describing the dynamics of excitons in TMDs including complex many-particle interactions. In order to obtain a material specific, realistic model which at the same time can still be numerically handled, we need to reduce the phase-space of electronic states. In particular, we restrict our consideration to the vicinity of valence band (v) maxima and conduction band (c) minima, since only in these regions bound exciton states can exist. In the close vicinity of a high-symmetry point $\zeta = \Gamma,\Lambda,K^{(\prime)}$ with an extremum in band $\lambda = c,v$ we approximate the band dispersion quadratically using isotropic masses, which yields

$$\varepsilon^{\lambda}_{\zeta\mathbf{k}} = \varepsilon^{\lambda}_{\zeta 0} + \sigma_{\lambda}\frac{\hbar^2}{2m^{\lambda}_{\zeta}}\mathbf{k}^2 \tag{3.1}$$

It is important to note that the momentum $\mathbf{k}$ here is measured from the respective high-symmetry point, so that the total crystal momentum is $\mathbf{k} + \zeta$. Moreover, all masses are defined positive so that $\sigma_{c/v} = \pm 1$, i.e. $m^v = m^h$ corresponds to the effective hole mass. The resulting effective mass model of the electronic structure is illustrated in Fig. 3.1c. Throughout this thesis we restrict the Hamiltonian to one fixed spin (e.g. denoted with ↑ in Fig. 3.1c), i.e. the spin of the upper valence band at K. This spin configuration comprises the energetically lowest spin-like, bright exciton at the K point (A exciton, K↑↑). The interaction of this exciton with other spin-configurations, such as the spin forbidden exciton (K↑↓) or the A exciton at K' (K'↓↓) require spin-flip or Coulomb exchange processes, which are not subject of this thesis. The material specific parameters m^{λ}_{ζ} and $\varepsilon^{\lambda}_{\zeta 0}$ in Eq. 3.1 can be extracted from density functional theory (DFT) and are given in Ref. [49].

3.2 Optical Matrix Element (Interband Current)

When considering interband transitions induced by the emission or absorption of light we focus on the so called A exciton resonances, which are direct optical transitions from the valence band maximum to the conduction band minimum at the K point. To obtain the electron-light matrix element Eq. 2.17 for this transition we use a tight-binding approximation of the electronic wavefunction. First-principle calculations [60, 61] of the electronic structure in TMDs show that the wave function in valence and conduction band at the K point are mostly composed of different d-type orbitals Φ^{λ} at metal-atom sites $\mathbf{R}$. Hence the Bloch

waves can be approximated as

$$\Psi^{\lambda}_{\mathbf{k}}(\mathbf{r}) = \langle \lambda \mathbf{k} | \mathbf{r} \rangle = \frac{1}{\sqrt{N}} \sum_{\mathbf{R}} e^{i(\mathbf{k}+\tau\mathbf{K})\mathbf{R}} \Phi^{\lambda}(\mathbf{r}-\mathbf{R}). \tag{3.2}$$

where $\tau = \pm 1$ for K and K$^{'}$ valley. Consequently the interband current matrix element reads

$$\begin{aligned} \mathbf{M}^{cv}_{\mathbf{k}}(\mathbf{q}) &= -i\hbar \langle c\mathbf{k}+\mathbf{q} | \nabla | v\mathbf{k} \rangle \\ &= \sum_{\mathbf{G}} \tilde{m}(\mathbf{k}+\tau\mathbf{K}+\mathbf{G}) \delta_{\mathbf{q},0} \end{aligned} \tag{3.3}$$

$$\tilde{m}(\mathbf{k}) = \hbar\mathbf{k} \frac{1}{A_{\mathrm{uc}}} \int dz \tilde{\Phi}^{c}(\mathbf{k},z) \tilde{\Phi}^{v}(\mathbf{k},z), \tag{3.4}$$

where $\mathbf{G}$ is a reciprocal lattice vector and $A_{uc} = A/N$ is the area of a unit cell. To arrive at Eq. 3.3 we performed an in-plane Fourier transformation $\Phi^{\lambda}(\mathbf{r}) = 1/A \sum_{\mathbf{k}} \tilde{\Phi}^{\lambda}(\mathbf{k},z) \exp(i\mathbf{k}\mathbf{r}_{\parallel})$, neglected umklapp processes with $\mathbf{q} = \mathbf{G}$ and used the completeness relation

$$\frac{1}{N} \sum_{\mathbf{R}} e^{i\mathbf{q}\mathbf{R}} = \sum_{\mathbf{G}} \delta_{\mathbf{q},\mathbf{G}}. \tag{3.5}$$

Next we use that $\Phi^{\lambda}(\mathbf{r})$ are smooth functions so that their Fourier components decay for large momenta [62]. Therefore we restrict the summation over $\mathbf{G}$'s to the leading terms with $\mathbf{K}+\mathbf{G} = C_3^n \mathbf{K}$, where C_3 is a rotation by 120°. Moreover we exploit the angular symmetry of d-orbitals found in Ref. [62],

$$\Phi^{\lambda}(C_3^n \mathbf{r}) = \exp(i\tau m_z^{\lambda} \frac{2\pi n}{3}) \Phi^{\lambda}(\mathbf{r}), \tag{3.6}$$

with the magnetic quantum numbers $m_z^c = 0$ and $m_z^v = 1$. Finally, in vicinity of K, i.e. $|\mathbf{k}| << |\mathbf{K}|$ we get,

$$\mathbf{M}^{cv} \approx \frac{\hbar\tau}{A_{uc}} \int dz \tilde{\Phi}^{c}(\tau\mathbf{K},z) \tilde{\Phi}^{v}(\tau\mathbf{K},z) \sum_{n} C_3^n \mathbf{K} e^{-i2\pi n\tau/3}. \tag{3.7}$$

The sum over n can be performed analytically

$$\sum_{n} C_3^n \mathbf{K} e^{-i2\pi n\tau/3} = -\frac{3}{2} |\mathbf{K}| e^{-i2\pi\tau/3} \begin{pmatrix} 1 \\ \tau i \end{pmatrix}. \tag{3.8}$$

Hence, we have analytically determined the optical selection rules. We group up all factors except for the Jones vector into the complex number M_0 determining the oscillator strength yielding

$$\mathbf{M}^{cv}_{\zeta} = \frac{1}{\sqrt{2}} M_0 \begin{pmatrix} 1 \\ \tau_{\zeta} i \end{pmatrix} (\delta_{\zeta,\mathrm{K}} + \delta_{\zeta,\mathrm{K}'}), \tag{3.9}$$

where we have explicitly added the restriction to the K and K' valley and defined $\tau_{\mathrm{K}^{(\prime)}} = \pm 1$. This result reflects the so called circular dichroism in TMDs [63]. Since the coupling strength to a light field with polarization e_σ is proportional to the product $\mathbf{M}^{cv} \cdot \mathbf{e}_\sigma$, transitions at the K-point can only be excited with $\sigma-$ circularly polarized light, while $\mathrm{K}^{(\prime)}$ transitions only couple to the opposite circular polarization.

The oscillator strength M_0 can be calculated from first principle methods. However, a good estimate can be obtained with a two band $\mathbf{k} \cdot \mathbf{p}$ expansion (cf. Sec. 3.3) of the band structure in vicinity of the K point, yielding [64]

$$M_0 = \sqrt{2}|\mathbf{M}^{cv} \cdot \mathbf{e}_x| = m_0 \sqrt{\frac{E_g}{2\mu}}, \tag{3.10}$$

with the electron rest mass m_0, the band gap $E_g = \varepsilon_0^c - \varepsilon_0^v$ and the reduced mass $\mu = m^c m^v/(m_c + m_v)$. Although the two band $\mathbf{k} \cdot \mathbf{p}$ model can be considered as rough estimation, the obtained oscillator strength compares well with ab initio results [63] and the radiative broadening of excitonic peaks calculated in this work agrees well with the experimentally extracted values (Paper 2).

3.3 Intraband Current Matrix Element

Apart from optical transitions between valence and conduction band, the coupling of the electrons to the electromagnetic field can also lead to an acelaration of charge carriers. Consequently if the electron hole plasma is driven by a low frequency field, such as terahertz or infrared radiation an oscillating current is generated. These processes are theoretically described by light field driven intraband transitions, i.e. the Hamiltonian Eq. 2.17 with $n = m$. In order to determine the corresponding intraband current matrix element $\mathbf{j}_\mathbf{k}^{\lambda\zeta}(\mathbf{q}) = e_0/m_0 \langle \lambda\zeta\mathbf{k} + \mathbf{q}|\hat{\mathbf{p}}|\lambda\zeta\mathbf{k}\rangle$ we express the wave function using lattice periodic Bloch functions $u_\mathbf{k}^{\lambda\zeta}$. For a fixed valley ζ we can write

$$\Psi_\mathbf{k}^\lambda(\mathbf{r}) = u_\mathbf{k}^\lambda(\mathbf{r}) e^{i\mathbf{kr}} \tag{3.11}$$

which for $\mathbf{q} << \mathbf{G}$ directly yields momentum conservation,

$$\mathbf{j}_\mathbf{k}^\lambda(\mathbf{q}) = \frac{e_0}{m_0} \langle u_\mathbf{k}^\lambda|\hbar\mathbf{k} + \hat{\mathbf{p}}|u_\mathbf{k}^\lambda\rangle \delta_{\mathbf{q},0}, \tag{3.12}$$

which results from dividing the whole integral into a sum of integrals over unit cells. To determine the remaining integral in Eq. 3.12 we again use the $\mathbf{k}\cdot\mathbf{p}$ theory, which is outlined in the following. Plugging ansatz 3.11 into the Schrödinger equation

yields

$$\tilde{H}_{\mathbf{k}} u^{\lambda}_{\mathbf{k}}(\mathbf{r}) = \varepsilon^{\lambda}_{\mathbf{k}} u^{\lambda}_{\mathbf{k}}(\mathbf{r}) \tag{3.13}$$

$$\tilde{H}_{\mathbf{k}} = H_0 + \frac{\hbar^2 \mathbf{k}^2}{2m_0} + \frac{\hbar}{m_0}\mathbf{k}\hat{\mathbf{p}}, \tag{3.14}$$

where the latter is referred to as $\mathbf{k} \cdot \mathbf{p}$ - Hamiltonian. Assuming that we know the solution of the above equation for a fixed $\mathbf{k}$, we can obtain the solution at small displacements $\tilde{H}_{\mathbf{k}+\mathbf{q}} \approx \tilde{H}_{\mathbf{k}} + \hbar\mathbf{q}/m_0(\hbar\mathbf{k} + \hat{\mathbf{p}})$ by treating the second term as a perturbation, which in first order yields

$$\varepsilon^{\lambda}_{\mathbf{k}+\mathbf{q}} = \varepsilon^{\lambda}_{\mathbf{k}} + \langle u^{\lambda}_{\mathbf{k}} | \hbar\mathbf{q}/m_0(\hbar\mathbf{k} + \hat{\mathbf{p}}) | u^{\lambda}_{\mathbf{k}} \rangle \tag{3.15}$$

$$\Rightarrow \mathbf{j}^{\lambda}_{\zeta\mathbf{k}} = \frac{e_0}{\hbar} \nabla_{\mathbf{k}} \varepsilon^{\lambda}_{\zeta\mathbf{k}}, \tag{3.16}$$

Here we set $\mathbf{q} \to 0$ and added the previously suppressed valley index in the second line. Hence the current matrix element is simply given by the product of the electron charge with the local group velocity.

3.4 Coulomb Matrix Element

The Coulomb interaction matrix element in Eq. 2.15 can be split into two major components via Fourier transformation of the interaction potential,

$$V_{ijkl} = \sum_{\mathbf{q}} V_{\mathbf{q}} F_{il}(\mathbf{q}) F_{jk}(-\mathbf{q}); \qquad F_{fi}(\mathbf{q}) = \langle f | e^{i\mathbf{q}\mathbf{r}} | i \rangle. \tag{3.17}$$

Here the form factor $F_{fi}(\mathbf{q})$ determines the scattering cross-section for a transition $i \to f$ under momentum transfer $\mathbf{q}$. Throughout this work we only consider band conserving Coulomb processes, and therefore only need to consider form factors with $\lambda_i = \lambda_f$. Moreover, for the Coulomb potential $V_{\mathbf{q}}$ we will in the following consider the impact of the non-trivial dielectric environment of a quasi-two-dimensional layer embedded in a three-dimensional world.

Scattering Form Factors

As we will show further below, the Coulomb potential decays quickly for large momenta $\mathbf{q}$. Therefore, we restrict to the case of $\mathbf{q} << \mathbf{G}$ and also neglect Coulomb-induced intervalley scattering with $\zeta_i \neq \zeta_j$. The remaining form factor can be

evaluated using the Bloch representation Eq. 3.11,

$$F^{\lambda}_{\mathbf{k}_f,\mathbf{k}_i}(\mathbf{q}) = \langle \lambda \mathbf{k}_f | e^{i\mathbf{qr}} | \lambda \mathbf{k}_i \rangle \tag{3.18}$$

$$= \sum_{\mathbf{R}} e^{i(\mathbf{q}+\mathbf{k}_i-\mathbf{k}_f)\mathbf{R}} \int_{uc} dr u^{\lambda}_{\mathbf{k}_f}{}^{*}(\mathbf{r}) e^{i(\mathbf{q}+\mathbf{k}_i-\mathbf{k}_f)\mathbf{r}} u^{\lambda}_{\mathbf{k}_i}(\mathbf{r}) \tag{3.19}$$

$$= \delta_{\mathbf{q},\mathbf{k}_f-\mathbf{k}_i} \langle u^{\lambda}_{\mathbf{k}_i+\mathbf{q}} | u^{\lambda}_{\mathbf{k}_i} \rangle \approx \delta_{\mathbf{q},\mathbf{k}_f-\mathbf{k}_i}, \tag{3.20}$$

where in the last step we used that the Bloch functions are almost constant in vicinity of high symmetry points.

Dielectric Screening in Two-Dimensional Materials

One of the most important difference between monolayers and conventional quasi-2D systems such as quantum wells, is the maximal confinement of electrons to a plane and the resulting strong modification of the dielectric screening [65, 66]. Figure 3.2 illustrates the difference between the field lines in a 3D system and 2D system embedded into a 3D environment [67]. In a bulk system (Fig. 3.2a) the

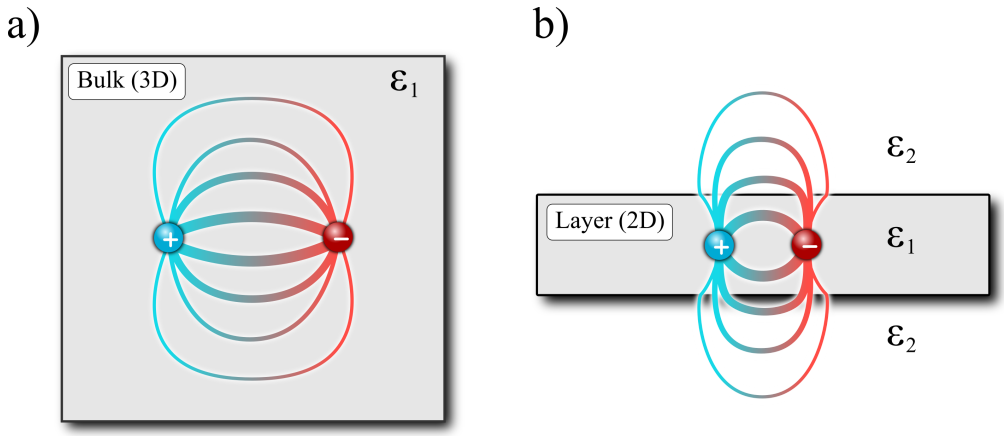

Figure 3.2: Dielectric Screening in a) bulk and b) monolayer [67]. While in bulk systems the field lines between interacting charges penetrate the surrounding crystal, in the case of monolayers most field lines expand in vacuum or materials with lower dielectric constants, giving rise to a weaker screening in two-dimensional systems.

field lines between two attracting charges penetrate the surrounding material and become weakened by the induced polarization. In contrast, for the 2D system, most field lines penetrate the space surrounding the monolayer and therefore -in the case of low dielectric constant- become much less weakened than in the bulk material. Moreover, the resulting distance behaviour of the effective Coulomb potential becomes a mixture of 2D and 3D components. To determine the potential

$V(\mathbf{r})$ we apply a fully classical approach, assuming point charges localized in the centre ($z = 0$) of a homogeneous dielectric slab with thickness d [68, 69]. In this picture the potential can be determined by the first Maxwell equation:

$$\nabla \mathbf{D} = -e_0 \delta(\mathbf{r}) \quad \text{with} \quad \mathbf{D} = -\epsilon_0 / e_0 \sum_{i=1,2,3} \epsilon^i(\mathbf{r}) \partial_i V(\mathbf{r}) \tag{3.21}$$

$$\epsilon^i(\mathbf{r}) = \begin{cases} \epsilon^i_{\text{TMD}} & \text{for } |z| \leq d/2 \\ \epsilon^i_{\text{bg}} & \text{for } |z| > d/2 \end{cases} \tag{3.22}$$

where the second line defines the dielectric landscape through the dielectric tensor of the TMD (ϵ_1) and the environment(ϵ_2). Using Gauss's divergence theorem, we can determine conditions for the field at the boundary of the slab, yielding the 2D Fourier transformed potential (at $z = 0$)

$$V_{\mathbf{q}} = \frac{e_0^2}{2\epsilon_0 A q \epsilon_{\text{s}}(q)} \tag{3.23}$$

$$\text{with} \quad \epsilon_{\text{s}}(q) = \kappa_{\text{TMD}} \tanh\left(\frac{1}{2}\left[\alpha_{\text{TMD}} d q - \ln\left(\frac{\kappa_{\text{TMD}} - \kappa_{\text{bg}}}{\kappa_{\text{TMD}} + \kappa_{\text{bg}}}\right)\right]\right) \tag{3.24}$$

whith $\kappa = \sqrt{\epsilon^{\parallel} \epsilon^{\perp}}$ and $\alpha = \sqrt{\epsilon^{\parallel} / \epsilon^{\perp}}$.

In the limiting case of small momenta $\alpha_{\text{TMD}} dq << 1$ and large dielectric contrast $\kappa_{\text{TMD}} >> \kappa_{\text{bg}}$ the potential can be approximated with the Keldysh form [68, 69]

$$V_{\mathbf{q}} = \frac{e_0^2}{2\epsilon_0 A q (\kappa_{\text{bg}} + \epsilon^{\parallel}_{\text{TMD}} dq/2)} \tag{3.25}$$

Hence, for small wave vectors (large distances) we obtain an effective 2D distance dependence ($1/q$) only screened by the environment, while at larger wave vectors (small distances) the potential becomes more 3D ($1/q^2$) with increasing influence of the TMD screening. Throughout this thesis we use dielectric constants for TMD monolayers obtained from DFT calculations [70].

3.5 Phonon Dispersion and Electron-Phonon Coupling

In addition to the electronic degrees of freedom, the properties and dynamics of excitons are also strongly influenced by the interaction with phonons. Similar to the electronic band structure, the phonon dispersion is characteristic for the

material and can be obtained through first principles calculations. The generic form of the phonon dispersion in TMD monolayers is shown along the symmetry paths in Fig. 3.3.

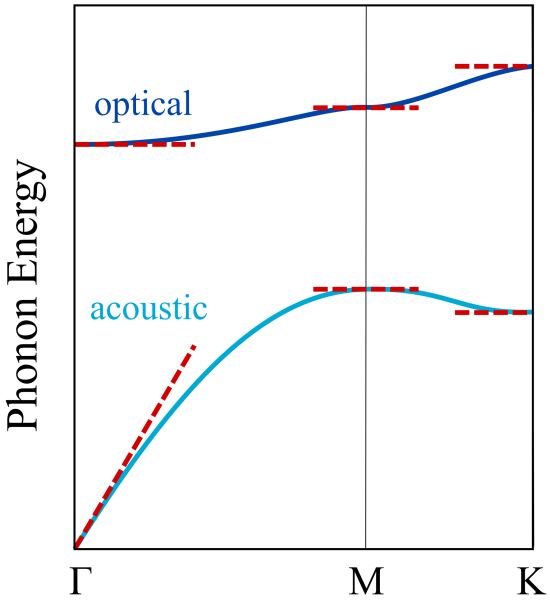

Figure 3.3: Sketch of typical phonon dispersion of acoustic and optical modes in TMDs [71], along with the linear (Debye) and constant (Einstein) approximation (red dashed).

We again simplify the treatment of phonons by using a zeroth/first order Taylor expansion in vicinity of high symmetry points to incorporate material specific phonon energies into our model,

$$\Omega^{\alpha}_{\zeta\mathbf{q}} = \begin{cases} v_\alpha \mathbf{q} & \text{for } \zeta = \Gamma \quad \& \quad \alpha = \text{LA,TA} \\ \\ \Omega^{\alpha}_{\zeta} & \text{else} \end{cases} . \tag{3.26}$$

Hence, long range acoustic phonons (at the Γ point) are approximated with a linear dispersion, characterized by the sound velocities v_α (Debye approximation), while optical modes as well as short wave length acoustic phonons ($\zeta \neq \Gamma$) are included with constant energies Ω^{α}_{ζ} (Einstein approximation). Note that the momentum $\mathbf{q}$ in Eq. 3.26 is measured with respect to the high symmetry point ζ, so that the total crystal momentum is given by $\zeta + \mathbf{q}$. Throughout this work we include longitudinal and transverse acoustic modes (LA,TA), as well as the corresponding optical modes (LO, TO) and the out-of-plane homopolar optical mode (A1). The coupling to other out-of-plane modes requires a symmetry breaking process, which is not the focus of this work. All phonon energies and sound velocities in TMDs are given in [71].

The interaction matrix element between electrons and phonons in Eq. 2.21 depends on the wave function overlap of initial and final electronic state as well as

the potential created through the phonon mode specific oscillation of the crystal. Therefore the matrix element is very sensitive to the involved electronic band, phonon mode and valley quantum numbers. While a simple parametrization of the interaction strength with experimentally accessible quantities might be possible for a single scattering channel, e.g intravalley acoustic phonon scattering, the use of parameters from ab initio calculations in literature [71, 72] is inevitable for the modeling of electron phonon scattering across the whole Brillouin zone. The so far most complete set of parameters from a first principles study of electron-phonon coupling strength in TMDs is given in Ref. [71]. In particular Ref. [71] gives a set of parameters, for the scattering from state (λ, ζ_i) to (λ, ζ_f) via interaction with a phonon of mode α and momentum $\zeta_f - \zeta_i + \mathbf{q}$. To this end the deformation potential approximation is applied, corresponding to a zeroth/first order Taylor expansion of the full electron-phonon coupling element obtained from DFPT calculations, reading

$$D^{\alpha\lambda}_{\zeta_f\zeta_i\mathbf{q}} \approx \sqrt{\frac{\hbar}{2\rho A\Omega_{\alpha\mathbf{q}}}}\tilde{D}^{\alpha\lambda}_{\zeta_f\zeta_i\mathbf{q}} \tag{3.27}$$

$$\tilde{D}^{\alpha\lambda}_{\zeta_f\zeta_i\mathbf{q}} = \begin{cases} \tilde{D}^{\lambda(1)}_{\zeta}\mathbf{q} & \text{for } \zeta_i = \zeta_f = \zeta \quad \& \quad \alpha = \text{LA,TA} \\ \\ \tilde{D}^{\alpha\lambda(0)}_{\zeta_f,\zeta_i} & \text{else} \end{cases}, \tag{3.28}$$

where ρ denotes the surface mass density of the TMD layer. It is important to note that the phonon momentum is again referring to the high symmetry point $\zeta_f - \zeta_i$ and momentum conservation is presumed,

$$H = \sum_{\alpha\lambda\mathbf{kq}} D^{\alpha\lambda}_{\mathbf{k},\mathbf{q}} a^\dagger_{\lambda\mathbf{k}+\mathbf{q}} a_{\lambda\mathbf{k}}(b_{\alpha\mathbf{q}} + b^\dagger_{\alpha-\mathbf{q}}) \tag{3.29}$$

$$\approx \sum_{\alpha\lambda\zeta\mathbf{k}\zeta'\mathbf{k}'} D^{\alpha\lambda}_{\zeta'\zeta,\mathbf{k}'-\mathbf{k}} a^\dagger_{\lambda\zeta',\mathbf{k}'} a_{\lambda\zeta,\mathbf{k}}(b_{\alpha,\zeta'-\zeta,\mathbf{k}'-\mathbf{k}} + b^\dagger_{\alpha,\zeta-\zeta',\mathbf{k}-\mathbf{k}'}), \tag{3.30}$$

where the first line corresponds to global coordinates, while the second line uses the expansions of operators in vicinity of high symmetry points and valley local coordinates.

Finally, it is important to note that the parameters in Ref. [71] do not include any phase or sign of the matrix elements. Usually, the electron-phonon coupling only enters the equations of motion of electronic observables in terms of an absolute square value, so that the sign of the matrix element is irrelevant. However, as we will show in Sec. 4.5, the exciton-phonon matrix element is given by the difference of the electronic coupling strengths in valence and conduction band, which is very sensitive to their signs. To solve this issue, we assume that the coupling strength for acoustic modes from Ref. [71] predominantly results from the deformation potential mechanism [73]. Moreover, the deformation potential in TMDs has been shown to have opposite signs in valence and conduction band [74], i.e. the bands

shift in opposite directions under strain. In contrast, optical modes mostly couple to electrons via the Fröhlich interaction which has the same sign in both bands. We therefore set $\mathrm{sgn}(D^v) = -1$ for the two acoustic modes, while all other modes have positive matrix elements.

3.6 Summary – Full Hamilton Operator

With the above introduced approximations for electron/phonon energies and the discussed interaction matrix elements we can now model the many-particle dynamics of valence and conduction band electrons ($\lambda = c,v$) in the vicinity of high symmetry points of the hexagonal Brillouin zone $\zeta = \Gamma,\Lambda^{(\prime)},K^{(\prime)}$. The quantum dynamics of this system is fully determined by the Hamiltonian,

$$\begin{aligned}
H &= H_0 + H_{\text{Coul}} + H_{\text{el-l}} + H_{\text{el-pt}} + H_{\text{el-ph}} \\
&= \sum_{\lambda\zeta\mathbf{k}} \varepsilon^{\lambda}_{\zeta\mathbf{k}} a^{\dagger}_{\lambda\zeta,\mathbf{k}} a_{\lambda\zeta,\mathbf{k}} + \sum_{\sigma\mathbf{k}} \hbar\omega_{\mathbf{k}} c^{\dagger}_{\sigma\mathbf{k}} c_{\sigma\mathbf{k}} + \sum_{\alpha\mathbf{q}} \hbar\Omega_{\alpha\mathbf{q}} b^{\dagger}_{\alpha\mathbf{q}} b_{\alpha\mathbf{q}} \\
&+ \frac{1}{2} \sum_{\lambda\zeta\mathbf{k}\lambda'\zeta'\mathbf{k}'\mathbf{q}} V_{\mathbf{q}} a^{\dagger}_{\lambda\zeta,\mathbf{k}+\mathbf{q}} a^{\dagger}_{\lambda'\zeta',\mathbf{k}'-\mathbf{q}} a_{\lambda'\zeta',\mathbf{k}'} a_{\lambda\zeta,\mathbf{k}} \\
&+ \sum_{\lambda\zeta\mathbf{k}} \mathbf{A}\cdot\mathbf{j}^{\lambda}_{\zeta\mathbf{k}} a^{\dagger}_{\lambda\zeta,\mathbf{k}} a_{\lambda\zeta,\mathbf{k}} + \frac{e_0}{m_0} \sum_{\zeta\mathbf{k}} \mathbf{A}\cdot\mathbf{M}^{vc}_{\zeta} a^{\dagger}_{v\zeta,\mathbf{k}} a_{c\zeta,\mathbf{k}} + \text{h.c.} \\
&+ \sum_{\sigma\mathbf{q}\zeta\mathbf{k}} \tilde{M}^{\zeta}_{\sigma\mathbf{q}} a^{\dagger}_{v\zeta,\mathbf{k}+\mathbf{q}_{\parallel}} a_{c\zeta,\mathbf{k}} c^{\dagger}_{\mathbf{q}} + \text{h.c.} \\
&+ \sum_{\alpha\lambda\zeta\mathbf{k}\zeta'\mathbf{k}'} D^{\alpha\lambda}_{\zeta'\zeta,\mathbf{k}'-\mathbf{k}} a^{\dagger}_{\lambda\zeta',\mathbf{k}'} a_{\lambda\zeta,\mathbf{k}} (b_{\alpha,\zeta'-\zeta,\mathbf{k}'-\mathbf{k}} + b^{\dagger}_{\alpha,\zeta-\zeta',\mathbf{k}-\mathbf{k}'}).
\end{aligned} \tag{3.31}$$

For completeness we have summarized all three forms of the electron light interaction considered in this work. Here $H_{\text{el-l}}$ is used to describe the interaction of electrons with an external laser pulse. In particular, the term $\propto \mathbf{j}$ will only give a significant contribution for low frequency fields (e.g. THz), while the second term $\propto \mathbf{M}$ is only relevant when the laser pulse is resonant to the interband transition. The fully quantized form $H_{\text{el-pt}}$ is important in the incoherent limit and is needed to describe spontaneous emission. Depending on the studied conditions, we will restrict to one of these three forms.

Finally, the Coulomb Hamiltonian H_{Coul} contains electron-electron, hole-hole as well as electron-hole interaction. We principally include all three contributions

in the next section and discuss all relevant Coulomb effects in the coherent limit. However, throughout this work we restrict the model to the low excitation limit. Here, the intraband Coulomb interaction is negligible and we only have to deal with the interaction between electrons and holes ($\lambda \neq \lambda'$).

CHAPTER 4

LINEAR SPECTROSCOPY

One of the most common techniques to characterize the properties of a material is the absorption or transmission spectroscopy. Here a sample is illuminated with coherent light (usually a laser) and the transmitted or reflected fraction of the light is measured as function of the wavelength. In this way one obtains access to the internal resonance energies of the material. In order to interpret such a transmission spectrum on a microscopic level, a model of the materials degrees of freedom is needed. In this chapter we investigate the interaction of TMDs with coherent light and calculate their optical response to a weak laser field. In particular, we derive how the formation of excitons modifies the optical resonances of TMDs and the broadening of excitonic absorption lines due to scattering with phonons.

4.1 Optical Susceptibility

The starting point of a theoretical investigation of the matter-light interaction are the macroscopic Maxwell equations. Assuming that the investigated material is neutral but can be electrically polarized ($\mathbf{P}$), the electrical field $\mathbf{E}$ of the coherent laser light is given by the inhomogeneous wave equation [37],

$$(\nabla^2 - \frac{n^2}{c^2}\partial_t^2)\mathbf{E}(\mathbf{r},t) = \mu_0 \partial_t^2 \mathbf{P}(\mathbf{r},t), \tag{4.1}$$

where n is the refractive index of the background medium and c is the vacuum light velocity. The key step to a linear response theory, is to assume that for harmonically oscillating, weak light fields, the polarization in the material is directly

proportional to the driving field. Hence, in the frequency domain we set for the components,

$$P_i(\omega) = \epsilon_0 \sum_j \chi_{ij}^{(1)}(\omega) E_j(\omega) \tag{4.2}$$

$$\chi_i(\omega) = \frac{P_i(\omega)}{\epsilon_0 E_i(\omega)} = \frac{j_i(\omega)}{\epsilon_0 \omega^2 A_i(\omega)} \qquad (\text{for} \quad \chi_{ij}^{(1)} = \chi_i \delta_{ij}), \tag{4.3}$$

which defines the complex valued optical susceptibility tensor $\chi^{(1)}$. In the second step we have expressed the electrical field in terms of the vector potential $\mathbf{E} = -\dot{\mathbf{A}}$ and rewrote the oscillating polarization as a macroscopic current $\mathbf{j} = \dot{\mathbf{P}}$. It is straightforward to show that the imaginary part of the susceptibility leads to a damping of a propagating wave, which corresponds to the absorption of energy by the material. To calculate the response χ based on a microscopic model, the current j is interpreted as the probability current [47]

$$\hat{\mathbf{j}}(t) = \frac{e_0}{2m_0 A} \int d^3r \big(\hat{\Psi}^\dagger(\mathbf{r}) \mathbf{p} \hat{\Psi}(\mathbf{r}) - (\mathbf{p}\hat{\Psi}^\dagger(\mathbf{r})) \hat{\Psi}(\mathbf{r}) \big) \tag{4.4}$$

$$\Rightarrow \langle \hat{\mathbf{j}} \rangle(t) \,\big|_{\text{inter}} = \frac{2e_0}{m_0 A} \sum_{\mathbf{k}} \text{Re}\{\mathbf{M}^{vc*} p_{\mathbf{k}}^{cv}(t)\} \tag{4.5}$$

Here we only took into account the contribution stemming from interband transitions, since absorption experiments are usually performed in frequency ranges, which are too large to induce oscillations of charge carrier occupations. Moreover, we have introduced the microscopic polarization $p_{\mathbf{k}}^{cv} = \langle a_{c\mathbf{k}}^\dagger a_{v\mathbf{k}} \rangle$ which is the probability amplitude for an interband transition.

In the following sections, we discuss the equations of motion for the microscopic polarization, including the electron-hole Coulomb interaction as well as electron-phonon scattering.

4.2 Semiconductor Bloch Equations

In the following we determine the evolution of a general interband polarization $p_{\mathbf{k}\mathbf{k}'}^{\lambda\lambda'} = \langle a_{\lambda\mathbf{k}}^\dagger a_{\lambda'\mathbf{k}'} \rangle$ by applying the Heisenberg equation of motion Eq. 2.25. For now we include the electronic eigenenergies H_0, the semi-classical electron light interaction $H_{\text{el-l}}$ and the Coulomb interaction H_{Coul}. The inclusion of the Coulomb interaction, gives rise to a hierarchy problem discussed in Sec. 2.3. We truncate our equations on a single particle level (mean field description) by applying the Hartree-Fock factorization (Eq. 2.31 to all appearing two-particle expectation values. Thereby, we find the well studied semiconductor Bloch equations [39, 44] for the microscopic polarization $p_{\mathbf{k}\mathbf{k}'}^{\lambda\lambda'}$ and band occupations $f_{\mathbf{k}}^{\lambda} = \langle a_{\lambda\mathbf{k}}^\dagger a_{\lambda\mathbf{k}} \rangle$,

$$i\hbar\partial_t p^{\lambda\lambda'}_{\mathbf{k}\mathbf{k}'} = (\tilde{\varepsilon}^{\lambda'}_{\mathbf{k}'} - \tilde{\varepsilon}^{\lambda}_{\mathbf{k}})p^{\lambda\lambda'}_{\mathbf{k}\mathbf{k}'} + (f^{\lambda}_{\mathbf{k}} - f^{\lambda'}_{\mathbf{k}'})\tilde{\Omega}^{\lambda\lambda'}_{\mathbf{k}\mathbf{k}'}(t) \tag{4.6}$$

$$\hbar\partial_t f^{\lambda}_{\mathbf{k}} = -2\sum_{\lambda'\mathbf{k}'} \mathrm{Im}\{(\tilde{\Omega}^{\lambda\lambda'}_{\mathbf{k}\mathbf{k}'})^* p^{\lambda\lambda'}_{\mathbf{k}\mathbf{k}'}\}, \tag{4.7}$$

with the Coulomb renormalized band energies [75–77],

$$\tilde{\varepsilon}^{\lambda}_{\mathbf{k}} = \varepsilon^{\lambda}_{\mathbf{k}} - \sum_{\mathbf{q}} V_{\mathbf{q}} f^{\lambda}_{\mathbf{k}+\mathbf{q}} \tag{4.8}$$

and the generalized Rabi energy,

$$\tilde{\Omega}^{\lambda\lambda'}_{\mathbf{k}\mathbf{k}'}(t) = \frac{e_0}{m_0}\mathbf{M}^{\lambda'\lambda}_{\mathbf{k}} \cdot \mathbf{A}(t)\delta_{\mathbf{k}\mathbf{k}'} + \sum_{\mathbf{q}} V_{\mathbf{q}} p^{\lambda\lambda'}_{\mathbf{k}+\mathbf{q},\mathbf{k}'+\mathbf{q}}. \tag{4.9}$$

Throughout this work, we consider low excitation powers, meaning that we neglect the changes in band occupations f induced by the laser pulse. Moreover, we assume that the Fermi-level lies deep within the band gap, where the latter is large compared to the considered thermal energies. In this case we can neglect the so called phase space filling, i.e. $(1 - f^{\mathrm{e}}_{\mathbf{k}} - f^{\mathrm{h}}_{\mathbf{k}}) \approx 1$, as well as occupation induced energy renormalizations. For the low density regime the Bloch equations can be simplified to ($p^{cv} \equiv p$):

$$i\hbar\partial_t p_{\mathbf{k}\mathbf{k}'} = -\sum_{\mathbf{q}} \mathcal{W}_{\mathbf{k}\mathbf{k}'\mathbf{q}} p_{\mathbf{k}+\mathbf{q},\mathbf{k}'+\mathbf{q}} - \frac{e_0}{m_0}\mathbf{M}^{vc}_{\mathbf{k}} \cdot \mathbf{A}(t)\delta_{\mathbf{k}\mathbf{k}'} \tag{4.10}$$

$$\mathcal{W}_{\mathbf{k}\mathbf{k}'\mathbf{q}} = (\varepsilon^{c}_{\mathbf{k}} - \varepsilon^{v}_{\mathbf{k}'})\delta_{\mathbf{q},0} - V_{\mathbf{q}}, \tag{4.11}$$

The from of Eq. 4.10 illustrates how the presence of the electron-hole interaction modifies the optical properties of the system. While in the case $V \longrightarrow 0$ the eigenfrequency of $p_{\mathbf{k}\mathbf{k}'}$ is given by the free particle transition energy $\varepsilon^{c}_{\mathbf{k}} - \varepsilon^{v}_{\mathbf{k}'}$, the presence of Coulomb interaction gives rise to a mixing of electronic states with different momenta $\mathbf{k}$, rendering it as a "bad" quantum number.

4.3 Wannier Equation

In order to obtain analytic insights into the new resonance energies of the system, we first consider the homogeneous version of Eq. 4.10,

$$i\hbar\partial_t p_{\mathbf{k},\mathbf{k}'} = -\sum_{\mathbf{q}} \mathcal{W}_{\mathbf{k}\mathbf{k}'\mathbf{q}} p_{\mathbf{k}+\mathbf{q},\mathbf{k}'+\mathbf{q}}. \tag{4.12}$$

In order to find the solutions of this equation, we calculate the eigenvalues and -functions of the Wannier matrix $\mathcal{W}$. After that we expand p in terms of the eigenfunctions Φ.

The corresponding eigenvalue problem reads

$$(\varepsilon^c_{\mathbf{k}_e} - \varepsilon^v_{\mathbf{k}_h})\Phi(\mathbf{k}_e, \mathbf{k}_h) - \sum_{\mathbf{l}} V_{\mathbf{q}}\Phi(\mathbf{k}_e + \mathbf{q}, \mathbf{k}_h + \mathbf{q}) = E_{\mathbf{k}_e,\mathbf{k}_h}\Phi(\mathbf{k}_e,\mathbf{k}_h), \tag{4.13}$$

which resembles the two-particle Schrödinger equation for an electron and a hole, and is referred to as Wannier equation [37, 39, 78, 79]. Here, Φ and E denote the wave function and eigenenergy of the electron-hole pair respectively. In principle Eq. 4.13 can be solved numerically when the band structure and Coulomb matrix element is known throughout the whole Brillouin zone. However, in case of so called Wannier excitons, where the binding radii are large compared to the unit cell, the excitonic wave function in momentum space becomes strongly localized in the vicinity of energetic minima of the band structure. In this case the problem can be simplified significantly by expanding the band structure in vicinity of its extrema. Assuming a parabolic dispersion (Eq. 3.1) the eigenvalue problem can be separated into relative ($\mathbf{k}$) and centre-of-mass (CoM) momentum ($\mathbf{Q}$) which are defined through the effective electron and hole masses m_e and m_h via

$$\mathbf{k} = \alpha\mathbf{k}_h + \beta\mathbf{k}_e \quad \text{and} \quad \mathbf{Q} = \mathbf{k}_e - \mathbf{k}_h \tag{4.14}$$

$$\mathbf{k}_e = \mathbf{k} + \alpha\mathbf{Q} \quad \text{and} \quad \mathbf{k}_h = \mathbf{k} - \beta\mathbf{Q}, \tag{4.15}$$

where $\alpha = m_e/M$, $\beta = m_h/M$ and $M = m_e + m_h$. Hence the kinetic energy of the electron hole pair can be decomposed

$$\varepsilon^c_{\mathbf{k}_e} - \varepsilon^v_{\mathbf{k}_h} = \frac{(\hbar\mathbf{k}_e)^2}{2m_e} + \frac{(\hbar\mathbf{k}_h)^2}{2m_h} + E_g = \frac{(\hbar\mathbf{k})^2}{2m_r} + \frac{(\hbar\mathbf{Q})^2}{2M} + E_g \tag{4.16}$$

with the reduced mass $m_r^{-1} = m_e^{-1} + m_h^{-1}$. Since the second term on the left side of Eq. 4.13 is independent of $\mathbf{Q}$, we can separate relative and the center-of-mass motion $\Phi(\mathbf{k},\mathbf{Q}) = \Psi(\mathbf{k})\eta(\mathbf{Q})$ and find

$$\frac{(\hbar\mathbf{k})^2}{2m_r}\Psi^\mu(\mathbf{k}) - \sum_{\mathbf{q}} V_{\mathbf{q}}\Psi^\mu(\mathbf{k} + \mathbf{q}) = E^{\mathrm{b}}_\mu\Psi^\mu(\mathbf{k}), \tag{4.17}$$

with the binding energy E^{b}_μ of the excitonic state μ, which is independent of the centre of mass motion. Hence, the equation of motion for the microscopic polarization can be diagonalized in momentum by performing a basis change $p_{\mathbf{k}_e,\mathbf{k}_h} \longrightarrow P^\mu_{\mathbf{Q}}$

via

$$p_{\mathbf{k}_e,\mathbf{k}_h}(t) = \sum_\mu P^\mu_{\mathbf{Q}}(t)\Psi^\mu(\mathbf{k}) \tag{4.18}$$

$$= \sum_\mu P^\mu_{\mathbf{k}_e-\mathbf{k}_h}(t)\Psi^\mu(\alpha\mathbf{k}_h + \beta\mathbf{k}_e) \tag{4.19}$$

which in Eq. 4.6 gives rise to Bloch equations in the excitonic basis

$$i\hbar\partial_t P^\mu_{\mathbf{Q}} = -E^\mu_{\mathbf{Q}}P^\mu_{\mathbf{Q}} - \Omega^\mu\delta_{\mathbf{Q},0} \tag{4.20}$$

$$E^\mu_{\mathbf{Q}} = \frac{\hbar^2\mathbf{Q}^2}{2M} + E_g + E^{\mathrm{b}}_\mu \tag{4.21}$$

$$\Omega^\mu = \frac{e_0}{m_0}\sum_{\mathbf{k}} \Psi^\mu(\mathbf{k})^*\mathbf{M}^{vc}_{\mathbf{k}}\cdot\mathbf{A}(t) = \frac{e_0}{m_0}\boldsymbol{\mathcal{M}}^\mu\cdot\mathbf{A}(t). \tag{4.22}$$

Here we used the orthogonality of the wave functions ($\sum_{\mathbf{k}}\Psi^\mu(\mathbf{k})^*\Psi^\nu(\mathbf{k}) = \delta_{\mu\nu}$). The solution of Eq. 4.20 is now easily obtained in the frequency domain

$$P^\mu_{\mathbf{Q}}(\omega) = \frac{\Omega^\mu(\omega)\delta_{\mathbf{Q},0}}{\hbar\omega - E^\mu_{\mathbf{Q}} - i\Gamma}. \tag{4.23}$$

Finally, we can determine the optical susceptibility of the excitonic system by transforming Eq. 4.5 into exciton basis and using the definition of the susceptibility Eq. 4.3. For σ-polarized light we find the so-called Elliot formula [78],

$$\chi_\sigma(\omega) = \frac{e_0^2}{m_0^2\epsilon_0 A\omega^2}\sum_\mu \frac{|\mathcal{M}^\mu_\sigma|^2}{\hbar\omega - E^\mu_0 - i\Gamma}. \tag{4.24}$$

The above equation illustrates two important aspects of the matter-light interaction within an excitonic system. First of all we find that only excitons with vanishing CoM momentum $\mathbf{Q} = 0$ can be directly excited with light. This reflects the momentum conservation, since the momentum carried by a photon at optical frequencies can be neglected in most considerations. Secondly, we find that the electron-hole Coulomb interaction has significantly modified the spectrum of resonance energies. Without Coulomb interaction optical transitions are allowed as long as the energy of the light is larger than the band gap. Eq. 4.24 shows that the Coulomb-induced mixing of polarizations at different momenta leads to a renormalization of the optical spectrum, now only allowing transitions at a series of exciton eigenenergies E^μ_0.

Moreover, we have artificially added a damping constant Γ in Eq. 4.23, which determines the energetic width of excitonic resonances. In Sec. 4.5 and 4.6 we show how this dephasing constants can be determined considering exciton-phonon interaction as well as radiative damping.

In the following, we demonstrate how the Wannier equation is solved numerically and discuss the obtained excitonic eigenspectrum.

4.4 Excitonic Bandstructure and Wavefunctions

The Wannier equation can be solved numerically via discretization and subsequent matrix diagonalization. First of all we take the limit of infinitely large systems, in which the electron momenta become continuous and we set,

$$\sum_{\mathbf{k}} \longrightarrow \frac{A}{4\pi^2}\int d^2k = \frac{A}{4\pi^2}\int_0^{2\pi} d\phi \int_0^{\infty} k dk, \tag{4.25}$$

Where in the second step we used polar coordinates. Moreover, we can reduce the dimensions of the algebraic problem by exploiting the symmetry of the Coulomb potential. Within the effective mass approximation introduced in Sec. 3.1 the Coulomb potential between electron and hole is rotationally symmetric, so that it holds,

$$\Psi(\mathbf{k}) = \psi(k)e^{iL\phi}, \tag{4.26}$$

which defines the angular momentum quantum number L. With Eq. 4.25 and 4.26 we can rewrite the Wannier equation (Eq. 4.17) into

$$\frac{\hbar^2 k^2}{2m_r}\psi(k) - \int_0^{\infty} dk' k' V^L_{kk'}\psi(k') = E^{\mathrm{b}}_L \psi(k) \tag{4.27}$$

$$V^L_{kk'} = \frac{A}{4\pi^2}\int_0^{2\pi} d\theta V(q = \sqrt{k^2 + k'^2 - 2kk'\cos(\theta)})e^{iL\theta} \tag{4.28}$$

The angle averaged Coulomb potential $V^L_{kk'}$ is now calculated numerically via Riemann sums, i.e. $\int_0^{2\pi} d\theta f(\theta) \approx \sum_i \Delta\theta f(\theta_i)$ with $\theta_i = \Delta\theta,...,n\Delta\theta,...,2\pi$. Similarly, we transform the above integral equation into a linear algebra problem by replacing the indefinite integral with a finite Riemann sum, $\int_0^{\infty} dk f(k) \approx \sum_i \Delta k f(k_i)$ with $k_i = \Delta k,...,n\Delta k, k_{\max}$. Hence, we finally get

$$\sum_j W^L_{ij}\psi^{nL}_j = E^{\mathrm{b}}_{nL}\psi^{nL}_i \tag{4.29}$$

$$W^L_{ij} = \frac{\hbar^2 k_i^2}{2m_r}\delta_{ij} - \Delta k k_j V^L_{k_i k_j} \quad \text{and} \quad \psi_i = \psi(k_i). \tag{4.30}$$

Here the main quantum number n is indexing the solutions of the above eigenvalue problem for a given L. For the numerical calculation of eigenvalues and eigenvectors one can now use the standard functions, e.g. implemented in one of the C libraries. However, it is important to note that the eigenvectors usually need to be normalized afterwards to account for the fact that our vectors only correspond to the radial component of the otherwise 2D function. Figure 4.1a shows the binding energy E^b for the s- ($L = 0$) and p-type ($L = 1$) ground state in a WSe_2 monolayer as function of the averaged dielectric environment. In addition to the excitons at

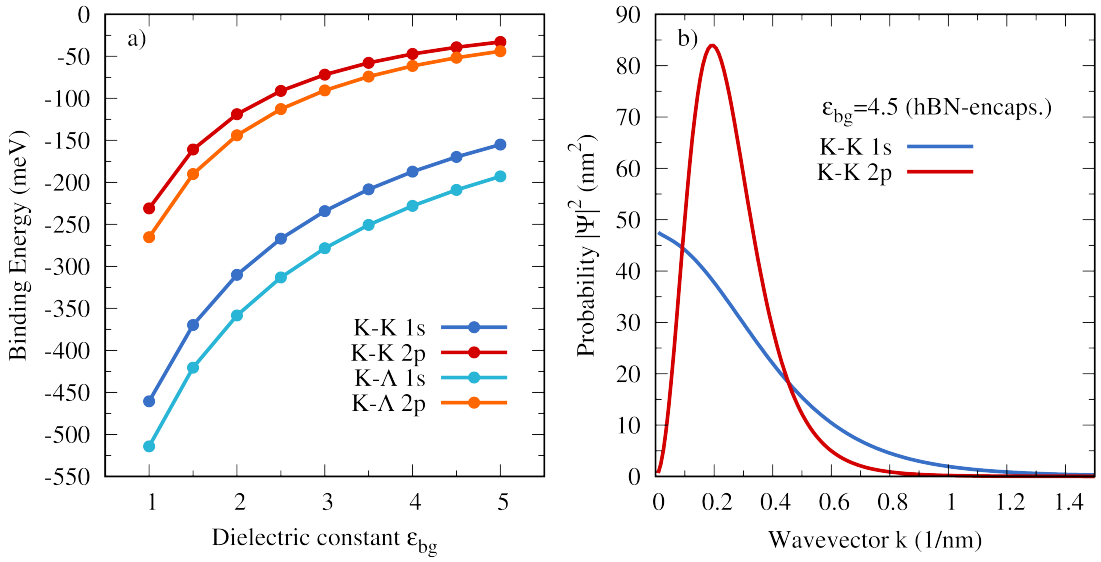

Figure 4.1: a) WSe_2 binding energies for s- ($L = 0$) and p-type ($L = 1$) ground state for K-K and K-Λ excitons as function of the dielectric constant of the environment (average of top and bottom dielectric constants). b)Radial component of the wave functions of the K-K 1s and 2p exciton in momentum space for the dielectric constant $\epsilon_{bg} = 4.5$ (corresponds to hBN encapsulation).

the K point (K-K) we also show the binding energies of an exciton whose electron is at the Λ point and the hole is at K, a so called intervalley exciton, which will be introduced in Sec. 5.3. These excitons have a larger binding energy, since the Λ point has a larger effective mass in the conduction band than the K point. Fig. 4.1a nicely illustrates the most unique aspect of TMD monolayers. While conventional semiconductor platforms used to study excitons, such as GaAs quantum wells have binding energies on the order of some tens of meV, TMD monolayer excitons are bound with energies of up to 0.5 eV, which makes them extremely stable even at room temperature. Figure 4.1b illustrates the wave functions of 1s and 2p K-K excitons in momentum space for an hBN encapsulated sample $\epsilon_{bg} = 4.5$. The corresponding wave functions in real space will have Bohr radii in the range of several nm and therefore extend over several unit cells. Moreover, we see the typical radial shape of p-type wave functions with vanishing probability at $k = 0$. The odd symmetry of p-type states, i.e. $\Psi(\mathbf{k}) = -\Psi(-\mathbf{k})$, is also translated into real space, so that the probability at $r = 0$ (electron and hole at same position) vanishes. Therefore, excitons with $L \neq 0$ can not recombine and are referred to as dark excitons. The numerical calculation needs a sufficiently large and dense momentum grid to converge. In the above calculation $k_{\max} = 5/nm$, 500 k-points and 250 ϕ-points where used, which yields converged results up to a few meV for all considered dielectric environments.

The total exciton energy, Eq. 4.21, is now given by the sum of the binding energy and the electronic transition energy from valence to the conduction band at the

respective valley extrema (single particle band gap). Just as the binding energy, the electronic bandgap differs for intra and intervalley excitons. In Figure 4.2 we show the total energy with respect to the band gap at K for the whole Rydberg series of excitons for the energetically most favourable K-K, K-Λ and K-K' excitons. Apart from the s-type states (solid), we also show the energies of p-type states

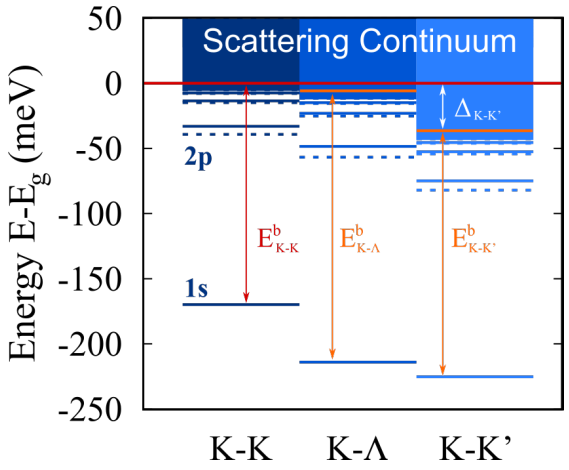

Figure 4.2: Term scheme of the total exciton energies in hBN-encapsulated WSe_2 with respect to the single particle band gap at K. Solid (dashed) lines represent s(p)-type states. While K-Λ excitons have the largest binding energy, the K-K' exciton is the energetically lowest due to a large offset in the single particle band gap resulting from spin orbit coupling.

(dashed). We see that although the K-Λ excitons has the largest binding energy, the K-K' exciton is the lowest in energy due to the large offset in the single particle band gap $\Delta_{K\text{-}K'}$. This results from the spin-orbit coupling induced splitting in the conduction band of about 40 meV and the inverted spin-ordering of bands at K and K', cf. Sec. 3.1.

Apart from the bound exciton states with $E^b < 0$, the solutions of the Wannier equation also contain a continuum of scattering states $E^b > 0$, i.e. with total energy above the band gap. These electron-hole pair states correspond to the free electron-hole plasma. In real space the wave functions of these states are given by plane waves, while their momentum space representation is given by delta functions. However, due to the numerical discretization of the problem we obtain strongly peaked but rapidly oscillating wave functions. These are difficult to treat numerically, when calculating form factors and other excitonic matrix elements. Therefore, throughout this work we focus on the series of bound states up to energies close to the free particle edge.

4.5 Phonon-induced Exciton Dephasing

In the following, we derive an expression for the electron-phonon scattering induced dephasing of coherent excitons, which leads to a decay of the microscopic polarization and the resulting broadening of excitonic resonances. The derivation is carried out along the lines of Refs. [55, 80]. For the sake of clarity, we will restrict the derivation to one valley. The derivation of intervalley scattering is analogue to the one shown below but contains more indices. A convenient way to formally treat scattering between different intervalley excitons is given in Sec. 5.3. Moreover, we focus on a single phonon mode. When neglecting the built up of cross-correlations between different modes, the resulting dephasing is given by a sum over all modes.

We calculate the commutator of the interband polarization with the electron-phonon Hamiltonian and find

$$\partial_t p^{cv}_{\mathbf{k}\mathbf{k}'} \big|_{\text{el-ph}} = \frac{i}{\hbar} \sum_{\mathbf{q}} \left[D^c_{\mathbf{q}} (S^{\mathbf{q}}_{\mathbf{k}+\mathbf{q},\mathbf{k}'} + T^{\mathbf{q}}_{\mathbf{k}+\mathbf{q},\mathbf{k}'}) - D^v_{\mathbf{q}} (S^{\mathbf{q}}_{\mathbf{k},\mathbf{k}'-\mathbf{q}} + T^{\mathbf{q}}_{\mathbf{k},\mathbf{k}'-\mathbf{q}}) \right]$$
$$S^{\mathbf{q}}_{\mathbf{k},\mathbf{k}'} = \langle a^\dagger_{c\mathbf{k}} a_{v\mathbf{k}'} b_{\mathbf{q}} \rangle, \quad T^{\mathbf{q}}_{\mathbf{k},\mathbf{k}'} = \langle a^\dagger_{c\mathbf{k}} a_{v\mathbf{k}'} b^\dagger_{\mathbf{q}} \rangle, \tag{4.31}$$

containing terms for phonon absorption (S) and emission (T) by electrons in conduction and valence bands, respectively. In contrast to the semiconductor Bloch equation presented in Sec. 4.2, a factorization of the appearing two-particle expectation values would vanish, since we assume a thermal phonon bath without coherent phonons ($\langle b \rangle = 0$). Therefore, we go one order higher within the many-particle hierarchy, and as an example compute the equations of motion for S (T is analogue). The appearing many-particle expectation values after evaluating the commutator are consequently factorized according to the cluster expansion scheme. In addition to the Hartree-Fock factorization Eq. 2.31 we make the important approximation,

$$\langle a^\dagger_{c\mathbf{k}} a_{v\mathbf{k}'} b^\dagger_{\mathbf{q}} b_{\mathbf{q}'} \rangle \approx \langle a^\dagger_{c\mathbf{k}} a_{v\mathbf{k}'} \rangle n_{\mathbf{q}} \delta_{\mathbf{q},\mathbf{q}'}, \tag{4.32}$$

with the phonon number $n_{\mathbf{q}} = \langle b^\dagger_{\mathbf{q}} b_{\mathbf{q}} \rangle$, which is approximated by an unperturbed Bose-Einstein distribution (bath approximation). The above step can be considered as Born approximation and is valid in the weak coupling regime, where changes in the bath occupation and interaction induced correlations can be neglected. We further assume low electron densities to neglect band renormalizations and Pauli-blocking, and find,

$$i\hbar \partial_t S^{\mathbf{q}}_{\mathbf{k},\mathbf{k}'} = (\hbar\Omega_{\mathbf{q}} + \varepsilon^v_{\mathbf{k}'} - \varepsilon^c_{\mathbf{k}}) S^{\mathbf{q}}_{\mathbf{k},\mathbf{k}'} + \sum_{\mathbf{l}} V_{\mathbf{l}} S^{\mathbf{q}}_{\mathbf{k}+\mathbf{l},\mathbf{k}'+\mathbf{l}}$$
$$- (D^c_{-\mathbf{q}} p^{cv}_{\mathbf{k}-\mathbf{q},\mathbf{k}'} - D^v_{-\mathbf{q}} p^{cv}_{\mathbf{k},\mathbf{k}'+\mathbf{q}}) n_{\mathbf{q}}. \tag{4.33}$$

Note that we have included the Coulomb Hamiltonian into the equations of motion of the electron-phonon correlation. Since the electron-hole attraction strongly

modifies the energies of available optical transitions, the Coulomb interaction in TMDs can not be treated perturbatively but has to be explicitly included in the treatment of all other interaction processes. Similar as in Sec. 4.3, we can simplify Eq. 4.33 by expanding all dynamic quantities in excitonic basis,

$$S^{\mathbf{q}}_{\mathbf{k},\mathbf{k}'}(t) = \sum_{\nu} S^{\nu}_{\mathbf{k}-\mathbf{k}',\mathbf{q}}(t)\Psi^{\nu}(\alpha\mathbf{k}' + \beta\mathbf{k}) \tag{4.34}$$

together with the exciton expansion for p we thus obtain,

$$i\hbar\partial_t S^{\nu}_{\mathbf{Q},\mathbf{q}} = (\hbar\Omega_{\mathbf{q}} - E^{\nu}_{\mathbf{Q}})S^{\nu}_{\mathbf{Q},\mathbf{q}} - \sum_{\mu} \mathcal{D}^{\nu\mu}_{-\mathbf{q}} P^{\mu}_{\mathbf{Q}-\mathbf{q}} n_{\mathbf{q}}, \tag{4.35}$$

$$\mathcal{D}^{\nu\mu}_{\mathbf{q}} = D^{c}_{\mathbf{q}}\mathcal{F}^{\nu\mu}(\beta\mathbf{q}) - D^{v}_{\mathbf{q}}\mathcal{F}^{\nu\mu}(-\alpha\mathbf{q}), \tag{4.36}$$

$$\mathcal{F}^{\nu\mu}(\mathbf{q}) = \sum_{\mathbf{k}} \Psi^{\nu *}(\mathbf{k})\Psi^{\mu}(\mathbf{k}+\mathbf{q}) = \langle\nu|e^{i\mathbf{q}\mathbf{r}}|\mu\rangle, \tag{4.37}$$

where we have introduced the exciton-phonon matrix element $\mathcal{D}^{\nu\mu}_{\mathbf{q}}$ defined by the scattering form factors $\mathcal{F}^{\nu\mu}(\mathbf{q})$. Due to the simple form of Eq. 4.35, we can now solve it within the Markov approximation (Eq. 2.36). It is important to note that the fast oscillation of the polarization $P^{\mu}_{\mathbf{Q}} \propto \exp(iE^{\mu}_{\mathbf{Q}}t)$ has to be split off before performing the adiabatic limit. Finally we plug the solution back into Eq. 4.33 after transforming it into exciton basis. The solution for T can be obtained from the equation of S by setting: $S \to T$, $\Omega_{\mathbf{q}} \to -\Omega_{\mathbf{q}}$ and $n_{\mathbf{q}} \to 1 + n_{\mathbf{q}}$. Finally, for energetically well separated exciton resonances, we can neglect off-diagonal couplings $\dot{P}^{\mu} \propto P^{\nu}$ with $\mu \neq \nu$, which yields the phonon-induced exciton dephasing,

$$\dot{P}^{\mu}_{\mathbf{Q}}\big|_{\text{el-ph}} = -\frac{1}{\hbar}\Gamma^{\mu}_{\mathbf{Q}} P^{\mu}_{\mathbf{Q}}. \tag{4.38}$$

$$\Gamma^{\mu}_{\mathbf{Q}} = \pi \sum_{\pm,j,\nu,\mathbf{q}} |\mathcal{D}^{\mu\nu}_{j\mathbf{q}}|^2 (\frac{1}{2} \pm \frac{1}{2} + n_{j\mathbf{q}})\delta(E^{\nu}_{\mathbf{Q}+\mathbf{q}} - E^{\mu}_{\mathbf{Q}} \pm \hbar\Omega_{j\mathbf{q}}), \tag{4.39}$$

where we have added the summation over different phonon modes j. We can interpret the above equations as loss of coherence due to scattering with phonons. This leads to a decay of the coherent exciton Eq. 4.38 with a decay constant Γ, which is the inverse coherence lifetime and determines the exciton linewidth. The latter is given by a sum over all energy and momentum conserving exciton-phonon scattering channels as dictated by Fermi's Golden Rule. Here phonon absorption $(-)$ requires the presence of phonons and is therefore proportional to $n_{\mathbf{q}}$. In contrast, phonon emission $(+)$ can take place spontaneously $(\propto 1)$ or is stimulated $\propto n_{\mathbf{q}}$. Moreover, each scattering channel is weighted by a probability rate given by the exciton-phonon matrix element Eq. 4.36. In the following, we

will discuss this matrix element and point out the crucial modifications it creates compared to a pure electron-phonon scattering.

First of all we find that the excitonic matrix element is given by two contributions, reflecting the individual scattering of either the electron or the hole. When focusing on state-conserving scattering $\nu = \mu$, the limit $\mathbf{q} \to 0$ yields $\mathcal{F}^{\mu\mu} \approx 1$ and $\mathcal{D}^{\mu\mu}_{\mathbf{q}} \approx D^c_{\mathbf{q}} - D^v_{\mathbf{q}}$. Hence, in the case of $D^c_{\mathbf{q}} = D^v_{\mathbf{q}}$ the exciton phonon coupling vanishes. This is because D is a measure of the change in electronic energy induced by the lattice deformation. If electron and hole energy are changed equally, the exciton energy $\propto \varepsilon^c - \varepsilon^v$ is unaffected. Therefore, excitonic matrix elements always reflect the asymmetry between electron and hole matrix elements. Another important excitonic feature becomes apparent for large $\mathbf{q}$, where the wave function overlap, determining the form factor Eq. 4.37 vanishes. This is a consequence of the composite nature of the exciton. Since the change of CoM momentum of the exciton is mediated by the individual scattering of the electron/hole, the relative motion of the electron-hole pair is also affected. The latter, however, is fixed to orbitals dictated by the Coulomb interaction, so that the scattering is only allowed within the momentum uncertainty described by $\Psi^\mu(\mathbf{k})$. Consequently, excitons with large binding radii, i.e. large position uncertainty, have lower momentum uncertainty and can therefore only absorb smaller phonon momenta without changing the orbital. This train of thoughts is supported with numerical calculations and a comparison to the experiment in Paper 2, which will be discussed in Sec. 4.7.

Numerical Evaluation of Scattering Integrals

In the following we discuss the evaluation of scattering integrals containing δ-functions, such as the phonon-induced dephasing rate Eq. 4.39. In general, these integrals have the form

$$I(\mathbf{k}) = \int dq \int d\phi S(\mathbf{k},q,\phi)\delta(E(\mathbf{k},q,\phi)), \tag{4.40}$$

where S contains the relevant matrix element and occupation numbers and E abbreviates the energy difference between initial and final states. It is important to note that the δ-function is one-dimensional and can be used to either simplify the q- or the ϕ-integration. Depending on the functions S and E we might have to choose differently, as will become clear further below. Assuming a function g that has simple roots x_i^0 it holds,

$$\int dx f(x)\delta(g(x)) = \sum_i \frac{f(x_i^0)}{|g'(x_i^0)|}. \tag{4.41}$$

Hence, we can treat ϕ as a parameter, and find the roots $q_i^0[\mathbf{k},\phi]$ with $E(\mathbf{k},q_i^0[\mathbf{k},\phi],\phi) = 0$. With this choice it holds,

$$I(\mathbf{k}) = \sum_i \int d\phi \frac{S(\mathbf{k},q,\phi)}{|\partial_q E(\mathbf{k},q,\phi)|} \Bigg|_{q=q_i^0[\mathbf{k},\phi]}. \tag{4.42}$$

However, the above expression can be divergent if the denominator becomes zero for certain $\mathbf{k}$ and ϕ values. In these cases, one needs to check if the singularity is removable by cancelling with a factor of S or we choose q as parameter and apply the rule Eq. 4.41 with ϕ as variable. Another option is to change the integrated momentum. In the above example we calculate the scattering integral of a state at momentum $\mathbf{k}$ by integrating over all scattering processes with momentum transfer $\mathbf{q}$. Instead, we could shift the momentum sum towards the final state, i.e. $\mathbf{q} \to \mathbf{k} + \mathbf{q} = \mathbf{k}'$.

In the case of the phonon-induced dephasing Eq. 4.39 the best choice depends on the type of phonon mode. For the case of acoustic phonons (energy scales linearly with $\mathbf{q}$, we can integrate over the phonon momentum $\mathbf{q}$ and obtain a removable singularity. In contrast, for optical phonons (constant energy) a straightforward application of the above procedure is only possible when integrating over the final state momentum $\mathbf{k}'$ (singularity at $\mathbf{k}' = 0$ can be removed).

For the generic case of non-parabolic bands, there is no recipe of how to treat singularities in the scattering integral. Since the δ-function results from the Markov approximation (Sec. 2.3) in the limiting case of $\gamma \to 0$, it is reasonable to numerically evaluate the δ-functions by replacing it with a narrow Lorentzian of width γ. However, if the final result does not converge for small γ, a self-consistent calculation of the scattering rate via the complex self-energy might be considered.

4.6 Absorption Spectrum and Radiative Damping

With the response spectrum of coherent excitons Eq. 4.24 and the phonon-induced dephasing Eq. 4.38 we have considered the intrinsic microscopic processes shaping the coherent optical properties of TMDs. In the following we derive an expression for the self-consistent optical absorption of a 2D material along the lines of Ref. [37].

First of all we rewrite the excitonic susceptibility (Eq. 4.24):

$$\chi_\sigma(\omega) = \frac{e_0^2}{m_0^2 \epsilon_0 A \omega^2} \sum_\mu \frac{|\mathcal{M}_\sigma^\mu|^2}{\hbar\omega - E_0^\mu - i\Gamma_0^\mu} \equiv \frac{2nc}{\omega}\xi_\sigma(\omega) \tag{4.43}$$

$$\xi_\sigma(\omega) = \sum_\mu \frac{\gamma_\sigma^\mu}{\hbar\omega - E_0^\mu - i\Gamma_0^\mu} \quad \text{and} \quad \gamma_\sigma^\mu \approx \frac{\hbar e_0^2 |\mathcal{M}_\sigma^\mu|^2}{2m_0^2 \epsilon_0 A n c E_0^\mu}, \tag{4.44}$$

introducing the unitless function ξ and the radiative damping γ^μ which will be discussed below. While for weakly absorbing 3D materials the absorbance is given by $\alpha = 2\mathrm{Im}\{\xi\}$, in 2D materials with strong matter-light interaction, the coupling to the re-emitted light has to be taken into account self-consistently. When a 2D material is illuminated with a perpendicularly propagating plane wave $\mathbf{E}^0$, we can use the inhomogeneous wave equation Eq. 4.1 to determine the total field amplitude within the monolayer plane, which yields [37]

$$E_i(z=0,\omega) = E_i^0(z=0,\omega) + i\mu_0 \frac{\omega c}{2n} P_i(\omega). \tag{4.45}$$

Consequently, the electrical field driving the microscopic polarization is not the initial laser field $\mathbf{E}^0$ anymore, but the total field which is modified by the coherent emission of the oscillating exciton. Hence, we set $P_i = \epsilon_0 \chi_i E_i = \epsilon_0 \chi_i E_i^0 + i\xi_i P_i$. With this self-consistent treatment of the matter-light interaction, the excited polarization is creating a counter-acting field, which damps its own oscillation. From Eq. 4.45 we can deduce the transmitted (T) and reflected fraction (R) of the light field amplitude. Finally using $\alpha = 1 - |T|^2 - |R|^2$ we find the radiatively damped absorption coefficient,

$$\alpha_\sigma(\omega) = \frac{2\mathrm{Im}\{\xi_\sigma(\omega)\}}{1 + |\xi_\sigma(\omega)|^2 + 2\mathrm{Im}\{\xi_\sigma(\omega)\}} \tag{4.46}$$

$$\approx \sum_\mu \frac{2\gamma_\sigma^\mu \Gamma_0^\mu}{(E_0^\mu - \hbar\omega)^2 + (\Gamma_0^\mu + \gamma_\sigma^\mu)^2}, \tag{4.47}$$

where in the second line we have plugged in the excitonic response function and neglected interference terms in the denominator, assuming energetically well separated resonances. Figure 4.3 shows a typical excitonic absorption spectrum.

Each s-type exciton state appears as a Lorentzian resonance at its eigenenergy. Thereby, the oscillator strength is decreasing with the main quantum number, due to increasing orbitals (cf. discussion of radiative broadening in Sec. 4.7). The linewidth of those resonances is given by the coherence life time of the corresponding exciton, which becomes smaller with increasing temperature due to enhanced exciton phonon-scattering.

In Eq. 4.47 we can read of that both, the exciton-phonon scattering Γ as well as the radiative damping,

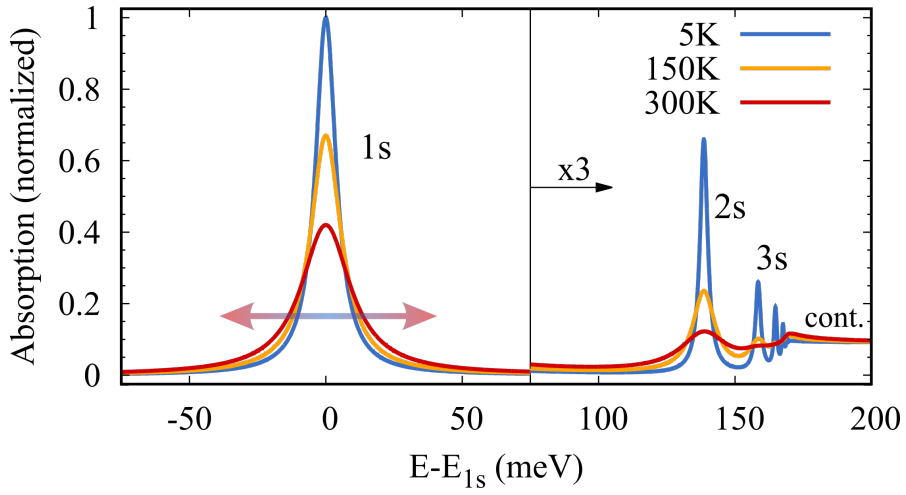

Figure 4.3: Calculated absorption spectrum for an hBN-encapsulated WSe_2 monolayer at different temperatures. Figure adopted from Paper 2.

$$\gamma_\sigma^\mu = \frac{\hbar e_0^2 |M_\sigma^{cv}|^2}{2m_0^2 \epsilon_0 A n c E_0^\mu} |\sum_{\mathbf{k}} \Psi^\mu(\mathbf{k})|^2, \tag{4.48}$$

lead to a broadening of exciton resonances. Both these mechanisms limit the lifetime of the coherent exciton polarization P^μ. An equivalent damping term as found for phonon-scattering in the equation of motion of P^μ can also be found for the radiative dephasing, by either plugging Eq. 4.45 into the semiconductor Bloch equations [55, 81] or a fully quantized treatment of the matter-light interaction via $H_{\text{el-pt}}$ in second order Born-Markov approximation (Sec. 6.2). In both cases we find,

$$\partial_t P_{\mathbf{Q}}^\mu = -\frac{1}{\hbar} \sum_\sigma \gamma_\sigma^\mu P_{\mathbf{Q}}^\mu \delta_{\mathbf{Q},\mathbf{0}}. \tag{4.49}$$

The dephasing rates derived above are key parameters determining the shape of the excitonic absorption spectrum and reveal information about the properties and dynamics of excitons. In particular, the presented model allows us to interpret the change in the exciton linewidth under different experimental situations. Here the phonon-induced broadening contains information about available exciton scattering channels and can therefore be used to deduce important statements about the dynamics of excitons [55, 58].

4.7 Linewidth of Higher Exciton States in WSe_2 Monolayers

While conventional semiconductor platforms for the study of exciton properties, e.g. GaAs quantum wells, usually only exhibit one distinguishable exciton resonance, the significantly increased Coulomb interaction in TMDs and the related increase in exciton binding energies allows us to spectrally resolve several excited excitons between ground state and band edge. In particular the recently developed method of encapsulating monolayers with hexagonal boron nitride (hBN) reduces the disorder induced inhomogeneous broadening of spectral lines (Paper 15), making the intrinsic linewidth of excitons accessible in experiments. The position of excitonic resonances in the absorption spectrum provides information about the binding energies and thus the Coulomb forces in the system [16, 82]. In addition to that, the linewidth is a measure for the lifetime of the induced optical coherences and therefore can provide important information about the many-particle scattering processes [55, 58, 83–86].
In Paper 2 we have numerically evaluated the above derived microscopic model of the exciton linewidth for the exemplary case of WSe_2 monolayers and compared the results with experimentally measured linewidths extracted from reflection contrast measurements on hBN encapsulated samples. In particular, we thereby focused on the broadening of higher excitonic states 2s and 3s, which in simply exfoliated samples can not be systematically studied due to their low oscillator strength and strong inhomogeneous broadening, but become visible in hBN encapsulated monolayers over a large range of temperatures.

Figure 4.4(a) schematically illustrates the exciton band structure and relevant scattering mechanisms. Excitons are excited at zero center-of-mass momentum and can either decay by radiative recombination (yellow) with a rate given by the radiative broadening γ^μ or scatter into a state with a non-zero center-of-mass momentum via interaction with phonons, quantified by the phonon-induced broadening Γ^μ. Apart from intravalley scattering via absorption of – mostly low energy acoustic – phonons (orange) or transitions into lower lying states after emission of a phonon (red), the electron or hole can scatter into a different valley (blue) giving rise to indirect intervalley excitons.

In Sec. 4.5 we have focused our derivation on intravalley processes for the sake of clarity. However, intervalley scattering channels can be included into the model with some small modifications as will be shown in Sec. 5.3. In Paper 2 we quantitatively analyse the temperature dependence of the linewidth of the 1s, 2s and 3s exciton by decomposing it into different scattering channels and discuss in detail the comparison between experiment and theory. In the following, we will only discuss the central outcome of our investigation.

Fig. 4.4 (b) shows the calculated full width at half maximum of exciton absorp-

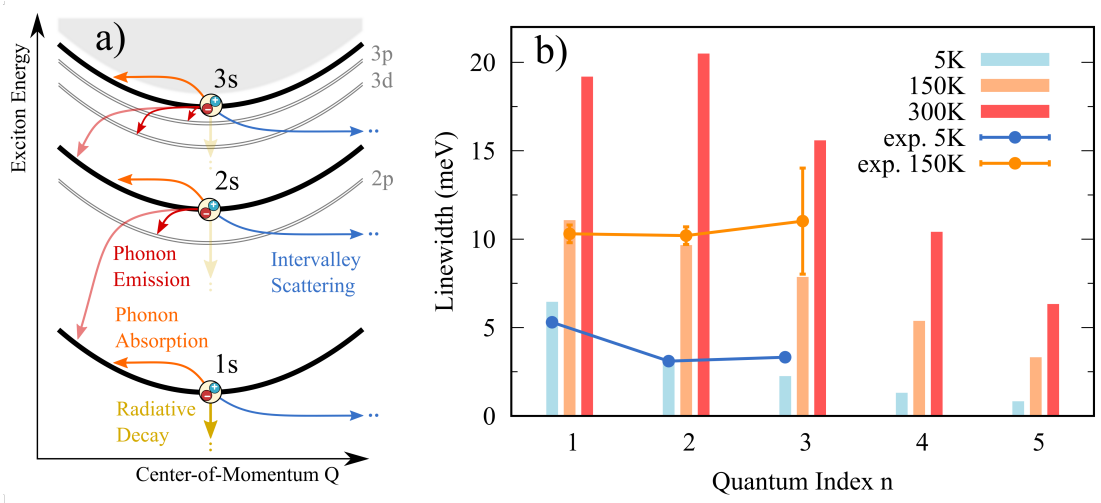

Figure 4.4: Exciton dephasing mechanisms. a) Schematic illustration of the exciton bandstructure and possible scattering mechanisms. Radiative recombination or scattering into a dark state with finite center-of-mass momentum via interaction with phonons leads to a broadening of exciton absorption lines. b) The linewidth of bright ns excitons as function of n for dfferent temperatures. Our microscopic model yields a decreasing trend for high n resulting from a reduced scattering efficiency for excited states. Figures adopted from Paper 2.

tion lines (s-type states) as a function of the principal quantum number n for three different temperatures. Moreover, the model (represented as bars) is directly compared to the experimentally measured values (points). Apart from the case of the 2s exciton at room temperature, we find – in reasonable agreement with the experiment – a general decrease of the linewidth with increasing quantum index n [87, 88]. This result at first sight contradicts the physical intuition, since excited states have a larger phase space of lower lying states to scatter into. To understand the observed behaviour we have to consider the influence of exciton wave functions on radiative and non-radiative scattering probabilities.
For the radiative damping (Sec. 4.6) it holds,

$$\gamma_\sigma^\mu \propto |\sum_{\mathbf{k}} \Psi^\mu(\mathbf{k})|^2 \propto |\Psi^\mu(\mathbf{r}=0)|^2. \tag{4.50}$$

Hence the radiative broadening (proportional to to the exciton recombination rate) scales with the probability of finding electron and hole at the same spatial position. With increasing index n the orbital functions become larger in space, so that the probability distribution is more widely spread, which reduces its value at $\mathbf{r} = 0$ and thereby the excitons oscillator strength.
At the same time the larger orbitals of excited states correspond to narrower wave functions in momentum space. Since the exciton-phonon matrix element is given by the overlap of initial and final state in momentum space, cf. Eq. 4.36, larger exciton radii lead to a reduction of scattering probabilities. This is similar to

the Heisenberg uncertainty principle, in the sense that a weaker localization in space yields smaller momentum uncertainties and therefore a reduced tolerance for momentum transfers. The overall good comparison between the theoretically predicted intrinsic scattering rates and the actually measured broadening indicates that the studied hBN encapsulated samples are only weakly influenced by inhomogeneities, which is further elaborated on in Paper 15. Moreover, in Paper 17 we investigated the impact of elastic impurity scattering on the linewidth of different exciton states. Here we find similar behaviour with increasing quantum index as observed for scattering with phonons. However, due to the lack of resonant states, the elastic scattering with impurities is strongly suppressed in the ground state, while phonon-scattering is very efficient. Finally, in Paper 13 we analysed how the excitonic linewidth changes in different TMDs when applying strain. Here the strain gives rise to valley dependent changes in band masses and energies, which modifies the efficiency of different exciton-phonon scattering channels, depending on the energetic arrangement of bright and dark excitons states.

CHAPTER 5

EXCITON HAMILTONIAN

The considerations of the last section have shown that the Coulomb interaction between electrons and holes completely restructures the eigenenergies of transitions between conduction and valence band. For non-interacting electrons, the interband transition energies are simply given by the band gap at the respective momentum. In Sec. 4.2 we found that the Coulomb interaction couples polarizations at different momenta, giving rise to new resonance energies. Therefore, it is from a conceptional as well as mathematical point of view convenient to perform a basis transformation. Instead of using coupled plane waves as electron-hole pair basis, we rather use the excitonic Rydberg series of bound and scattering states as reference point to describe the excitation kinetics, such as illustrated in Figure 5.1.

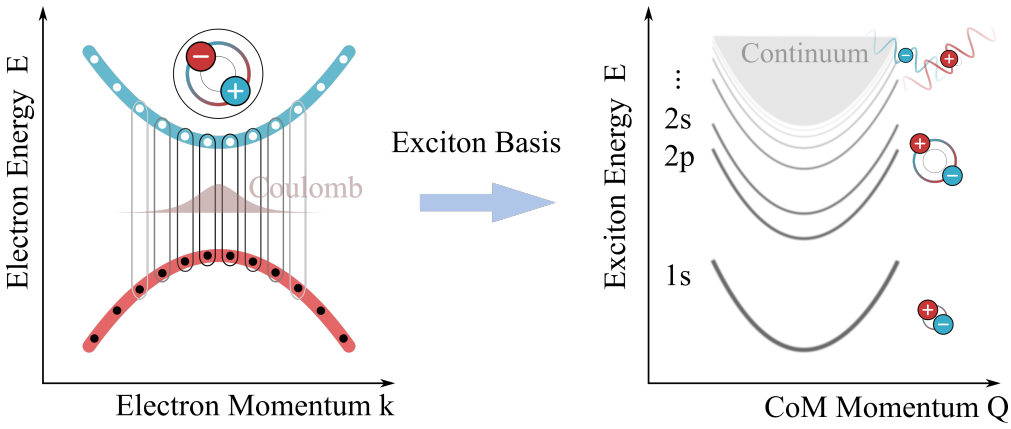

Figure 5.1: Illustration of the exciton in free electron-hole pair basis (left) and in the excitonic picture (right).

In Sec. 4.2 we showed that the equations of motion related to interband transitions can be drastically simplified by expanding them in terms of excitonic wave functions. In principle, this basis transformation can also be done in other equations of motion, e.g. for higher order electron-hole correlations describing incoherent exciton densities. However, the derivations of Coulomb contributions to the equations of motion in the electron-hole picture are often quite cumbersome and the exciton basis transformation also becomes more complex when dealing with e.g. three-particle correlations. Therefore it is convenient to apply the Hartree-Fock approximation and low-excitation limit directly on the level of the Hamiltonian and transform the electron-hole operators into exciton basis [89–92]. This step dramatically simplifies the derivation of equations of motion and allows to study higher order processes such as exciton-exciton interaction (Paper 30) [92, 93] thanks to a reduced number of operators in play. The transformation procedure shown in this section has a rather empirical character, but the resulting Hamiltonian has the same form as obtained in more sophisticated theoretical approaches towards excitonic Hamiltonians [92]. While the exciton Hamiltonian formalism is used to present the theoretical models in the following sections, all presented equations have been verified to be equivalent to the results obtained with an analogous calculation using fermionic operators for electrons and assuming low densities (f_e,$f_h << 1$).

5.1 Excitonic Pair Operators

We first focus on one electronic valley to illustrate the principle and later introduce valley quantum numbers to include intervalley excitons. The first step towards an excitonic Hamiltonian is the definition of electron-hole pair operators A as combination of conduction and valence band electrons:

$$A^\dagger_{\mathbf{k}\mathbf{k}'} = a^\dagger_{c\mathbf{k}} a_{v\mathbf{k}'} \tag{5.1}$$

$$[A_{\mathbf{k}_1\mathbf{k}_2}, A^\dagger_{\mathbf{k}_3\mathbf{k}_4}] = \delta_{\mathbf{k}_1\mathbf{k}_3}\delta_{\mathbf{k}_2\mathbf{k}_4} - B_{\mathbf{k}_1\mathbf{k}_2\mathbf{k}_3\mathbf{k}_4} \approx \delta_{\mathbf{k}_1\mathbf{k}_3}\delta_{\mathbf{k}_2\mathbf{k}_4} \tag{5.2}$$

$$B_{\mathbf{k}_1\mathbf{k}_2\mathbf{k}_3\mathbf{k}_4} = a_{v\mathbf{k}_4} a^\dagger_{v\mathbf{k}_2}\delta_{\mathbf{k}_1\mathbf{k}_3} + a^\dagger_{c\mathbf{k}_3} a_{c\mathbf{k}_1}\delta_{\mathbf{k}_2\mathbf{k}_4} \tag{5.3}$$

Here the term B accounts for the fermionic substructure of the pair operators and inter alia gives rise to Pauli blocking. In the low excitation limit considered in this work, we set $B = 0$ and obtain a fully bosonic commutation of electron-hole excitations. In order to describe the full Hamiltonian in terms of pair creation operators, we now need to find a way to express intraband transitions, such as $a^\dagger_{c\mathbf{k}_1} a_{c\mathbf{k}_2}$, as combinations of interband operators A. Since the many-particle dynamics of the system is fully determined by the commutator with the Hamiltonian, we can change the representing operators when conserving the underlying commutation

relations. As an example, we consider the following equivalent commutators

$$\begin{aligned}[a^\dagger_{c\mathbf{k}_1} a_{c\mathbf{k}_2}, A^\dagger_{\mathbf{k}_3\mathbf{k}_4}] &= [a^\dagger_{c\mathbf{k}_1} a_{c\mathbf{k}_2}, a^\dagger_{c\mathbf{k}_3} a_{v\mathbf{k}_4}] = a^\dagger_{c\mathbf{k}_1} a_{v\mathbf{k}_4} \delta_{\mathbf{k}_2\mathbf{k}_3} \\ &= A^\dagger_{\mathbf{k}_1\mathbf{k}_4} \delta_{\mathbf{k}_2\mathbf{k}_3} \approx \sum_i [A^\dagger_{\mathbf{k}_1\mathbf{k}_i} A_{\mathbf{k}_2\mathbf{k}_i}, A^\dagger_{\mathbf{k}_3\mathbf{k}_4}]. \end{aligned} \tag{5.4}$$

Similar relations can be shown for A and intraband transitions in the valence band. Consequently, when strictly neglecting the correction factors B, the following substitutions are valid in the Hamiltonian:

$$a^\dagger_{c\mathbf{k}} a_{c\mathbf{k}'} \longrightarrow \sum_{\mathbf{l}} A^\dagger_{\mathbf{kl}} A_{\mathbf{k}'\mathbf{l}} \tag{5.5}$$

$$a_{v\mathbf{k}} a^\dagger_{v\mathbf{k}'} \longrightarrow \sum_{\mathbf{l}} A^\dagger_{\mathbf{lk}} A_{\mathbf{lk}'} \tag{5.6}$$

5.2 Exciton Transformation

Next we transform the electronic Hamiltonian into excitonic basis. To this end we neglect the intraband Coulomb interaction, which for higher densities gives rise to energy renormalization and electron-electron scattering, but in the low excitation regime has no impact on the dynamics of the system. Hence the electronic part of the Hamiltonian can be rewritten as:

$$H_{\text{el}} + H_{\text{Coul}} \to H_{\text{x-0}} = \sum_{\mathbf{kk}'} \left[(\varepsilon^c_{\mathbf{k}} - \varepsilon^v_{\mathbf{k}'}) A^\dagger_{\mathbf{kk}'} - \sum_{\mathbf{q}} V_{\mathbf{q}} A^\dagger_{\mathbf{k+q},\mathbf{k}'+\mathbf{q}} \right] A_{\mathbf{kk}'} \tag{5.7}$$

$$\approx \sum_{\mu\mathbf{Q}} E^\mu_{\mathbf{Q}} X^\dagger_{\mu\mathbf{Q}} X_{\mu\mathbf{Q}}, \tag{5.8}$$

where in the last line we used the expansion into excitonic eigenmodes,

$$A^\dagger_{\mathbf{k}_e\mathbf{k}_h} = \sum_{\mu} X^\dagger_{\mu,\mathbf{k}_e-\mathbf{k}_h} \Psi^\mu(\alpha\mathbf{k}_h + \beta\mathbf{k}_e), \tag{5.9}$$

and used that the wave functions fulfill the Wannier equation (Eq. 4.17). The above applied transformation is completely analogous to the treatment of the Coulomb interaction in the semiconductor Bloch equations Sec. 4.3. It is important to note that the Coulomb interaction is now fully contained within the single

particle energy of the exciton. In the electron picture the Hamiltonian contained many-particle interactions, giving rise to a hierarchy problem in Coulomb correlations. Now the negligence of the fermionic correction term B in Eq. 5.2 has led to an effective single particle problem. With the above described transformation and commutation rules, we have restricted the problem to the low density regime and applied a Hartree-Fock factorization of the Coulomb interaction directly within the Hamiltonian.

We can now transform all other interaction Hamiltonians into exciton basis, where the following substitutions come in handy:

$$a^\dagger_{c\mathbf{k}+\mathbf{q}} a_{c\mathbf{k}} = \sum_{\nu\mu\mathbf{Q}} \Big[\Psi^{\nu *}(\mathbf{k} - \alpha\mathbf{Q})\Psi^{\mu}(\mathbf{k} - \alpha\mathbf{Q} + \beta\mathbf{q})\Big] X^\dagger_{\mu\mathbf{Q}+\mathbf{q}} X_{\nu\mathbf{Q}} \tag{5.10}$$

$$a^\dagger_{v\mathbf{k}} a_{v\mathbf{k}-\mathbf{q}} = -\sum_{\nu\mu\mathbf{Q}} \Big[\Psi^{\nu *}(\mathbf{k} + \beta\mathbf{Q})\Psi^{\mu}(\mathbf{k} + \beta\mathbf{Q} - \alpha\mathbf{q})\Big] X^\dagger_{\mu\mathbf{Q}+\mathbf{q}} X_{\nu\mathbf{Q}}. \tag{5.11}$$

Applying this procedure for example to the electron-phonon Hamiltonian gives rise to a convenient exciton-phonon Hamiltonian:

$$H_{\text{x-ph}} = \sum_{\mu\nu,\mathbf{q}\mathbf{Q}} \mathcal{D}^{\nu\mu}_{\mathbf{q}} X^\dagger_{\mu,\mathbf{Q}+\mathbf{q}} X_{\nu,\mathbf{Q}} (b_{\mathbf{q}} + b^\dagger_{-\mathbf{q}}), \tag{5.12}$$

where the exciton-phonon matrix element $\mathcal{D}^{\nu\mu}_{\mathbf{q}}$ is given by the Eq. 4.36, which we already found via transformation of the equations of motion.

Before we show the other Hamiltonians in exciton frame, we will extend the set of basis functions to intervalley excitons, which represent an important phonon scattering channel.

5.3 Indirect Excitons and Intervalley Phonon Scattering

So far all discussions about excitons where referring to electron hole pairs within the same valley, e.g. the K point. However, the electron and hole momenta entering the Wannier equation, discussed in Sec. 4.3, always referred to the minimum of the parabolically approximated band structure (valley). In principle, the electron valley can be different from the hole valley and we would still obtain the same Wannier equation, since the Coulomb matrix element is independent of the distance of electron and hole in momentum space. As long as electron and hole have a positive reduced mass, they can form a bound state, which we refer to as intervalley or indirect exciton.

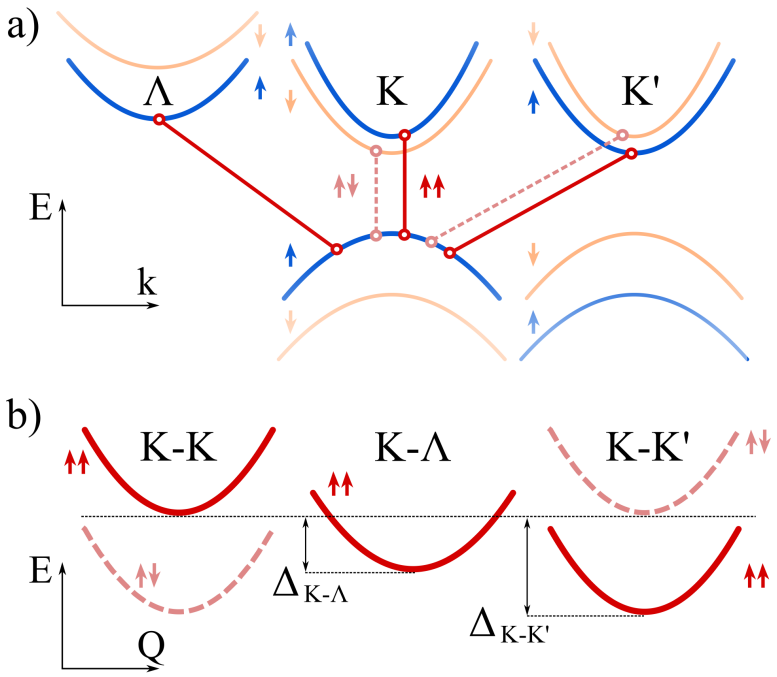

Figure 5.2: Sketch of the a) electronic band structure exhibiting multiple minima and maxima of valence and conduction band and b) corresponding exciton center-of-mass dispersion containing the direct (K-K) exciton as well as several intervalley excitons such as K-K' and K-Λ. Figure adopted from Paper 3.

Figure 5.2 illustrates the relevant minima and maxima of valence and conduction band along with the excitonic center-of-mass dispersion for the 1s ground state, respectively. As result of different binding energies as well as varying electronic band gaps, intervalley excitons, such as K-Λ and K-K', can lie energetically below the direct K-K exciton.
In order to include intervalley excitons into our effective mass model, we divide the Brillouin zone into small neighbourhoods U_ζ of the band extrema/valleys ζ, i.e. $\sum_{\mathbf{k}\in 1.\mathrm{BZ}} \to \sum_{\zeta,\mathbf{k}\in U_\zeta}$, and use the valley as additional (vectorial) quantum number, $a_{c\mathbf{k}} \to a_{c\zeta\mathbf{k}_\zeta}$. In this formalism intervalley excitons can be easily included into the exciton model derived in Sec. 4 and the exciton transformation is given by

$$a^\dagger_{c\zeta_e\mathbf{k}_e} a_{v\zeta_h\mathbf{k}_h} = A^\dagger_{\zeta_e\mathbf{k}_e,\zeta_h\mathbf{k}_h} = \sum_\mu X^\dagger_{\mu\zeta_e\zeta_h,\mathbf{k}_e-\mathbf{k}_h} \Psi^\mu_{\zeta_e\zeta_h}(\alpha_{\zeta_e\zeta_h}\mathbf{k}_h + \beta_{\zeta_e\zeta_h}\mathbf{k}_e), \tag{5.13}$$

with valley dependent mass coefficients $\alpha_{\zeta\zeta'} = m_e^\zeta/M_{\zeta\zeta'}$, $\beta_{\zeta\zeta'} = m_h^{\zeta'}/M_{\zeta\zeta'}$ and $M_{\zeta\zeta'} = m_e^\zeta + m_h^{\zeta'}$. Here the wave functions need to fulfill the intervalley Wannier equation,

$$\frac{(\hbar\mathbf{k})^2}{2m_r^{\zeta_e\zeta_h}} \Psi^\mu_{\zeta_e\zeta_h}(\mathbf{k}) - \sum_{\mathbf{q}} V_{\mathbf{q}} \Psi^\mu_{\zeta_e\zeta_h}(\mathbf{k}+\mathbf{q}) = E^{\mathrm{b}}_{\mu\zeta_e\zeta_h} \Psi^\mu_{\zeta_e\zeta_h}(\mathbf{k}), \tag{5.14}$$

and we finally obtain

$$H_{\text{el}} + H_{\text{Coul}} \rightarrow H_{\text{x-0}} = \sum_{\mu\zeta_e\zeta_h\mathbf{Q}} E^{\mu}_{\zeta_e\zeta_h\mathbf{Q}} X^{\dagger}_{\mu\zeta_e\zeta_h\mathbf{Q}} X_{\mu\zeta_e\zeta_h\mathbf{Q}}, \tag{5.15}$$

$$E^{\mu}_{\zeta_e\zeta_h\mathbf{Q}} = \frac{\hbar^2\mathbf{Q}^2}{2M_{\zeta_e\zeta_h}} + \varepsilon^{c}_{\zeta_e\mathbf{0}} - \varepsilon^{v}_{\zeta_h\mathbf{0}} + E^{\text{b}}_{\mu\zeta_e\zeta_h}. \tag{5.16}$$

In the above equation we see that the inclusion of the Coulomb interaction can change the energetic ordering of direct and indirect transitions. While in the electronic picture the energy of an interband transition is simply given by the energy difference of conduction band minimum and valence band maximum $\varepsilon^{c}_{\zeta_e\mathbf{0}} - \varepsilon^{v}_{\zeta_h\mathbf{0}}$, the exciton ground state of the respective transition is red shifted by the binding energy $E^{1s}_{\zeta_e\zeta_h 0} = \varepsilon^{c}_{\zeta_e\mathbf{0}} - \varepsilon^{v}_{\zeta_h\mathbf{0}} + E^{\text{b}}_{1s,\zeta_e\zeta_h}$. Therefore, a momentum indirect transition which is higher then the direct transition in terms of electronic energies, can be lower in terms of exciton energies.

This is exactly the case in TMD monolayers, where small energetic separations of different electronic valleys and large differences in the exciton binding energies lead to a rearrangement of the energy landscape when considering the Coulomb interaction. This is discussed in more detail and with concrete examples in Sec. 4.4.

Since intervalley exciton states can lie below the optically active K-K exciton [94, 95] they provide an important relaxation channel and have a large impact on the optoelectronic properties in TMDs. In the following, we discuss how scattering between different exciton valleys is included into our model. Throughout this work, the electron-phonon scattering is the only interaction mechanism which can provide large enough momenta to transfer electrons between two valleys. Since the explicit notation of the valleys is quite repetitive and unaesthetic, we will in the following make use of an excitonic super index $\mu = (n_\mu, L_\mu, \zeta^e_\mu, \zeta^h_\mu)$, unifying the main quantum number n_μ and angular momentum L_μ of the relative motion as well as the electron and hole valleys. Similarly, we introduce a compound index for phonon modes $j = (\kappa_j, \zeta^{\text{ph}}_j)$, including the phonon branch κ_j and the nearest high symmetry point ζ^{ph}_j. In this notation, the above introduced exciton transformation yields,

$$H_{\text{el-ph}} = \sum_{\kappa\lambda\zeta\mathbf{k}\zeta'\mathbf{k}'} D^{\kappa\lambda}_{\zeta'\zeta,\mathbf{k}'-\mathbf{k}} a^{\dagger}_{\lambda\zeta',\mathbf{k}'} a_{\lambda\zeta,\mathbf{k}} b_{\kappa,\zeta'-\zeta,\mathbf{k}'-\mathbf{k}} + \text{h.c.}, \tag{5.17}$$

$$\implies H_{\text{x-ph}} = \sum_{\mathbf{Q},\mathbf{q}\nu\mu j} \mathcal{D}^{\mu\nu}_{j\mathbf{q},\mathbf{Q}} X^{\dagger}_{\nu\mathbf{Q}+\mathbf{q}} X_{\mu\mathbf{Q}} b_{j\mathbf{q}} + \text{h.c.}, \tag{5.18}$$

with the exciton-phonon matrix element generalized to intervalley scattering,

$$\begin{aligned}\mathcal{D}^{\mu\nu}_{j\mathbf{q},\mathbf{Q}} = & D^{\kappa_j c}_{\zeta^e_\nu \zeta^e_\mu,\mathbf{q}} \delta_{\zeta^h_\nu \zeta^h_\mu} \delta_{\zeta^{\mathrm{ph}}_j, \zeta^e_\nu - \zeta^e_\mu} \mathcal{F}^{\mu\nu}(\beta_\nu[\mathbf{q} + s_{\nu\mu}\mathbf{Q}]) \\ & - D^{\kappa_j v}_{\zeta^h_\mu \zeta^h_\nu,\mathbf{q}} \delta_{\zeta^e_\nu \zeta^e_\mu} \delta_{\zeta^{\mathrm{ph}}_j, \zeta^h_\mu - \zeta^h_\nu} \mathcal{F}^{\mu\nu}(-\alpha_\nu[\mathbf{q} + s_{\nu\mu}\mathbf{Q}])\end{aligned} \tag{5.19}$$

with $s_{\nu\mu} = 1 - M_\nu/M_\mu$. The form of Eq. 5.18 is analog to the Hamiltonian found for intravalley scattering (Eq. 5.12), however here using super indices, which demonstrates that inter- and intravalley scattering can be formally treated in the same way. For intravalley scattering we also find a similar matrix element, which here however contains delta functions ensuring a) conservation of the electron (hole) valley if the hole (electron) scatters with a phonon, and (b) momentum conservation, i.e. the phonon-valley has to be compatible with the electronic intervalley transition. Moreover, the intervalley matrix element is in general $\mathbf{Q}$-dependent, since the CoM momentum now appears in the scattering form factor, which quantifies the likelihood for a transfer of relative momentum. Since the relative momentum is defined with respect to valley masses, a change of valley leads to an additionally transferred relative momentum. For the range of CoM momenta and exciton masses considered in this work $s_{\nu\mu}\mathbf{Q}$ is usually a small vector, so that this modification only leads to small corrections of the intervalley relaxation dynamics, which has been tested numerically. Since the numerical treatment of a matrix element with two momenta is very time consuming, we use the symmetry conserving approximation $\mathcal{D}^{\mu\nu}_{j\mathbf{q},\mathbf{Q}} \approx (\mathcal{D}^{\mu\nu}_{j\mathbf{q},\mathbf{Q}=\mathbf{0}} + \mathcal{D}^{\nu\mu*}_{j,-\mathbf{q},\mathbf{Q}=\mathbf{0}})/2$.

5.4 Exciton Light Interaction

For all other interaction Hamiltonians considered in this work the electronic valley is conserved, so that the operators can be transformed for each valley separately and according to the rules discussed in Sec. 5.2. For the exciton-photon interaction we find,

$$H_{x-pt} = \sum_{\sigma\mathbf{q},\mu} \tilde{\mathcal{M}}^{\mu}_{\sigma\mathbf{q}} c^\dagger_{\sigma\mathbf{q}} X_{\mu,\mathbf{q}_\parallel} + \mathrm{h.c.} \tag{5.20}$$

$$\text{with} \quad \tilde{\mathcal{M}}^{\mu}_{\sigma\mathbf{q}} = \delta_{\zeta^e_\mu,\zeta^h_\mu} \tilde{M}^{\zeta}_{\sigma\mathbf{q}} \sum_{\mathbf{k}} \Psi^{\mu*}(\mathbf{k}). \tag{5.21}$$

In contrast to the phonon-scattering, the exciton-photon interaction does not conserve the total number of excitons, since it describes a conversion of excitons to photons and vice versa. The excitonic oscillator strength $\propto \sum_{\mathbf{k}} \Psi(\mathbf{k}) = \Psi(\mathbf{r} = 0)$, reflects the fact that excitons can only recombine if the probability of finding an electron and hole at the same position is not zero (as, e.g., for p-type wave functions).

Finally, we transform the semi-classical intraband electron-light coupling, which yields

$$H_{\text{x-intra}} = \sum_{\nu\mu\mathbf{Q}} \mathbf{A} \cdot \boldsymbol{\mathcal{J}}^{\nu\mu}_{\mathbf{Q}} X^{\dagger}_{\mu\mathbf{Q}} X_{\nu\mathbf{Q}} \tag{5.22}$$

$$\begin{aligned} \boldsymbol{\mathcal{J}}^{\nu\mu}_{\mathbf{Q}} &= \delta_{\zeta^e_\nu,\zeta^e_\mu}\delta_{\zeta^h_\nu,\zeta^h_\mu} \sum_{\mathbf{k}} \Psi^{\nu *}(\mathbf{k})(\mathbf{j}^{c}_{\zeta^e \mathbf{k}+\alpha\mathbf{Q}} - \mathbf{j}^{v}_{\zeta^h \mathbf{k}-\beta\mathbf{Q}})\Psi^{\mu}(\mathbf{k}) \\ &= \delta_{\zeta^e_\nu,\zeta^e_\mu}\delta_{\zeta^h_\nu,\zeta^h_\mu} \frac{e_0\hbar}{m_r^{\zeta^e\zeta^h}} \sum_{\mathbf{k}} \Psi^{\nu *}(\mathbf{k})\mathbf{k}\Psi^{\mu}(\mathbf{k}), \end{aligned} \tag{5.23}$$

where we have plugged in the current matrix element for a parabolic band structure in the second step. Eq. 5.22 shows that optically induced intraband currents can drive transitions between different exciton states, which is further elaborated on in Sec. 7.3.

With the above derived exciton Hamiltonian, together with the transformation rules for electronic operators, we can express all observables relevant in this thesis as expectation values of exciton operators and quantify transition rates in terms of excitonic matrix elements. Since the Coulomb interaction is implicitly included, this step dramatically simplifies the derivation of dynamical equations and allows us to read of excitonic effects directly on the level of the Hamilton operator.

CHAPTER 6

PHOTOLUMINESCENCE

Complementary to the linear absorption spectroscopy presented in Sec. 4.1, another common technique to optically characterize materials is to measure the photoluminescence (PL) spectrum. Here the material is excited with a fixed wavelength above the bandgap and the (delayed) light emission from the material is measured as function of frequency. Similar to absorption spectra, the PL gives access to the energies of optically active states in the material, but has some crucial advantages. On one hand, the PL signal is measured at frequencies far away from the excitation energy. Therefore very weak signals can be resolved by using extremely sensitive detectors after filtering out the laser light used for the excitation. On the other hand, the PL results from spontaneous recombination of electrons and holes, which have relaxed to low energy states after they have been excited. Therefore, the PL signal is not only reflecting the oscillator strength of a state, but also contains information about the (incoherent) occupation of this state [96, 97]. As a result, the low temperature emission can reveal quantum states with very weak matter-light coupling, which only become measurable due to a large occupation probability.

In this chapter we investigate the spontaneous light emission from TMDs due to the recombination of incoherent exciton populations. In particular, we derive how momentum indirect dark excitons can become visible in low temperature PL spectra, revealing a fingerprint of phonon-assisted recombination processes.

6.1 Incoherent Photon Emission

To derive an expression for the incoherent light emission, we consider the energy balance of the electromagnetic field. The PL signal is equivalent to the energy flux $\mathbf{S}$ of the electromagnetic field, which obeys the continuity equation

$$\nabla \cdot \mathbf{S} = -\partial_t \rho_{\mathrm{EM}}, \tag{6.1}$$

where ρ_{EM} is the energy density of the electromagnetic field. Assuming that the PL detector integrates over an infinitely large sphere, we can use Gauss law to obtain the radiation power

$$P_{\mathrm{rad}} = \oint \mathbf{dA} \cdot \mathbf{S} = \partial_t \int d^3r \frac{1}{2}(\varepsilon_0 \mathbf{E}^2 + \frac{1}{\mu_0}\mathbf{B}^2) \tag{6.2}$$

$$= \sum_{\sigma\mathbf{q}} \hbar\omega_{\mathbf{q}} \partial_t \langle c^\dagger_{\sigma\mathbf{q}} c_{\sigma\mathbf{q}} \rangle = \int d\omega \hbar\omega I(\omega,t). \tag{6.3}$$

In the second line we have used the expansion of the electromagnetic field in terms of photon creation and annihilation operators, cf. Sec. 2.1, and introduced a spectral power density, which determines the PL spectrum (photon flux)

$$I(\omega,t) = \sum_{\sigma\mathbf{q}} \partial_t n^{\mathrm{pt}}_{\sigma\mathbf{q}}(t) \delta(\omega - \omega_{\mathbf{q}}) \tag{6.4}$$

as a measure for the temporal change of the photon number $n^{\mathrm{pt}}_{\sigma\mathbf{q}} = \langle c^\dagger_{\sigma\mathbf{q}} c_{\sigma\mathbf{q}} \rangle$. Hence, to calculate the emission spectrum of a material, we have to consider the equation of motion of the photon numbers, which are coupled to the excitonic system through exciton-photon Hamiltonian. In the following sections we consider different orders of many-particle correlations within the hierarchy of exciton-photon/phonon correlations, giving rise to a variety of intriguing spectral phenomena within the PL. It is important to note that the photon density $n^{\mathrm{pt}}_{\mathbf{q}} = |\langle c^\dagger_{\mathbf{q}} \rangle|^2 + \delta\langle c^\dagger_{\mathbf{q}} c_{\mathbf{q}} \rangle$ contains a coherent part $|\langle c^\dagger_{\mathbf{q}} \rangle|^2$ and a purely quantum mechanical contribution $\delta\langle c^\dagger_{\mathbf{q}} c_{\mathbf{q}} \rangle$. In the following we consider the incoherent limit, where the electrical field amplitude of the emitted light $\langle E \rangle \propto \langle c^\dagger_{\mathbf{q}} \rangle$ vanishes. This is the case when the emitting excitonic system is in an incoherent state, which in our theoretical framework means that there are no coherent polarizations $p^{cv} \propto \langle X^\dagger \rangle = 0$.

6.2 Luminescence Bloch Equations and Elliot Formula

In the following we derive a luminescence formula reflecting the direct radiative recombination of incoherent bright excitons. To this end we calculate the equation

of motion for the photonic density matrix $n^{\sigma\sigma'}_{\mathbf{k}\mathbf{k}'} = \langle c^\dagger_{\sigma\mathbf{k}} c_{\sigma'\mathbf{k}'}\rangle$ including H_0 and the exciton photon coupling yielding ($\tilde{\mathcal{M}} \to \mathcal{M}$),

$$\partial_t n^{\sigma\sigma'}_{\mathbf{k}\mathbf{k}'} = i(\omega_{\sigma\mathbf{k}} - \omega_{\sigma'\mathbf{k}'}) n^{\sigma\sigma'}_{\mathbf{k}\mathbf{k}'} + \frac{i}{\hbar}\sum_\mu (\mathcal{M}^{\mu *}_{\sigma'\mathbf{k}'} \mathcal{S}^{\mu *}_{\sigma'\mathbf{k}'} - \mathcal{M}^{\mu}_{\sigma'\mathbf{k}'} \mathcal{S}^{\mu}_{\sigma\mathbf{k}}) \tag{6.5}$$

$$\implies \partial_t n^{\mathrm{pt}}_{\sigma\mathbf{q}} = \frac{2}{\hbar}\sum_\mu \mathrm{Im}\{\mathcal{M}^\mu_{\sigma\mathbf{q}} \mathcal{S}^\mu_{\sigma\mathbf{q}}\} \quad \text{with} \quad \mathcal{S}^\mu_{\sigma\mathbf{q}} = \langle c^\dagger_{\sigma\mathbf{q}} X_{\mu\mathbf{q}_\parallel}\rangle, \tag{6.6}$$

where we have introduced the recombination amplitude $\mathcal{S}^\mu_{\sigma\mathbf{q}}$. Next we determine the dynamics of $\mathcal{S}$ which yields,

$$i\hbar\partial_t \mathcal{S}^\mu_{\sigma\mathbf{q}} = (E^\mu_{\mathbf{q}_\parallel} - \hbar\omega_{\sigma\mathbf{q}})\mathcal{S}^\mu_{\sigma\mathbf{q}} + \sum_{\sigma'\mathbf{q}'} \mathcal{M}^{\mu *}_{\sigma'\mathbf{q}'} n^{\sigma\sigma'}_{\mathbf{q}\mathbf{q}'} - \mathcal{M}^{\mu *}_{\sigma\mathbf{q}} N^\mu_{\mathbf{q}_\parallel}. \tag{6.7}$$

Here we have introduced the exciton density $N^\mu_{\mathbf{Q}} = \langle X^\dagger_{\mu\mathbf{Q}} X_{\mu\mathbf{Q}}\rangle$ and set intraexciton coherences to zero, i.e. $\langle X^\dagger_\nu X_\mu\rangle = \delta_{\nu\mu} N^\mu$ [98]. The term $\propto n^{\sigma\sigma'}_{\mathbf{q}\mathbf{q}'}$ accounts for absorption and stimulated emission of photons (diagonal contributions) as well as radiative damping (off-diagonal terms). Here we consider an open-quantum system and can therefore neglect the re-absorption and stimulated emission of photons ($n^{\mathrm{pt}}_{\sigma\mathbf{q}} << N^\mu_{\mathbf{Q}}$). However, we include the radiative damping, by solving Eq. 6.5 in Markov approximation and plugging the result in Eq. 6.7. Similar to the coherent limit we neglect radiative couplings $\dot{\mathcal{S}}^\mu \propto \mathcal{S}^\nu$ with $\nu \neq \mu$ and disregard renormalization terms. Consequently, the second term in Eq. 6.7 yields a damping

$$\partial_t \mathcal{S}^\mu_{\sigma\mathbf{q}} \big|_{\text{rad. damp.}} = -\frac{1}{\hbar}\gamma^\mu_{\mathbf{q}_\parallel} \mathcal{S}^\mu_{\sigma\mathbf{q}} \tag{6.8}$$

$$\gamma^\mu_{\mathbf{q}_\parallel} = \pi \sum_{\sigma\mathbf{k}} |\mathcal{M}^\mu_{\sigma\mathbf{k}}|^2 \delta_{\mathbf{k}_\parallel\mathbf{q}_\parallel} \delta(E^\mu_{\mathbf{q}_\parallel} - \hbar\omega_{\sigma\mathbf{k}}) \tag{6.9}$$

Moreover, we can perform the same calculation for the phonon-induced damping as demonstrated in Sec. 4.5, yielding $\partial_t \mathcal{S}^\mu_{\sigma\mathbf{q}} \big|_{\text{el-ph}} = -\frac{1}{\hbar}\Gamma^\mu_{\mathbf{q}_\parallel} \mathcal{S}^\mu_{\sigma\mathbf{q}}$. Finally, we solve the properly damped equation for $\mathcal{S}$ in the static limit ($\dot{\mathcal{S}} = 0$) and plug the result in Eq. 6.6, which yields the so called Elliot formula for the PL:

$$\partial_t n^{\mathrm{pt}}_{\sigma\mathbf{q}} = \frac{2}{\hbar}\sum_\mu \mathrm{Im}\{\frac{|\mathcal{M}^\mu_{\sigma\mathbf{q}}|^2 N^\mu_{\mathbf{q}_\parallel}}{E^\mu_{\mathbf{q}_\parallel} - \hbar\omega_{\sigma\mathbf{q}} - i(\gamma^\mu_{\mathbf{q}_\parallel} + \Gamma^\mu_{\mathbf{q}_\parallel})}\}. \tag{6.10}$$

Hence, for a perfectly perpendicular emission we find the intensity

$$I^\perp_\sigma(\omega) = \frac{2}{\hbar}\sum_\mu \gamma^\mu_\sigma N^\mu_{\mathbf{0}} \mathcal{L}_{\gamma^\mu + \Gamma^\mu}(E^\mu_{\mathbf{0}} - \hbar\omega), \tag{6.11}$$

where we used the Couchy/Lorentz distribution $\mathcal{L}_\gamma(E) = \gamma/(\pi(E^2+\gamma^2))$. Hence every bright exciton state $|\mu,\mathbf{Q}\approx 0\rangle$ emits with a Lorentzian spectral profile at its eigenenergy. Thereby the width is given by radiative and phonon-induced dephasing as already shown in the coherent limit (Sec. 4.5 and 4.6). However, in contrast to the linear spectroscopy, the emission intensity is now proportional to the number of excitons $N^\mu_{\mathbf{0}}$ occupying bright states (states within the light cone $\mathbf{Q}\approx 0$), where each exciton recombines with the rate $2\gamma^\mu_{\mathbf{0}}/\hbar$. Therefore, when comparing absorption and emission spectra, the peak intensities of PL peaks is re-scaled by the number of particles occupying the respective state. In Sec. 7.2 we show that electrons and holes excited above the band gap quickly dissipate their excess energy via emission of phonons until they reach the energetically lowest exciton states. This way a thermal equilibrium distribution $N^\mu_{\mathbf{Q}} \propto \exp(E^\mu_{\mathbf{Q}}/k_BT)$ is created on a picosecond timescale after optical excitation. The exciton recombination process is usually much slower than that, since only excitons in the light cone can decay into a photon (recombination bottleneck). Therefore, when calculating stationary luminescence it is a good approximation to assume a Boltzmann distribution for the exciton occupations.

In the above derivation we have only considered direct recombination of excitons [99, 100], which means that the CoM momentum of the exciton is fully transferred to the photon. This is because in the perturbative treatment of the exciton-phonon interaction we have neglected additional source terms and only included broadening contributions. In the following section we show how the above discussed model can be modified to include phonon-assisted recombination, i.e. the decay of excitons under simultaneous emission of photons and phonons.

6.3 Phonon-assisted Exciton Recombination

The fundamental law of momentum conservation only allows excitons with zero center-of-mass momentum to be created by or recombine through light emission. However, the vast majority of states in the excitonic band structure has a non-zero center of mass momentum. In particular, intervalley excitons have very large center of mass momenta $\mathbf{Q}_\zeta = \zeta^e - \zeta^h$ and in some materials are energetically far below the momentum direct bright exciton [95]. Therefore, after an optical excitation and ultrafast thermalization the majority of excitons will occupy the energetically lowest, dark intervalley excitons state. However the lifetime of these dark state is not infinite, but is limited by defect or phonon-assisted recombination processes. These recombination processes require the simultaneous dissipation of momentum, e.g. through emission of a phonon [101–104]. These three-particle processes are however very inefficient compared to the direct recombination of an exciton with zero center-of-mass momentum. Nonetheless, when the intervalley exciton lower in energy than the bright state, the low temperature PL can exhibit

strong phonon-assisted signals due to an orders of magnitude larger population of the dark state, as depicted in Fig. 6.1. These indirect recombination channels are

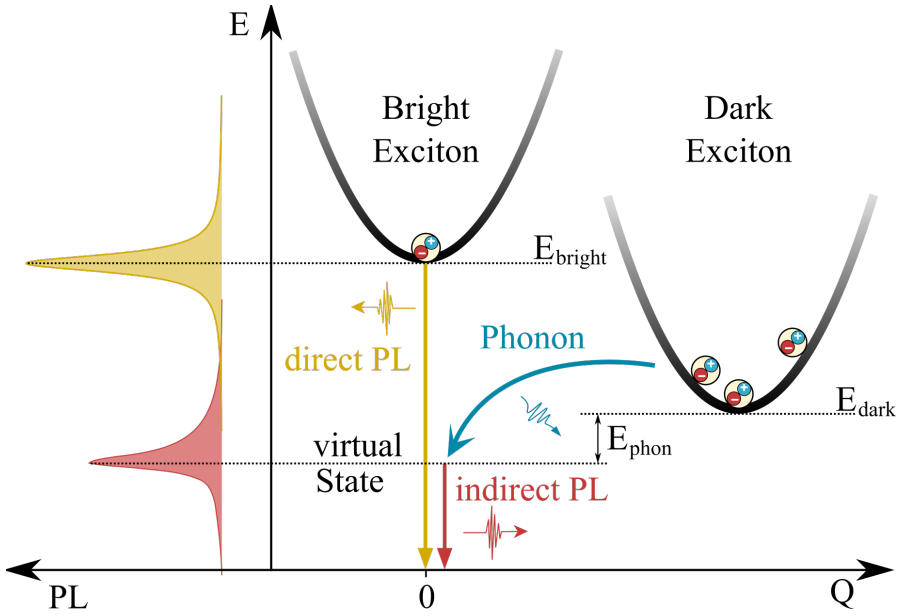

Figure 6.1: Luminescence from dark excitons. Sketch of direct and indirect decay channels showing the underlying scattering processes in the excitonic center-of-mass dispersion (right) and the corresponding PL signals (left). Momentum-dark excitons can decay by simultaneously interacting with phonons and photon, giving rise to phonon side peaks (red). Figure adopted from Paper 3.

usually visualized as two-step processes, in which the exciton first scatters into a virtual state in the light cone via interaction with a phonon and consequently recombines by emitting a photon with the energy of the virtual state $\mathrm{E_{dark}} \pm \mathrm{E_{phonon}}$. Such emission traces provide a unique possibility to measure the energetic position of otherwise optically inaccessible dark excitons.

In the following, we discuss how phonon-assisted recombination channels can be included in the microscopic luminescence model introduced in the last section. For clarity we drop the photon (σ) and phonon mode index (j). The calculation can be similarly performed for multiple photon/phonon modes and yields and additive solution. Just as in the last section we applying the Heisenberg equation of motion to calculate the evolution of the photon density by including H_0, $H_{\text{x-pt}}$ and $H_{\text{x-ph}}$. In contrast to the last section we thereby include additional source terms and higher-order exciton-phonon-photon correlations. Hence we find a closed system of equations for the photon density $n^{\text{pt}}_{\mathbf{k}} = \langle c^\dagger_{\mathbf{k}} c_{\mathbf{k}} \rangle$, the recombination amplitude $\mathcal{S}^{\mu}_{\mathbf{k}} = \langle c^\dagger_{\mathbf{k}} X_{\mu \mathbf{k}_\parallel} \rangle$, the phonon-assisted recombination amplitude $\mathcal{U}^{\mu,\pm}_{\mathbf{kq}} = \langle c^\dagger_{\mathbf{k}} b^{(\dagger)}_{\mp \mathbf{q}} X_{\mu \mathbf{k}_\parallel - \mathbf{q}} \rangle$

and the exciton-phonon correlation $\mathcal{C}^{\nu\mu,\pm}_{\mathbf{kq}} = \langle X^\dagger_{\nu\mathbf{k}_\parallel} X_{\mu\mathbf{k}_\parallel-\mathbf{q}} b^{(\dagger)}_{\mp\mathbf{q}}\rangle$:

$$\frac{d}{dt} n^{\mathrm{pt}}_{\mathbf{k}} = \frac{2}{\hbar}\sum_\mu \mathrm{Im}\{\mathcal{M}^\mu_{\mathbf{k}}\mathcal{S}^\mu_{\mathbf{k}}\}, \tag{6.12}$$

$$i\hbar\frac{d}{dt}\mathcal{S}^\mu_{\mathbf{k}} = (E^\mu_{\mathbf{k}_\parallel} - \hbar\omega_{\mathbf{k}})\mathcal{S}^\mu_{\mathbf{k}} - \mathcal{M}^{\mu*}_{\mathbf{k}} N^\mu_{\mathbf{k}_\parallel} + \sum_{\nu\mathbf{q}\pm}\mathcal{D}^{\nu\mu}_{\mathbf{q}}\mathcal{U}^{\nu\pm}_{\mathbf{kq}} + \dot{\mathcal{S}}|^{\mathrm{rad}}_{\mathrm{deph.}}, \tag{6.13}$$

$$\begin{aligned} i\hbar\frac{d}{dt}\mathcal{U}^{\nu,\pm}_{\mathbf{kq}} &= (E^\nu_{\mathbf{k}_\parallel-\mathbf{q}} \mp \hbar\Omega_{\mathbf{q}} - \hbar\omega_{\mathbf{k}})\mathcal{U}^{\nu,\pm}_{\mathbf{kq}} + \sum_\mu \mathcal{D}^{\nu\mu*}_{\mathbf{q}}\eta^\pm_{\mathbf{q}}\mathcal{S}^\mu_{\mathbf{k}} \\ &\quad - \sum_\mu \mathcal{M}^{\mu*}_{\mathbf{k}}\mathcal{C}^{\mu\nu,\pm}_{\mathbf{kq}} + \dot{\mathcal{U}}|^{\mathrm{ph}}_{\mathrm{deph.}}, \end{aligned} \tag{6.14}$$

$$i\hbar\frac{d}{dt}\mathcal{C}^{\nu\mu,\pm}_{\mathbf{kq}} = (E^\mu_{\mathbf{k}_\parallel-\mathbf{q}} - E^\nu_{\mathbf{k}_\parallel} \mp \hbar\Omega_{\mathbf{q}})\mathcal{C}^{\nu\mu,\pm}_{\mathbf{kq}} - \mathcal{D}^{\mu\nu*}_{\mathbf{q}} Q^{\nu\mu,\pm}_{\mathbf{kq}} + \dot{\mathcal{C}}|^{\mathrm{rad+ph}}_{\mathrm{deph.}}, \tag{6.15}$$

where $\eta^\pm_{\mathbf{q}} = 1/2 \mp 1/2 + \langle b^\dagger_{\mathbf{q}} b_{\mathbf{q}}\rangle$ denotes the phonon occupation factors for absorption (+) and emission (-), $N^\mu_{\mathbf{Q}} = \langle X^\dagger_{\mu\mathbf{Q}} X_{\mu\mathbf{Q}}\rangle$ is the exciton density and $Q^{\nu\mu,\pm}_{\mathbf{kq}} = \eta^\mp_{\mathbf{q}} N^\mu_{\mathbf{k}_\parallel-\mathbf{q}} - \eta^\pm_{\mathbf{q}} N^\nu_{\mathbf{k}_\parallel}$ abbreviates the source term of exciton-phonon correlations.

To arrive at this set of equations we have applied the cluster expansion scheme and again neglected all coherent quantities. Moreover, we assume the low density limit and therefore neglect quadratic occupations and disregard contributions connected to multi-phonon processes. Finally, we have abbreviated additional correlations giving rise to a dephasing of the respective quantity with $(\cdot)|^{\mathrm{phon}}_{\mathrm{deph.}}$. It is important to note that these dephasing contributions need to be treated on the same microscopic footing as the dephasing resulting from the coupling between $\mathcal{S}$ and $\mathcal{U}$. An inconsistent damping of the equations, e.g. by approximating all dephasing contributions with a damping constant δ can lead to non-physical solutions such as negative PL signals.

In the supplementary material of Paper 3 we show how the above system of equations can be simplified in order to obtain an analytical formula for the static PL signal, including a self consistent many-particle dephasing. Here we are only going to briefly discuss the general structure and interpretation of the final equation. For a thermalized exciton distribution, we find the following analytic expression for the σ-polarized photon flux emitted in perpendicular direction with respect to the monolayer:

$$\begin{aligned} I^\perp_\sigma(\omega) = \frac{2}{\pi\hbar}\sum_\mu \frac{\gamma^\mu_\sigma}{(E^\mu_{\mathbf{0}} - \hbar\omega)^2 + (\gamma^\mu_{\mathbf{0}} + \Gamma^\mu_{\mathbf{0}})^2}\Bigg(\gamma^\mu_{\mathbf{0}} N^\mu_{\mathbf{0}} \\ + \sum_{\nu\mathbf{q},j\pm} |\mathcal{D}^{\mu\nu}_{j\mathbf{q}}|^2 N^\nu_{\mathbf{q}}\eta^\pm_{j\mathbf{q}} \frac{\Gamma^\nu_{\mathbf{q}}}{(E^\nu_{\mathbf{q}} \pm \hbar\Omega_{j\mathbf{q}} - \hbar\omega)^2 + (\Gamma^\nu_{\mathbf{q}})^2}\Bigg). \end{aligned} \tag{6.16}$$

The first line is analogous to the result for the direct recombination derived in the last section, with the important difference that the phonon dephasing Γ^μ here only appears in the denominator. However, for energies $\hbar\omega \approx E_0^\mu$ the second line containing the scattering contributions can be rewritten as phonon-guided in-scattering to the bright state. In thermal equilibrium this is approximately equal to the out-scattering, cf. Sec. 7.1, so that the second term becomes $\Gamma_{\mathbf{0}}^\mu N_{\mathbf{0}}^\mu$. Hence, in the resonant case, Eq. 6.16 can be well approximated with the Elliot formula derived in the last section,

$$I_\sigma^\perp(\omega)|_{\omega\approx E_0^\mu} = \frac{2}{\pi\hbar}\frac{\gamma_\sigma^\mu(\gamma_{\mathbf{0}}^\mu+\Gamma_{\mathbf{0}}^\mu)}{(E_{\mathbf{0}}^\mu-\hbar\omega)^2+(\gamma_{\mathbf{0}}^\mu+\Gamma_{\mathbf{0}}^\mu)^2}N_{\mathbf{0}}^\mu. \tag{6.17}$$

It is important to note that the two contributions in Eq. 6.16 should not be interpreted as direct and phonon assisted recombination, since the second contribution also accounts for the dephasing of the direct recombination.

The scattering contribution in Eq. 6.16 is for large detuning from the bright state $\propto |\mathcal{MD}|^2/(E_0-\hbar\omega)^2$ and therefore agrees well with expressions obtained from other perturbative treatments, e.g. as derived for optical phonon replicas in the polaron picture in Refs. [101, 102]. The advantage of the cluster expansion is that it consistently includes phonon-induced broadening as well as additional phonon-assisted decay channels. This allows us to quantitatively compare line shapes and intensities of bright and dark exciton states in experiment and theory.

The luminescence formula is one of the key outcomes of this work and can be applied to an arbitrary semiconductor whose band edge excitations are of excitonic nature. In the following section, we apply the formula to calculate the low temperature PL spectrum of WSe_2 revealing optical signatures of dark intervalley excitons.

6.4 Dark Exciton Luminescence in WSe_2 Monolayers

TMD monolayers have over the last years remained in the focus of fundamental condensed matter research, partly because the strong many-particle interactions in these systems provide an excellent platform to study intriguing quantum phenomena of correlated systems. One of the major puzzles of the TMD research has been the low-temperature PL spectrum. While the PL of TMDs on SiO_2 is dominated by bright exciton peak, potentially a trion peak and some random defect peaks far below the A exciton, hBN encapsulated samples have revealed a plethora of new peaks below the apparent exciton ground states resonance [105–108], whose microscopic origin has been mostly unknown. Most studies on this topic have

focused on the impact of bound exciton configurations, such as trions [109], biexcitons [110] and trapped excitons [111, 112]. In Paper 3 we have demonstrated in a joint experiment-theory study that some of the low-temperature emission peaks in WSe_2 are likely related to the phonon-assisted recombination of momentum-dark K-K' excitons. In Paper 3 we present the bright and dark exciton energies calculated with the Wannier equation and ab initio band parameters. Moreover, we evaluate Eq. 6.16 for hBN encapsulated WSe_2 for different temperatures and demonstrate how the shape of phonon-sidebands evolves. Here, we only point out the main outcome of this work. In Fig. 6.2 we compare a PL spectrum measured

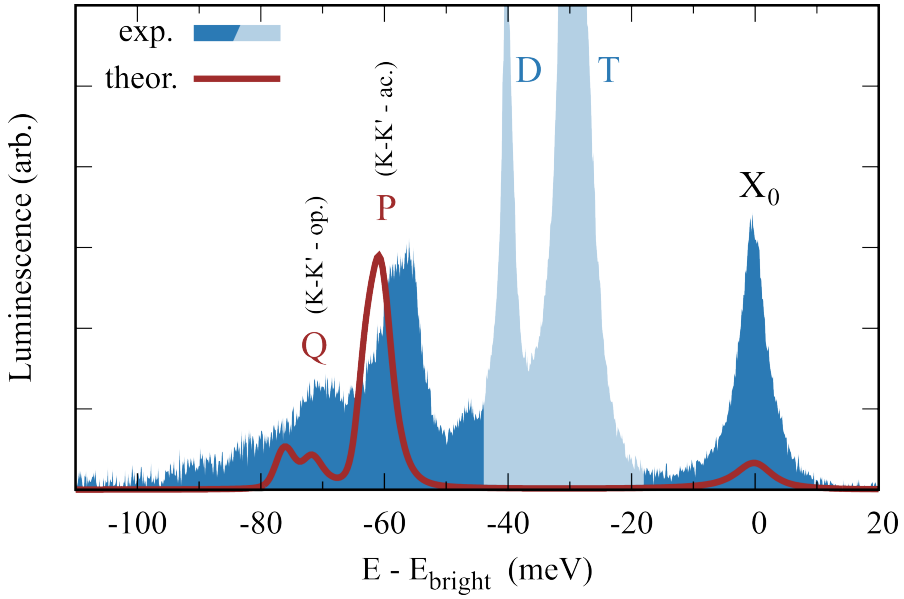

Figure 6.2: PL spectra in experiment and theory. The blue curve shows the PL measured on hBN-encapsulated WSe_2 at the charge neutrality point and T=15 K. The red curve shows the simulated spectrum. The peaks P and Q denote the acoustic and optical phonon-assisted recombination of K-K' excitons. Figure adopted from Paper 3.

by the Urbaszek Group from the University in Toulouse (CNRS) with our model. The blue curve shows the measured PL at T=15 K for hBN-encapsulated WSe_2 at the charge neutrality point (applied gate voltage) [106]. The red curve shows the calculated spectrum for an equivalent set of parameters.

Both experiment and theory show additional resonances between 50 and 80 meV below the bright exciton denoted with P and Q. The two other peaks around 40 and 30 meV below the A exciton peak (denoted with D and T) have been assigned to spin-forbidden dark states [107] and charge defect bound trions [113], respectively. In contrast, the microscopic origin of the peaks P and Q has been unknown. Our model and several other independent studies [105, 114, 115] suggest that they result from a phonon-assisted recombination of momentum-dark K-K' excitons.

While the agreement of peak positions in experiment and theory are reasonably good, there are significant differences in the height of the bright exciton X_0 and the phonon side peaks P,Q. This deviation may stem from inaccuracies in the exciton-phonon matrix element, e.g. resulting from the applied deformation potential approximation in Ref. [71], whose parameters have been used in this work. Moreover, the calculated PL signal uses a Boltzmann distribution to approximate the exciton occupations, which might be insufficient in the considered low temperature regime and CW excitation. In general, the complex interplay of optical pumping, relaxation of excitons and recombination might result in quasi-equilibrium occupations that deviate from the assumed Boltzmann distribution. However, in the supplementary material of Paper 3 we show spectra measured at other temperatures and find a good agreement for the temperature trends for peak shapes and intensity ratios. Moreover, in a follow-up joint experiment-theory project (Paper 28), we have investigated how the phonon-sidebands evolve in time. Here we combined a full simulation of the exciton relaxation dynamics (Sec. 7) with time- and spectrally resolved PL measurements. In good agreement between experiment and theory, we were able to show that the phonon-driven thermalization of the optically injected excitons is resulting in a temporal red-shift of the phonon assisted PL peaks.

CHAPTER 7

EXCITON DYNAMICS

So far we have only considered static exciton properties, such as the linear coherent response of TMDs (Sec. 4) and the luminescence signal stemming from the recombination of an incoherent quasi-equilibrium exciton distribution (Sec. 6). In the following we will investigate how incoherent exciton populations are formed and distributed in energy after the material has been excited with a short optical pump pulse. In particular, we will show how electron-hole pairs created with energies far above the excitonic ground state dissipate their excess energy via the emission of phonons. In the last part of this section, we also demonstrated how the exciton relaxation processes can be indirectly observed in ultrafast pump-probe experiments.

7.1 Formation of Incoherent Excitons

In Sec. 6 we have assumed that the excitation of light and a subsequent thermalization process leads to an occupation of exciton energies $N^{\mu}_{\mathbf{Q}} = \langle X^{\dagger}_{\mu\mathbf{Q}} X_{\mu\mathbf{Q}} \rangle$. In the following we will derive the equations of motion, which describe the formation of these exciton populations [37, 55, 80, 116]. To this end, we derive the different contributions to the exciton dynamics resulting from exciton-phonon interaction, excitation with coherent light and recombination due to the coupling of to the quantized photon field. Thereby, mixed contributions such as the exciton-phonon-photon interaction discussed in Sec. 6 will be neglected and the exciton-phonon as well as exciton-photon scattering are treated perturbatively on the level of the second-order Born-Markov approximation.

Exciton-Phonon Scattering

To derive the phonon-contribution to the equations of motion, we set up the Heisenberg equation of motion for the exciton occupation $N^{\mu}_{\mathbf{Q}}$ including H_0 and $H_{\text{x-ph}}$. Similar to the procedure described in Sec. 4.5 we truncate the many-particle hierarchy on the level of two-particle correlations yielding the coupled equations,

$$\partial_t N^{\mu}_{\mathbf{Q}} \big|_{\text{x-ph}} = \frac{2}{\hbar} \sum_{\nu \mathbf{Q}, \pm} \text{Im}\{\mathcal{D}^{\nu\mu}_{\mathbf{q}} \mathcal{C}^{\mu\nu\pm}_{\mathbf{Q}\mathbf{q}}\}, \tag{7.1}$$

$$\begin{aligned} i\hbar \partial_t \mathcal{C}^{\mu\nu,\pm}_{\mathbf{Q}\mathbf{q}} \big|_{\text{x-ph}} &= (E^{\nu}_{\mathbf{Q}-\mathbf{q}} - E^{\mu}_{\mathbf{Q}} \mp \hbar\Omega_{\mathbf{q}}) \mathcal{C}^{\mu\nu,\pm}_{\mathbf{Q}\mathbf{q}} \\ &\quad - \mathcal{D}^{\nu\mu *}_{\mathbf{q}} (\eta^{\mp}_{\mathbf{q}} N^{\nu}_{\mathbf{Q}-\mathbf{q}} - \eta^{\pm}_{\mathbf{q}} N^{\mu}_{\mathbf{Q}}), \end{aligned} \tag{7.2}$$

with the definitions introduced in the last section, $\mathcal{C}^{\mu\nu,\pm}_{\mathbf{Q}\mathbf{q}} = \langle X^{\dagger}_{\mu\mathbf{Q}} X_{\nu\mathbf{Q}-\mathbf{q}} b^{\dagger/(\ )}_{\mp\mathbf{q}} \rangle$ and $\eta^{\pm}_{\mathbf{q}} = 1/2 \mp 1/2 + \langle b^{\dagger}_{\mathbf{q}} b_{\mathbf{q}} \rangle$. It is important to note that we have neglected non-linear terms ($\propto N^2$) to obtain the above equation for $\mathcal{C}$. These terms result from the bosonic commutator relations used for the exciton operators. This commutator, however, only holds for low densities ($N_{\mathbf{Q}} << 1$) in which the linear terms ($\propto N$) dominate. At higher densities, where the N^2 terms might become important, we would also need to include correction terms to the bosonic exciton commutator to be consistent. A numerical evaluation of the above system of equations is due to the large dimensionality of $\mathcal{C}$ extremely expensive and the solution would also depend on the unknown damping of the latter. However, a physically intuitive and numerically feasible description of the system is obtained by solving Eq. 7.2 within a Markov/adiabatic approximation, yielding

$$\mathcal{C}^{\mu\nu,\pm}_{\mathbf{Q}\mathbf{q}} \approx i\pi \mathcal{D}^{\nu\mu *}_{\mathbf{q}} (\eta^{\mp}_{\mathbf{q}} N^{\nu}_{\mathbf{Q}-\mathbf{q}} - \eta^{\pm}_{\mathbf{q}} N^{\mu}_{\mathbf{Q}}) \delta(E^{\nu}_{\mathbf{Q}-\mathbf{q}} - E^{\mu}_{\mathbf{Q}} \mp \hbar\Omega_{\mathbf{q}}), \tag{7.3}$$

which plugged into the equation for the densities gives rise to a Boltzmann scattering equation,

$$\partial_t N^{\mu}_{\mathbf{Q}} \big|_{\text{x-ph}} = \sum_{\nu \mathbf{Q}'} (W^{\nu\mu}_{\mathbf{Q}'\mathbf{Q}} N^{\nu}_{\mathbf{Q}'} - W^{\mu\nu}_{\mathbf{Q}\mathbf{Q}'} N^{\mu}_{\mathbf{Q}}) \tag{7.4}$$

$$W^{\mu\nu}_{\mathbf{Q}\mathbf{Q}'} = \frac{2\pi}{\hbar} \sum_{\pm, j} |\mathcal{D}^{\mu\nu}_{j,\mathbf{Q}'-\mathbf{Q}}|^2 (\frac{1}{2} \pm \frac{1}{2} + n^{\text{ph}}_{j,\mathbf{Q}'-\mathbf{Q}}) \delta(E^{\nu}_{\mathbf{Q}'} - E^{\mu}_{\mathbf{Q}} \pm \hbar\Omega_{\mathbf{q}}). \tag{7.5}$$

Here the coefficients $W^{\mu\nu}_{\mathbf{Q}\mathbf{Q}'}$ denote the probability rates to scatter from state $|\mu\mathbf{Q}\rangle$ to state $|\nu\mathbf{Q}'\rangle$, which resemble Fermis golden rule with different weights for phonon emission (+) and absorption processes (-) given by the relevant phonon numbers. Consequently, the first term in Eq. 7.4 corresponds to the total in-scattering, while the second term reflects the out-scattering from the respective state. The latter is closely related to the dephasing rate Γ (inverse coherence lifetime) derived in Sec. 4.5 via $2\Gamma^{\mu}_{\mathbf{Q}}/\hbar = W^{\text{out}}_{\mu\mathbf{Q}} = \sum_{\nu\mathbf{Q}'} W^{\mu\nu}_{\mathbf{Q}\mathbf{Q}'}$.

Spontaneous Recombination

With the same procedure we now consider the coupling of exciton occupations to the photon field described by $H_{\text{x-pt}}$. Thus we obtain

$$\partial_t N^{\mu}_{\mathbf{Q}} \big|_{\text{x-pt}} = -\frac{2}{\hbar} \sum_{\sigma \mathbf{q}} \text{Im}\{\tilde{\mathcal{M}}^{\mu}_{\sigma \mathbf{q}} \mathcal{S}^{\mu}_{\sigma \mathbf{q}}\} \delta_{\mathbf{q}_{\parallel}, \mathbf{Q}_{\parallel}} \tag{7.6}$$

$$i\hbar \frac{d}{dt} \mathcal{S}^{\mu}_{\mathbf{q}} \big|_{\text{x-pt}} = (E^{\mu}_{\mathbf{q}_{\parallel}} - \hbar\omega_{\mathbf{q}}) \mathcal{S}^{\mu}_{\mathbf{q}} - \mathcal{M}^{\mu *}_{\mathbf{k}} N^{\mu}_{\mathbf{q}_{\parallel}}, \tag{7.7}$$

where we have neglected the number of photons and suppressed dephasing contributions in Eq. 7.7. We again apply the Markov approximation in Eq. 7.7 and plug the result in the equation of the density, yielding

$$\partial_t N^{\mu}_{\mathbf{Q}} \big|_{\text{x-pt}} = -\frac{2}{\hbar} \gamma^{\mu}_{\mathbf{Q}} N^{\mu}_{\mathbf{Q}} \approx -\frac{2}{\hbar} \tilde{\gamma}^{\mu} N^{\mu}_{\mathbf{Q}} \delta_{\mathbf{Q},0}, \tag{7.8}$$

where we have identified the radiative dephasing γ (Eq. 6.9) and introduced an effective recombination rate $\tilde{\gamma}$, which is an integral over the recombination rates throughout the lightcone. The second form of Eq. 7.8 ($\propto \delta_{\mathbf{Q},0)}$) underlines that $\gamma_{\mathbf{Q}}$ is strongly peaked around $\mathbf{Q} = 0$, since the recombination requires momentum conservation. As a result of the negligible momentum of photons in the visible spectral range, only excitons with almost vanishing CoM momentum can recombine and emit photons. Moreover, we again find that the occupation N decays with twice the decay constant of the polarization P, which is consistent with the singlet factorization $N = |P|^2 + \delta N$.

Coherent Excitation

In the above consideration of the coupling between excitons and the electromagnetic field, we have neglected the absorption and stimulated emission of photons, which consequently only describes the coupling to the photon vacuum. Hence, Eq. 7.8 only captures the change of exciton numbers due to spontaneous recombination. To include an excitation of the system with a short laser pulse, we simply split the electromagnetic field into a part describing the laser pulse and the "rest". Since the excitation pulse is usually coherent laser light, this part is well described by the semi-classical exciton light coupling $H_{\text{x-l}}$. The coupling to the "rest" field is then described fully quantum mechanically through the treatment in the last section. At this point it is also worth noting that for the exciton occupation $N^{\mu}_{\mathbf{Q}} = \langle X^{\dagger}_{\mu \mathbf{Q}} X_{\mu \mathbf{Q}} \rangle$ we have so far not distinguished between coherent and incoherent contributions. Therefore, one part of the dynamics of $N^{\mu}_{\mathbf{Q}}$ is reflecting the evolution of coherent excitonic polarizations $P^{\mu}_{\mathbf{Q}}$ (Sec. 4) and therefore we also obtain a direct coupling to the laser field,

$$\partial_t N^{\mu}_{\mathbf{Q}} \big|_{\text{x-l}} = \frac{2}{\hbar} \text{Im}\{\frac{e_0}{m_0} \boldsymbol{\mathcal{M}}^{\mu *} \cdot \mathbf{A}(t) P^{\mu}_{\mathbf{Q}}\} \delta_{\mathbf{Q},0}. \tag{7.9}$$

In the following we will show that this is just the excitation of coherent excitons $P^\mu_{\mathbf{Q}}$, while the creation of genuinely incoherent excitons needs an additional scattering process with phonons.

Polarization-to-Population Transfer

For the discussion of microscopic phenomena and the interpretation of optical experiments it is often useful to distinguish between the coherent exciton polarization $P^\mu_{\mathbf{Q}} = \langle X^\dagger_{\mu\mathbf{Q}} \rangle$ and genuinely incoherent excitons, given by the correlated part of the exciton number $\delta N^\mu_{\mathbf{Q}} = \langle X^\dagger_{\mu\mathbf{Q}} X_{\mu\mathbf{Q}} \rangle - \langle X^\dagger_{\mu\mathbf{Q}} \rangle \langle X_{\mu\mathbf{Q}} \rangle = N^\mu_{\mathbf{Q}} - |P^\mu_{\mathbf{Q}}|^2$. Thereby the dynamics of the coherent part has been derived in Sec. 4 and in total reads

$$i\hbar \partial_t P^\mu = -(E^\mu_{\mathbf{0}} + i\gamma^\mu_{\mathbf{0}} + i\Gamma^\mu_{\mathbf{0}}) P^\mu - \frac{e_0}{m_0} \boldsymbol{\mathcal{M}}^\mu \cdot \mathbf{A}(t). \tag{7.10}$$

Since we do not consider any coherent processes creating excitonic polarizations with $\mathbf{Q} \neq 0$, we have redefined $P^\mu \equiv \langle X^\dagger_{\mu\mathbf{0}} \rangle$. The incoherent dynamics is now given by

$$\delta \dot{N}^\mu_{\mathbf{Q}} = \partial_t (N^\mu_{\mathbf{Q}} - |P^\mu_{\mathbf{Q}}|^2) = \dot{N}^\mu_{\mathbf{Q}} - 2\mathrm{Re}\{\dot{P}^\mu P^{\mu *}\} \delta_{\mathbf{Q},0}, \tag{7.11}$$

which yields the equation of motion for incoherent exciton densities,

$$\delta \dot{N}^\mu_{\mathbf{Q}} = \sum_\nu W^{\nu\mu}_{\mathbf{0Q}} |P^\nu|^2 + \sum_{\nu\mathbf{Q}'} (W^{\nu\mu}_{\mathbf{Q}'\mathbf{Q}} \delta N^\nu_{\mathbf{Q}'} - W^{\mu\nu}_{\mathbf{QQ}'} \delta N^\mu_{\mathbf{Q}}) - \frac{2}{\hbar} \gamma^\mu_{\mathbf{Q}} \delta N^\mu_{\mathbf{Q}}. \tag{7.12}$$

The above equations 7.10 and 7.12 contain all intrinsic processes shaping the life cycle of an exciton. The coherent laser light creates excitonic polarizations described by the driving term in Eq. 7.10. Subsequently, the polarization is coherently re-emitted (γ^μ_0) corresponding to Rayleigh scattered light or, more importantly, decays through interaction with phonons quantified by the phonon-dephasing Γ^μ_0. However, the energy of the coherent exciton is not lost, but it is converted into incoherent exciton occupations, which is reflected by the first term in Eq. 7.12. One can see that the decay of the coherent excitons is driving incoherent populations by considering the total changes due to interaction with phonons

$$\sum_{\mu\mathbf{Q}} \partial_t \delta N^\mu_{\mathbf{Q}} \big|_{\text{x-ph}} = \sum_{\nu\mu\mathbf{Q}} W^{\nu\mu}_{\mathbf{0Q}} |P^\nu|^2 = \frac{2}{\hbar} \sum_\mu \Gamma^\mu_{\mathbf{0}} |P^\mu|^2 = -\sum_\mu \partial_t |P^\mu|^2 \big|_{\text{x-ph}}. \tag{7.13}$$

This transfer from coherent to incoherent excitons due to scattering with phonons is referred to as polarization-to-population transfer [37, 59, 80].

After incoherent excitons have been created, they redistribute across all available exciton states via scattering with phonons, which is described by the Boltzmann scattering term (second part of Eq. 7.12). Finally, excitons with zero CoM can spontaneously recombine again and emit incoherent photons.

It is important to note that the compound exciton index μ contains the exciton valley, but also the main quantum number n_μ and angular momentum l_μ determining the relative motion of electron and hole, which was discussed in Sec. 4.4. Hence, excitons not only gain or loose CoM momentum via interaction with phonons, but can also dissipate energy of their internal motion, e.g. by performing a phonon-assisted transition from a 2p to the 1s state. Moreover, the solutions of the Wannier equation (indexed by μ) not only contain bound electron-hole pairs ($E^b_\mu < 0$), but also a continuum of free scattering states ($E^b_\mu > 0$) which resemble the free electron and hole plasma states with pair energies above the band gap. Hence, Eqs. 7.10 and 7.12 do not only capture the single particle kinetics of the ground state exciton, which has been studied in previous works [59, 80], but also contains the formation of bound excitons out of a free electron-hole plasma after excitation above the band gap. The numerical simulation of this exciton relaxation across the full Rydberg series of excited exciton states is a key outcome of this thesis and is discussed in the next section.

7.2 Exciton Relaxation Cascade in $MoSe_2$

In the following we consider the exciton relaxation dynamics in $MoSe_2$ monolayers after an optical excitation with energies at the single particle band gap. In Paper 1 we provide a detailed analysis of the time-, momentum- and energy resolved dynamics of the system. Here we just give a short overview of the principle mechanism and the key outcomes. Figure 7.1 schematically illustrates the exciton band structure and the dominant relaxation mechanisms after an excitation close to the band edge. The pump pulse creates quasi-free electron-hole pairs at the scattering continuum (yellow arrow), which subsequently dissipate their excess energy via a sequence of phonon emissions [116], performing a cascadic relaxation across the Rydberg-series of lower lying exciton states (orange arrows), in particular also scattering to momentum indirect pairs, such as KΛ excitons.

Fig. 7.2, shows the simulated exciton dynamics after an excitation 20 meV below the free-particle band gap and parameters for $MoSe_2$ on a SiO_2 substrate. The time interval at which the pump pulse passes the sample is yellow shaded. The coloured areas under the black curve (total number of electron-hole pairs) illustrate the fractions of appearing exciton states, e.g. at 0.5 ps, shortly after the pump

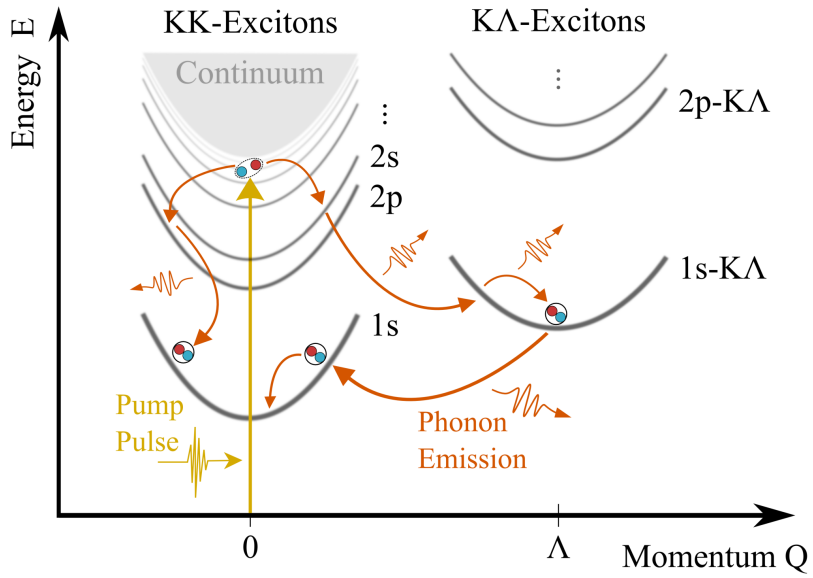

Figure 7.1: Intraexcitonic relaxation cascade in $MoSe_2$. Excited hot electron-hole pairs dissipate energy via a sequence of phonon emissions, performing a cascade-like relaxation through the Rydberg series of exciton states including momentum indirect KΛ states. Figure adopted from Paper 1.

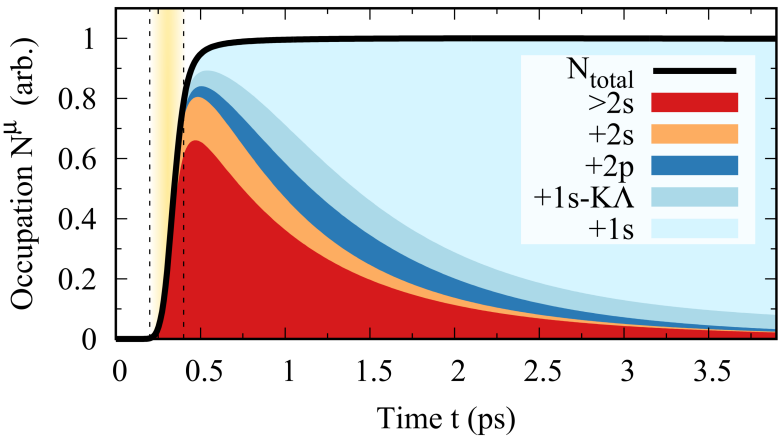

Figure 7.2: Exciton formation and relaxation dynamics. Evolution of the momentum integrated exciton occupations N. The black line shows the overall number of incoherent excitons, while the coloured surfaces below the black line represent the relative fraction of the respective exciton state. After 1.5 ps a 1/e-fraction of the excited pairs has relaxed into the 1s-ground state. Figure adopted from Paper 1.

pulse more than 60% of the occupation are in states higher than 2s, while at 4 ps, ore than 90% of the occupation have relaxed to the 1s ground state. Note that the different contributions were added up successively to pile up to the total

number. Moreover, the large amount of different excited states close to the band gap ($E > E_{2s}$) have been grouped for a better overview.

Fig. 7.2 shows that optically excited, "hot" pairs dissipate their energy and decay into lower lying states on a ps-timescale. Our simulation predicts that after 1.5 ps a 1/e-fraction of the excited pairs has decayed into the 1s-ground state revealing an ultrafast formation of bound excitons out of a free electron-hole plasma. In Paper 1 we discuss the most efficient relaxation channels determined by the symmetries of exciton wave functions and the arrangement of energy levels. Moreover, we also show snap shots of the momentum resolved exciton dynamics across the Rydberg series of bright and dark exciton states.

7.3 Pump-Probe Spectroscopy via Intraexcitonic Transitions

In contrast to linear absorption experiments, addressing the static properties of the system, the so called pump-probe spectroscopy allows us to study the dynamics of excited charge carriers and – similarly intriguing – the internal degrees of freedom of excited quasi-particles. The most frequently used pump-probe method uses two pulses addressing interband transitions. While the first pump pulse is strongly absorbed by the material, giving rise to excited charge carriers in the conduction band, the second probe pulse becomes less absorbed by the material, which results from the Pauli blocking of the already excited carriers (Paper 25). Therefore, the change in the absorption of the probe pulse as function of delay between pump and probe provides information of the carrier relaxation process on ultrafast timescales. However, in this thesis we focus on a slightly different approach to pump-probe spectroscopy, where the probe pulse addresses low frequency intraband transitions. The idea behind this technique is that the presence of excitons created by the first pump pulse can significantly modify the low frequency response of the material, which subsequently can be probed by the absorption of a the probe pulse [117–120]. The reason for the change in the response function is that the optically injected excitons can interact with light by performing transitions between internal degrees of freedom, e.g. from their ground state (1s) to the first excited state (2p). For TMD monolayers, this change in the relative motion of the electron-hole pair can occur via the absorption of terahertz/far infra-red light [21, 121, 122]. From a theoretical point of view, the intraexcitonic response results from oscillating intraband currents induced by the electrical field of the probing laser. To derive the response function we consider the intraband contribution to the probability current (Eq. 4.4), which reads

$$\langle \hat{\mathbf{j}} \rangle(t) \,|_{\,\text{intra}} = \frac{1}{A} \sum_{\zeta\lambda\mathbf{k}} \mathbf{j}^{\lambda}_{\zeta\mathbf{k}} \langle a^{\dagger}_{\lambda\zeta,\mathbf{k}} a_{\lambda\zeta,\mathbf{k}} \rangle = \frac{1}{A} \sum_{\nu\mu\mathbf{Q}} \boldsymbol{\mathcal{J}}^{\nu\mu}_{\mathbf{Q}} \langle X^{\dagger}_{\mu\mathbf{Q}} X_{\nu\mathbf{Q}} \rangle, \tag{7.14}$$

where in the second step we have expanded the electronic operators in terms of excitons via Eq. 5.10 and 5.11, where the exciton index also contains valley quantum numbers. It is important to note that the exciton current matrix element vanishes for a bound state and $\nu = \mu$, since it is proportional to the expectation value of the relative momentum between electron and hole (cf. Eq. 5.23). Therefore, only transition correlations $\sigma^{\mu\nu}_{\mathbf{Q}} = \langle X^{\dagger}_{\mu\mathbf{Q}} X_{\nu\mathbf{Q}} \rangle$ between states with opposite parities, such as 1s and 2p, can contribute to a current. Similar to the treatment of the semiconductor Bloch equations in Sec. 4, we can now derive the linear response from the equations of motion of $\sigma^{\nu\mu}_{\mathbf{Q}}$. Here the source term results from the intraband contribution of the exciton-light coupling (Eq. 5.22) yielding,

$$i\hbar\partial_t \sigma^{\mu\nu}_{\mathbf{Q}} \big|_{\text{x-intra}} = \sum_{\xi} \mathbf{A}(\boldsymbol{\mathcal{J}}^{\xi\nu}_{\mathbf{Q}} \sigma^{\mu\xi}_{\mathbf{Q}} - \boldsymbol{\mathcal{J}}^{\mu\xi}_{\mathbf{Q}} \sigma^{\xi\nu}_{\mathbf{Q}}) \tag{7.15}$$

$$\approx \mathbf{A}\boldsymbol{\mathcal{J}}^{\mu\nu}_{\mathbf{Q}}(N^{\mu}_{\mathbf{Q}} - N^{\nu}_{\mathbf{Q}}), \tag{7.16}$$

where in the second step we only considered the coupling to densities (linear response), i.e. $\xi = \mu,\nu$. Analogue to the equation of motion for exciton densities $N^{\mu}_{\mathbf{Q}}$, we can also derive the phonon contribution to the equation of motion of $\sigma^{\nu\mu}_{\mathbf{Q}}$. Neglecting off-diagonal couplings $\dot{\sigma}^{\nu\mu} \propto \dot{\sigma}^{nm}$ with $n \neq \nu$ and $m \neq \mu$ (random phase approximation) we find the phonon dephasing

$$\dot{\sigma}^{\mu\nu}_{\mathbf{Q}} \big|_{\text{x-ph}} = -\frac{1}{\hbar}(\Gamma^{\mu}_{\mathbf{Q}} + \Gamma^{\nu}_{\mathbf{Q}})\sigma^{\mu\nu}_{\mathbf{Q}}. \tag{7.17}$$

Now we solve the equation of motion for σ in the frequency domain and plug the result into Eq. 7.14. Together with the defintion of the susceptibility Eq. 4.2 we thus obtain [118],

$$\chi_{\sigma}(\omega) = \frac{1}{\epsilon_0 A \omega^2} \sum_{\nu\mu\mathbf{Q}} |\boldsymbol{\mathcal{J}}^{\nu\mu}_{\mathbf{Q}} \cdot \mathbf{e}_{\sigma}|^2 \frac{N^{\nu}_{\mathbf{Q}} - N^{\mu}_{\mathbf{Q}}}{\hbar\omega - E^{\mu}_{\mathbf{Q}} + E^{\nu}_{\mathbf{Q}} - i(\Gamma^{\mu}_{\mathbf{Q}} + \Gamma^{\nu}_{\mathbf{Q}})}. \tag{7.18}$$

Again we find a sum of Lorentzian responses, however here at energies corresponding to intraexciton transitions. Moreover, in contrast to the linear absorption, the intraexcitonic response is proportional to the exciton number, since a certain transition from ν to μ can only be performed if an exciton occupies the initial states ν. Therefore, the interband pump - intraband probe spectroscopy has two unique capabilities. On one hand we obtain direct access to the internal transition energies, which provide information about the excitonic binding energies. On the other hand, we can resolve the occupation dynamics of incoherent excitons across different exciton states on an ultrafast timescale, while other techniques relying on absorption bleaching are only sensitive to the Pauli blocking of the excited

electron states (Paper 25), which do not contain information about electron-hole correlations. In contrast, THz/infrared spectroscopy addresses internal oscillations between electron hole pairs and is therefore sensitive to condensation phases of the electron-hole gas.

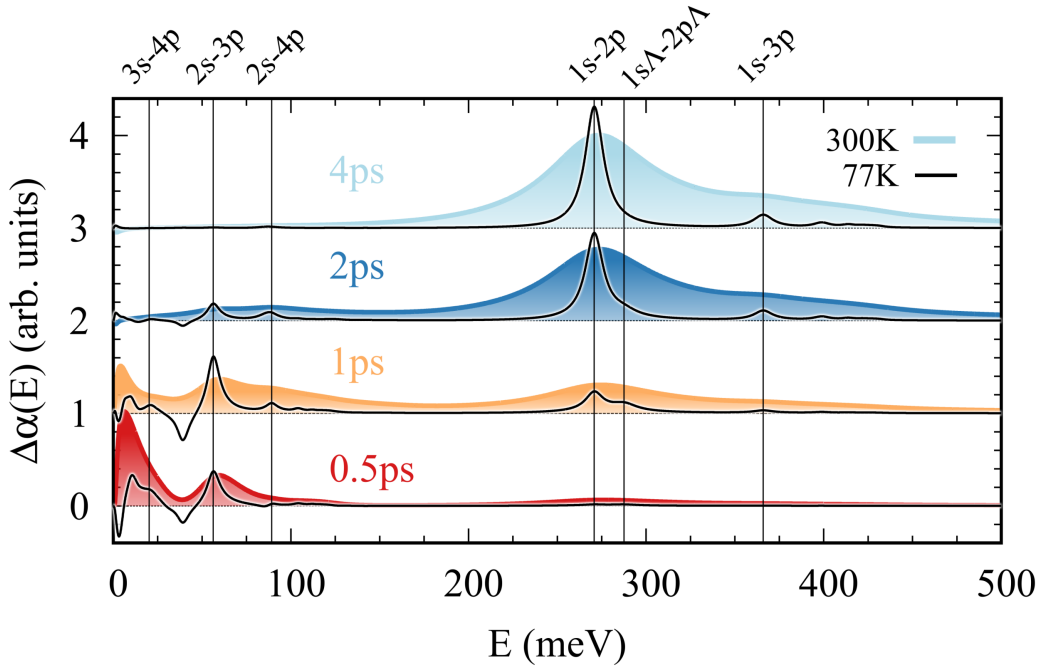

Figure 7.3: Pump-induced low frequency absorption as function of the probe energy for four different times. Shortly after the pump the occupation of excited states leads to multiple absorption features for energies below 150 meV, inter alia optical gain resulting from transient population inversions. For large delay times the spectrum is dominated by the response of the 1s-2p transitions of excitons in the ground state. Figure adopted from Paper 1.

Figure 7.3 shows the calculated low frequency absorption ($\mathrm{Im}\{\chi\}$) as function of the probe energy at different delay times after the pump pulse for the conditions discussed in the last section (band edge excitation in $MoSe_2$). The colour shaded curves result from the dynamics at room temperature, while the black curves show the resulting spectra simulated for 77 K. Shortly after the pump pulse (t=0.5-1ps) we find several absorption peaks at low energies, stemming from close lying transitions of the excited higher order exciton states >2s. In particular, our calculations predict that transient population inversions between s- and p-types states arise during the relaxation process, since the relaxation preferably occurs between states with the same orbital symmetry. For the spectra measured at 77 K, where the absorption lines become narrow enough due to a reduced exciton-phonon scattering, we therefore observe pronounced gain signals (i.e. negative absorption). With increasing delay time, as the population relaxes towards a thermal Boltzmann distribution, we find a shift of the response towards the 1s-2p transition energy,

stemming from excitons in the ground state. The rise time of the 1s-2p resonance is a direct measure of relaxation from free to bound states. In Paper 1 we further discuss the different spectral features and the comparison with experiments. This study shows that the developed theoretical approach presents a powerful tool for the investigation of exciton relaxation dynamics and can be applied to a wide range of excitonic systems. In particular, in a joint experiment-theory study, we showed that the exciton binding energy is significantly reduced within an hBN-capped TMD compared to a "naked" monolayer in Paper 11. Within the same partnership, we demonstrated in Paper 24 how the exciton binding energy can be tuned in a homobilayer by controlling the degree of interlayer hybridizaion through the stacking angles, which is discussed in Sec. 9. Moreover, we applied a similar approach as the one presented above, to model the exciton dynamics in a van der Waals heterostructure, consisting of two different monolayers, published in Paper 14 and 18.

7.4 Spatiotemporal Dynamics

The microscopic model for the relaxation dynamics presented in the last sections can be extended to also describe spatially inhomogeneous systems, giving rise to equilibration processes like diffusion. Here it is not sufficient to restrict the treatment to momentum diagonal elements of the excitonic density matrix $\langle X^\dagger_{\mathbf{Q}} X^\dagger_{\mathbf{Q}}\rangle$, but the evolution of off-diagonal elements $\langle X^\dagger_{\mathbf{Q}} X^\dagger_{\mathbf{Q}'}\rangle$ is containing essential information about the spatial distribution. Details on this approach are given in Paper 19 and 21 and references therein. Here we just shortly introduce the concept of excitonic Wigner functions as possible extension of the presented model of the exciton relaxation. Starting point of the theoretical description of a spatially inhomogeneous exciton distribution is the pair probability density,

$$\rho(\mathbf{r}_e,\mathbf{r}_h) = \langle \psi^\dagger_e(\mathbf{r}_e)\psi_e(\mathbf{r}_e)\psi^\dagger_h(\mathbf{r}_h)\psi_h(\mathbf{r}_h)\rangle, \tag{7.19}$$

which corresponds to the probability of finding an electron at position $\mathbf{r}_e$ *and* simultaneously a hole at position $\mathbf{r}_h$. Next we expand the particle field operators ψ in terms of valence and conduction band operators within the effective mass approximation and introduce a relative coordinate $\mathbf{r} = \mathbf{r}_e - \mathbf{r}_h$ and center-of-mass coordinate $\mathbf{R} = \alpha\mathbf{r}_e - \beta\mathbf{r}_h$, which yields

$$\rho(\mathbf{r},\mathbf{R}) = \frac{1}{A^2}\sum_{\mathbf{k}\mathbf{k}'\mathbf{Q}\mathbf{Q}'} e^{i(\mathbf{Q}-\mathbf{Q}')\mathbf{R}} e^{i(\mathbf{k}-\mathbf{k}'+\beta(\mathbf{Q}-\mathbf{Q}'))\mathbf{r}} \langle c^\dagger_{\mathbf{k}+\mathbf{Q}} v_{\mathbf{k}} v^\dagger_{\mathbf{k}'} c_{\mathbf{k}'+\mathbf{Q}'}\rangle. \tag{7.20}$$

The appearing operator combination $c^\dagger v$ can now be expanded in terms of exciton operators (Eq. 5.9), which reads

$$\rho(\mathbf{r},\mathbf{R}) = \sum_{\nu\mu\mathbf{q}\mathbf{Q}} \tilde{\mathcal{F}}_{\nu\mu}(\mathbf{r}) \langle X^\dagger_{\mu\mathbf{Q}+\mathbf{q}} X_{\nu\mathbf{Q}}\rangle e^{i(\mathbf{q})\mathbf{R}}, \tag{7.21}$$

where $\tilde{\mathcal{F}}_{\nu\mu}(\mathbf{r})$ denotes the Fourier transform of the excitonic form factor (Eq. 4.37). In Eq. 7.21 we already see that all the spatial information is contained in the off-diagonal elements of the exciton density matrix. However, we are usually only interested in the probability of finding an exciton at a certain *center-of-mass position*, which is given by

$$\rho(\mathbf{R}) = \int d^2r \rho(\mathbf{r},\mathbf{R}) = \sum_{\mu\mathbf{q}\mathbf{Q}} \langle X^\dagger_{\mu\mathbf{Q}+\mathbf{q}} X_{\mu\mathbf{Q}} \rangle e^{i(\mathbf{q})\mathbf{R}} = \frac{1}{A} \sum_{\mu\mathbf{Q}} N^\mu_{\mathbf{Q}}(\mathbf{R}), \tag{7.22}$$

where in the last step we have introduced the excitonic Wigner function $N^\mu_{\mathbf{Q}}(\mathbf{R})$. The latter contains all the information needed to obtain the probability distribution in momentum ($\int d^2R$) or in space ($\sum_{\mathbf{Q}}$). An extensive review on electronic Wigner functions within the density matrix formalism is given in Ref. [36]. With the above interpretation and the excitonic Hamiltonian most of the considerations in Ref. [36] can be directly transferred to excitons, as long as the length scale of spatial fluctuations in density are small compared to the exciton Bohr radius.

In Paper 19, 21, 20 and 29 we discuss several intriguing phenomena in the exciton diffusion, such as the formation of spatial exciton rings, effective negative diffusion coefficients as well as the effect of strain on exciton transport.

CHAPTER 8

INTERLAYER EXCITONS IN VAN DER WAALS BILAYERS

So far our analysis has entirely focused on TMD monolayers and the different exciton states therein. However an exciting opportunity to increase the electronic degrees of freedom, is to vertically stack two monolayer TMDs into a so called bilayer structure. While homobilayers (two layers of the same material) have long been considered as boring byproduct of the exfoliation process for monolayers, the discovery of superconductivity in magic angle bilayer graphene [23, 24] has spiked interest for possible, similarly exotic quantum behaviour in bilayer TMDs. In particular, the possibility to artificially engineer the materials properties by choosing different monolayer components and varying the relative angle at which the two materials are stacked upon each other, dramatically increases the playground for many-particle physics and possible applications. One of the main novelties of a bilayer in comparison to single layers, is that excitons can either be composed of electrons and holes residing in the same layer (intralayer excitons) or can be made of a spatially separated electron-hole pair extending over both layers [25–29]. In this section, we introduce the general model Hamiltonian, which is used in this work to describe electronic and excitonic eigenstates in bilayers.

8.1 Electrons and Phonons in van der Waals Bilayers

Monolayer materials are also referred to as van der Waals materials, since their bulk counterparts consist of atomic layers which only weakly interact with each

other via van der Waals forces, while atoms within the same layer have strong covalent bonds. Nevertheless, the electronic structure of monolayers is undergoing significant modifications when they are stacked up to a bilayer. However, it is still convenient to use the monolayer eigenstates as basis functions of the bilayer Hamiltonian. In particular, many phenomena observed in a bilayer can already be described within a simplified frame considering two decoupled monolayers. Physical effects which go beyond this simplified picture can than be intuitively interpreted in the monolayer basis by adding interlayer interaction terms to the Hamiltonian, e.g. accounting for an overlap of the wave functions in different layers.

Hence, we extend the model Hamiltonian introduced for monolayers in Sec. 3.1 by simply adding a binary quantum number l for the lower ($l = 0$) and upper layer ($l = 1$)

$$|\lambda\zeta\mathbf{k}\rangle \longrightarrow |\lambda l\zeta\mathbf{k}\rangle \tag{8.1}$$

$$\varepsilon^{\lambda}_{l\zeta\mathbf{k}} = \varepsilon^{\lambda}_{l\zeta 0} + \sigma_{\lambda}\frac{\hbar^2}{2m^{\lambda}_{l\zeta}}\mathbf{k}^2 \tag{8.2}$$

Here the effective band masses $m^{\lambda}_{l\zeta}$ remain unchanged with respect to the monolayer. In contrast, the band gap and the correct alignment of valence and conduction band in both layers strongly depend on the considered combination of materials as well as their stacking.

In Figure 8.1 illustrates the atomic registries for different high-symmetry stackings. Thereby the grey notation is used in many publications, but is less precise

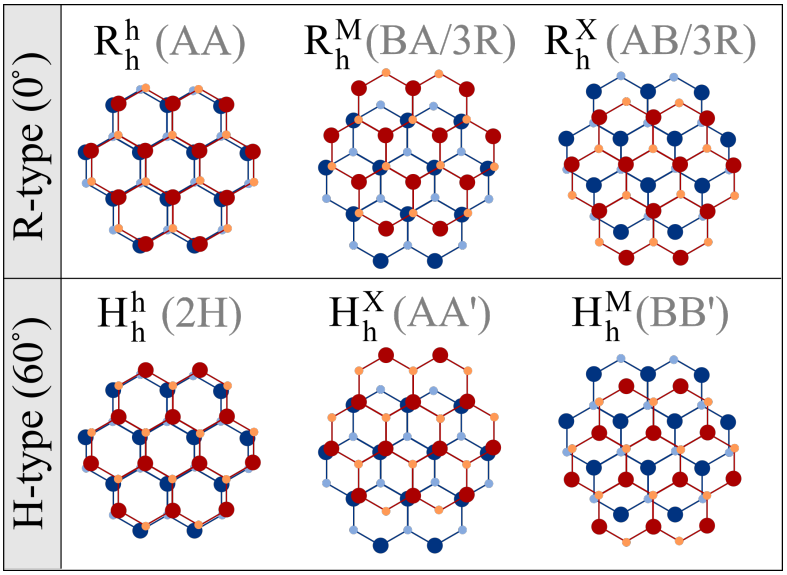

Figure 8.1: Definition of different high-symmetry stacking geometries.

than the alternative notation (black), which we will use in this work. Here R(H)

stands for perfectly aligned lattices with 0° (60°) angle, meaning that one initially places the metal atoms of one layer on top of the metal (chalcogen) atoms of the other layer, yielding the R_h^h (H_h^h) stacking (h=hole/void). The other stackings then result from lateral shifts of one layer along a high-symmetry line, so that e.g. a metal (M) or a chalcogen atom (X) of the upper layer is above the hole/void of the other layer, denoted by e.g. $R_h^{M/X}$.
In *homobilayers* with R-type stacking the electronic bands of the decoupled monolayers are degenerate, i.e. $\varepsilon^\lambda_{0,\zeta 0} = \varepsilon^\lambda_{1,\zeta 0}$. However, a relative rotation of both layers in real space leads to the same rotation of the Brillouin zones in reciprocal space. Therefore for 60° rotated layers, the K point of one layer corresponds to the K' point in the other layer. In this case, we rename K to K' but invert the spin-ordering of bands in both layers. Hence, for H-type stacking, bands with equal spins are separated by the spin-orbit splitting, i.e. $\varepsilon^\lambda_{0,\zeta 0} = \varepsilon^\lambda_{1,\zeta 0} + \Delta^{\mathrm{SOC}}_{\lambda\zeta}$. In addition to this the band gap is undergoing a significant renormalization due to the Coulomb screening added by the second layer. However, for the properties of the exciton and its dynamics the band gap does play a minor role and just adds a constant shift to emission and absorption energies.
For a *heterostructure*, the above mentioned difference between R- and H-type stacking is still true. However, in addition to that two different monolayers have different band gaps and the band alignment usually has a constant offset $\varepsilon^\lambda_{0,\zeta 0} = \varepsilon^\lambda_{1,\zeta 0} + \Delta^{\mathrm{vac}}$, resulting from different work functions (vacuum potentials). The latter needs to be determined through first principles calculations or adjustments to experiments, cf. Sec. 10.1.
Apart from the above mentioned arguments which hold for the energy alignment of two completely decoupled monolayers, we will discuss energy changes due to interlayer hybridization in Sec. 9 as well as alignment shifts resulting from the electrostatic potential of the adjacent layer in Sec. 10.
Throughout this work we do not consider any changes in the phonon modes of the two monolayers, when they are stacked. This is justified by the weak van der Waals forces between atoms in different layers compared to the strong in-plane bonds. Consequently, we again just add a layer index to the phonon quantum number $j = (\kappa_j, \zeta_j^{\mathrm{ph}}) \to (l_j, \kappa_j, \zeta_j^{\mathrm{ph}})$, while their energies as well as electron phonon coupling elements remain unchanged. It is important to note that in this decoupled basis direct phonon scattering between states in different layers is forbidden, i.e. $D^{j\lambda}_{l_1\zeta_1, l_2\zeta_2\mathbf{q}} \propto \delta_{l_j,l_1}\delta_{l_j,l_2}$. We will however show in Sec. 9.3 that interlayer hybridization of electronic states can lead to a phonon scattering between layer mixed states, which , e.g., can lead to a phonon-assisted charge transfer between both layers.

In contrast to the electron-phonon interaction, the Coulomb potential of an electron sitting in one layer extends into the other layer. Hence, charges sitting in different layers are subject to their mutual Coulomb forces and can form interlayer excitons.

8.2 Interlayer Coulomb Potential

In order to describe the Coulomb potential of charges within a bilayer system, we need to modify our screening model presented in Sec. 3.4. To this end, we again solve the Poisson equation, however for a dielectric environment of two homogeneous dielectric slabs on top of each other [29, 123, 124],

$$\epsilon^i(\mathbf{r}) = \begin{cases} \epsilon^i_{\text{bg}} & \text{for } z < -d_0 \\ \epsilon^i_0 & \text{for } -d_0 < z < 0 \\ \epsilon^i_1 & \text{for } 0 < z < d_1 \\ \epsilon^i_{\text{bg}} & \text{for } z > d_1. \end{cases} \tag{8.3}$$

If we now place a point charge in the middle of layer l ($z_0 = \pm d_l/2$) we can use the above definition to define boundary conditions for the electric field and determine the Coulomb potential experienced by another charge in layer l' at $z = \pm d_{l'}/2$ which yields [124],

$$V^{ll'}_{\mathbf{q}} = \frac{e_0^2}{2\epsilon_0 A q \epsilon^{ll'}_s(q)}; \quad \epsilon^{ll'}_s(q) = \begin{cases} \epsilon_{\text{inter}}(q) & \text{for } l \neq l' \\ \epsilon^l_{\text{intra}}(q) & \text{for } l = l' \end{cases} \tag{8.4}$$

$$\epsilon_{\text{inter}}(q) = \kappa_{\text{bg}} g^0_q g^1_q f_q \quad \text{and} \quad \epsilon^l_{\text{intra}}(q) = \frac{\kappa_{\text{bg}} g^{1-l}_q f_q}{\text{ch}(\delta_{1-l}q/2) h^l_q} \tag{8.5}$$

with the abbreviations,

$$\begin{aligned} f_q &= 1 + \frac{1}{2}\Big[(\frac{\kappa_0}{\kappa_{\text{bg}}} + \frac{\kappa_{\text{bg}}}{\kappa_0})\text{th}(\delta_0 q) + (\frac{\kappa_1}{\kappa_{\text{bg}}} + \frac{\kappa_{\text{bg}}}{\kappa_1})\text{th}(\delta_1 q) + (\frac{\kappa_0}{\kappa_1} \\ &\quad + \frac{\kappa_1}{\kappa_0})\text{th}(d_0 q)\text{th}(\delta_1 q)\Big], \\ h^l_q &= 1 + \frac{\kappa_{\text{bg}}}{\kappa_l}\text{th}(\delta_l q) + \frac{\kappa_{\text{bg}}}{\kappa_{1-l}}\text{th}(\delta_{1-l} q/2) + \frac{\kappa_l}{\kappa_{1-l}}\text{th}(\delta_l q)\text{th}(\delta_{1-l} q/2), \\ g^l_q &= \frac{\text{ch}(\delta_l q)}{\text{ch}(\delta_{1-l} q/2)\big[1 + \frac{\kappa_{\text{bg}}}{\kappa_l}\text{th}(\delta_l q/2)\big]}. \end{aligned} \tag{8.6}$$

Here we used the short notations $\text{ch}(\cdot) = \cosh(\cdot)$, $\text{th}(\cdot) = \tanh(\cdot)$ and $\delta_l = \alpha_l d_l$ [29], where α_l and κ_l are defined by the dielectric constants (cf. Sec. 3.4) and d_l is the thickness of layer $l = 0{,}1$.
This modified potential has two important consequences: i) The potential between electrons and holes within the same layer is strongly screened by the presence of the adjacent second layer ($\epsilon^{\parallel}_{TMD} \sim 15$). ii) The potential between two charges in different layers is even more suppressed, since their distance is constraint by their difference in z coordinates $\Delta z = (d_0 + d_1)/2$. This constraint is implicitly included into the effective 2D Coulomb potential $V^{ll'}_{\mathbf{q}}$ via the function ϵ_{inter}. This allows us

to treat the bilayer as a 2D system, while the spatial configuration of states in z-direction is encoded in the strength of the matrix elements. Although the interlayer distance changes with the stacking geometry, the variation is usually within 10% of the bulk interlayer distance [30]. This would result in small variations of binding energy in the range of a few meV. We therefore neglect this variation for the treatment of the Coulomb interaction and use the thickness parameters d_l for monolayers [70] also in Eq. 8.4.

8.3 Interlayer Excitons

With the above definition of the Coulomb potential, the corresponding Hamiltonian reads

$$H = \frac{1}{2} \sum_{\lambda l \zeta \mathbf{k} \lambda' l' \zeta' \mathbf{k}' \mathbf{q}} V_{\mathbf{q}}^{ll'} a^\dagger_{\lambda l \zeta, \mathbf{k}+\mathbf{q}} a^\dagger_{\lambda' l' \zeta', \mathbf{k}'-\mathbf{q}} a_{\lambda' l' \zeta', \mathbf{k}'} a_{\lambda l \zeta, \mathbf{k}} \tag{8.7}$$

Since all three quantum number band λ, valley ζ and layer l are conserved, we can generalize the transformation into exciton basis to include interlayer excitons, in analogy to the treatment of intervalley excitons by replacing $\zeta \to \xi = (\zeta,l)$. After this step we can apply the same transformation rules as for intervalley excitons, cf. Sec. 5.3, just that the exciton super index $\mu = (n_\mu,L_\mu,l^e_\mu,\zeta^e_\mu,l^h_\mu,\zeta^h_\mu)$ now also contains electron/hole layer l_e/l_h. Consequently, the exciton wavefunctions Ψ now have to fulfill the interlayer Wannier equation,

$$\frac{(\hbar \mathbf{k})^2}{2m_r^{l_e \zeta_e l_h \zeta_h}} \Psi(\mathbf{k}) - \sum_{\mathbf{q}} V_{\mathbf{q}}^{l_e l_h} \Psi(\mathbf{k}+\mathbf{q}) = E^{\mathrm{b}} \Psi(\mathbf{k}). \tag{8.8}$$

This equation is formally equivalent to the normal Wannier equation and can therefore be solved with the method describe in Sec. 4.4. Figure 8.2 shows the solution of the interlayer Wannier equation for a WSe_2 bilayer. In a) we compare the binding energy of the intralayer ground state 1s (X0) exciton with the interlayer exciton (iX), composed of the same band configuration (A exciton) but with electron and hole in different layers. For both intra- and interlayer excitons we find strongly reduced binding energies compared to the monolayer (Sec. 4.4). For the intralayer exciton this results from the additional screening created by the second layer. For the interlayer exciton the binding energy is further reduced due to the distance constraints for the electron and hole (Paper 14&18). For the intralayer exciton, electron and hole can be at the same position, which contributes a large fraction of the Coulomb energy. In contrast, in the interlayer exciton, electron and hole are always separated by a minimal distance given by the interlayer separation. Therefore, their mutual Coulomb potential does not diverge as $r \to 0$, but goes to a finite value, which significantly reduces the expectation value of the potential energy. However, when comparing the 2p state energies, we find almost the same result for intra- and interlayer excitons. This is because for p-types states

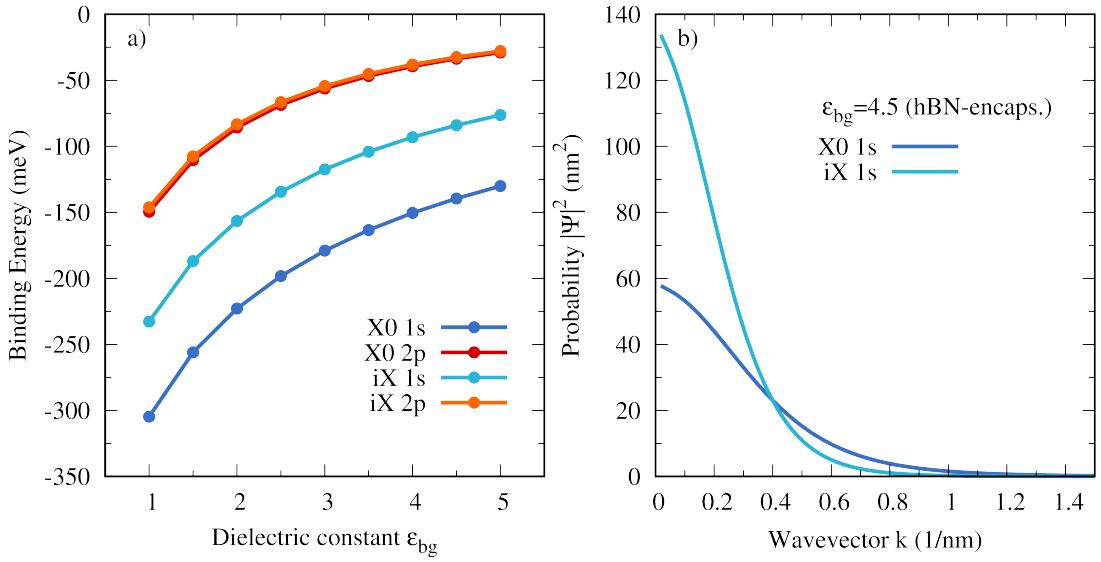

Figure 8.2: Solution of the interlayer Wannier equation for a WSe_2 bilayer. a) Binding energy of the 1s and 2p state for the intralayer (X0) and the interlayer exciton (iX) with the same band configuration but with electron and hole in different layers. b) Wave function of the 1s intra- and interlayer exciton within an hBN encapsulated sample.

the probability $|\Psi_{2p}(r=0)|^2 = 0$, so that the above explained difference between the effective intra- and interlayer potential is not relevant. In Figure 8.2b) the wave functions of intra- and interlayer ground state are compared for the dielectric environment corresponding to an hBN-encapsulation. Again we see that the interlayer exciton wave function is much narrower in momentum space (broader in real space) than its intralayer counter part, reflecting the reduced Coulomb force between layer separated electron-hole pairs.

CHAPTER 9

INTERLAYER HYBRIDIZATION IN TWISTED HOMOBILAYERS

In addition to the emergence of interlayer excitons, TMD bilayers have other important features distinguishing them from their monolayer counterparts. An important difference is the mixing or hybridization of electronic states in both layers [125–129]. A simple analogy to this phenomenon is the emergence of molecular orbitals, when e.g. two hydrogen atoms are brought close to each other. While the well known hydrogen orbitals are solutions of the Schrödinger equation containing a single nucleus, the solution for two closely spaced nuclei is well approximated by a superposition of two hydrogen orbitals, as depicted in Fig. 9.1.

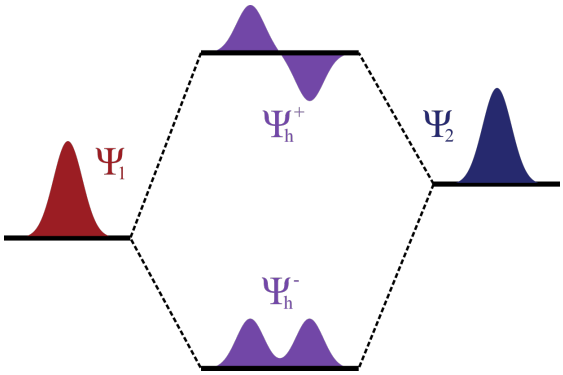

Figure 9.1: Hybridization and avoided crossing resulting from the overlap between two quantum states.

The resulting superpositions can be referred to as hybrid states and the resulting splitting between the bonding and anti-bonding state is a direct measure for the interaction strength between the two initial states. The same principle applies to

the monolayer eigenfunctions, which are strongly localized within the out of plane direction. When two layers are stacked on top of each other, the two monolayer wave functions will overlap, so that an energetically more favourable state is given by a hybrid state, which is delocalized across both layers. In the following section, we investigate how this interlayer hybridization can be described within our many-particle formalism. Here, the special focus lies on the role of the Coulomb interaction as well as the impact of different stacking geometries. In particular, we focus on the theoretical modeling of homobilayers, since here the hybridization effects should be strong as a result of degenerate monolayer states.

9.1 Interlayer Hopping - Tunneling Hamiltonian

In order to model the interlayer hybridization we set up an effective single particle Hamiltonian for valence and conduction band electrons in the bilayer,

$$H_0^I = -\frac{\hbar^2}{2m_0}\nabla^2 + V_0(r) + V_1(r), \tag{9.1}$$

where V_l is the effective electrostatic potential created by the nuclei and core electrons of layer $l = 0,1$. Now we use Eq. 2.12 to transform this Hamiltonian into second quantization. Thereby we restrict the Fock space to the monolayer eigenstates of valence and conduction band electrons (for simplicity only one valley) which yields,

$$\begin{aligned} H_0 &= \sum_{\lambda\lambda' ll' \mathbf{k}\mathbf{k}'} \langle \lambda l \mathbf{k} | H_0^I | \lambda' l' \mathbf{k}' \rangle a^\dagger_{\lambda l \mathbf{k}} a_{\lambda' l' \mathbf{k}'} \\ &= \sum_{\lambda l \mathbf{k}} \varepsilon^\lambda_{l\mathbf{k}} a^\dagger_{\lambda l \mathbf{k}} a_{\lambda l \mathbf{k}} + H_T + H_M \qquad (9.2) \\ H_T &= \sum_{\lambda, l \neq l', \mathbf{k}\mathbf{q}} T^\lambda_{ll'}(\mathbf{q},\mathbf{k}) a^\dagger_{\lambda l \mathbf{k}+\mathbf{q}} a_{\lambda l' \mathbf{k}}; \\ &\text{with} \quad T^\lambda_{ll'}(\mathbf{q},\mathbf{k}) = \langle \lambda l \mathbf{k} + \mathbf{q} | V_0 + V_1 | \lambda l' \mathbf{k} \rangle \qquad (9.3) \\ H_M &= \sum_{\lambda l \mathbf{k}\mathbf{q}} \mathcal{V}^\lambda_l(\mathbf{q},\mathbf{k}) a^\dagger_{\lambda l \mathbf{k}+\mathbf{q}} a_{\lambda l \mathbf{k}}; \\ &\text{with} \quad \mathcal{V}^\lambda_l(\mathbf{q},\mathbf{k}) = \langle \lambda l \mathbf{k} + \mathbf{q} | V_{1-l} | \lambda l \mathbf{k} \rangle. \qquad (9.4) \end{aligned}$$

Here we neglected the mixing of states in different bands ($\lambda' = \lambda$) and used that the basis functions of layer l are eigenstates of the respective potential V_l with the eigenenergy $\varepsilon^\lambda_{l\mathbf{k}}$, reflecting the monolayer band structure. Moreover, we introduced two new Hamiltonians, which now contain the main modifications of the electronic structure. The moiré Hamiltonian H_M contains the electrostatic energy shifts that

introduce the change of the potential energy of electrons in layer $l = 0{,}1$ due to the presence of the electrostatic potential stemming from atoms in the other layer $1 - l$. This effect will be in detail discussed in Sec. 10.1. In this section we focus on the interlayer hopping/tunneling Hamiltonian H_T.

This term leads to a transfer of carriers from $|\lambda l' \mathbf{k}'\rangle$ to the other layer $|\lambda l \mathbf{k}\rangle$, with a rate determined by the wave function overlap within $T^{\lambda}_{ll'}$. However, for strong interlayer interactions, this term also leads to a significant energy shift and wave function mixing, which has important consequences on other interaction mechanisms. Therefore, the goal of the next section will be to find a basis transformation which brings H_0 into a diagonal form.

Tunneling Matrix Element

Before we can find a suitable diagonalization strategy, we first need to determine the general properties of the tunneling matrix element $T^{\lambda}_{ll'}(\mathbf{q},\mathbf{k})$. In the following, we use a tight binding approach to deduce the momentum selection rules for an interlayer hopping process. Thereby we follow the derivation given in Ref. [62]. In the following, we suppress the band index λ and use compound indices $i = (l_i,\zeta_i)$. The electronic wave function in vicinity of valley ζ (here used as a vector in reciprocal space) is approximately [62]:

$$\Psi_{i\mathbf{k}}(\mathbf{r}) = \frac{1}{\sqrt{N}} \sum_{\mathbf{R}_i} e^{i(\zeta_i + \mathbf{k})\mathbf{R}_i} \Phi_i(\mathbf{r} - \mathbf{R}_i). \tag{9.5}$$

It is important to note that although the we use decoupled layers as basis functions, their wave function still live in the same coordinate system. Consequently, a relative shift and/or rotation of the two layers, will i) modify the atomic positions $\mathbf{R}_i$ in layer l_i and ii) rotate their Brillouin zones accordingly so that $\zeta_i \neq \zeta_j$ although we refer to the same high-symmetry point, e.g.$|\zeta_i| = |\zeta_j| = |K|$. Using Eq. 9.5 we can express the tunneling matrix element in terms of hopping integrals,

$$h_{ij}(\mathbf{R}) = \frac{1}{A_{\mathrm{uc}}} \int d^3r \Phi_i^*(\mathbf{r}) V_i(\mathbf{r}) \Phi_j(\mathbf{r} + \mathbf{R}) \tag{9.6}$$

$$= \frac{1}{A} \sum_{\mathbf{q}} \tilde{h}_{ij}(\mathbf{q}) e^{i\mathbf{q}\mathbf{R}}, \tag{9.7}$$

where we introduced the in-plane Fourier transform with respect to the 2D displacement $\mathbf{R}$ in the second line. The remaining sums over lattice coordinates $\mathbf{R}_i$ now yield momentum conservation via the identity,

$$\frac{1}{N} \sum_{\mathbf{R}_i} e^{i\mathbf{q}\mathbf{R}_i} = \sum_{\mathbf{G}_i} e^{i\mathbf{G}_i\mathbf{R}_i^0} \delta_{\mathbf{q},\mathbf{G}_i}, \tag{9.8}$$

where $\mathbf{R}_i^0$ is the position of the atom in layer l_i, which is closest to the center of the real space coordinate system. In the following, we introduce the convention that the real space coordinate system is centered in the middle of a connection line between nearest neighbours of different layers, i.e. $\mathbf{R}_i^0 = -\mathbf{R}_j^0 = \mathbf{D}_i/2$ for $(i \neq j)$. With Eq. 9.6 and 9.8, and further restricting to a small vicinity of the high-symmetry point $|\mathbf{k}| \ll |\zeta|$ we find,

$$T_{ij}(\mathbf{q},\mathbf{k}) = \sum_{\mathbf{G}_i,\mathbf{G}_j} t_{ij}(\zeta_j + \mathbf{G}_j) e^{i(\mathbf{G}_i+\mathbf{G}_j)\mathbf{D}_i/2} \delta_{\mathbf{q},\zeta_j+\mathbf{G}_j-\zeta_i-\mathbf{G}_i}, \tag{9.9}$$

with the abbreviation $t_{ij}(q) = \tilde{h}_{ij}(\mathbf{q}) + \tilde{h}^*_{ji}(\mathbf{q})$. The appearing sum over reciprocal lattice vectors can be further simplified by assuming that the hopping integrals decay quickly in momentum space [62]. In this case, we can restrict the sum over $\mathbf{G}$ to $\mathbf{G}_i = 0$ and the "first shell" with $|\mathbf{G}_i| = |\mathbf{G}_i^{(0)}|$, where $\mathbf{G}_i^{(0)}$ is one of the two fundamental translations of the reciprocal lattice. Moreover, the chosen representation of electronic operators contains the restriction that the valley local momenta $\mathbf{k}$ and $\mathbf{k}+\mathbf{q}$ are in close vicinity to the respective high-symmetry point and are therefore small compared to $\mathbf{G}$ vectors. Consequently, the δ-function in Eq. 9.9 implies that for small twist-angles only tunneling between equivalent high-symmetry points $\zeta_i \approx \zeta_j$ is allowed, e.g. between the two slightly shifted K points of both layers. For intervalley processes, e.g. $\zeta_i = \Lambda$ and $\zeta_j = K$ the δ-function gives large momenta $\mathbf{q}$ which violate the valley local approximation and therefore have to be disregarded.

In the following, we keep the general notation with ζ_i and ζ_j, but keep in mind that $\zeta_i \approx \zeta_j$. In order to further simplify Eq. 9.9 within a first shell approximation, we now have to distinguish between different high symmetry points.

Tunneling at the K Point

A special situation arises when considering electrons at the edge of the Brillouin zone $\zeta_i = \tau K_i$ ($\tau = -1$ for K' and $\tau = 1$ else), because here we find three different $\mathbf{G}$-vectors with $|\zeta_i + \mathbf{G}_i| = |\zeta_i|$, given by $\mathbf{G}_i^n = \tau(C_3^n K_i - K_i)$, where C_3 is a 120° rotation and n = 0,1,2. Furthermore, when restricting to small twist angles, it holds $|\zeta_i - \zeta_j|,q \ll |\mathbf{G}_i^{(0)}|$. Therefore, when choosing a specific $\mathbf{G}_i = \mathbf{G}_i^n$, the sum over $\mathbf{G}_j$ only contributes with the terms $\mathbf{G}_j = \mathbf{G}_j^n$. Consequently, Eq. 9.9 reduces to

$$T_{ij}(\mathbf{q}) \approx \sum_{n=0}^{2} \theta_{ij}^{(n)} \delta_{\mathbf{q},\tau C_3^n(K_j-K_i)}, \tag{9.10}$$

with $\theta_{ij}^{(n)} = t_{ij}(\tau C_3^n K_j) \exp(i\tau(C_3^n K_i - K_i + C_3^n K_j - K_j)\mathbf{D}_i/2)$. Finally, we use the angular symmetry of d-orbitals [62], $\Phi(C_3^n \mathbf{r}) = \exp(im_z 2\pi n/3)\Phi(\mathbf{r})$, with the

magnetic quantum numbers $m_z^c = 0$ and $m_z^v = \pm 1$ for K(K') point. Thus we obtain

$$\theta_{ij}^{(n)} = \theta_0 \exp\left(i2\pi n \Delta m_z/3 + i\tau(C_3^n K_i - K_i + C_3^n K_j - K_j)\mathbf{D}_i/2\right), \tag{9.11}$$

where $\Delta m_z = (-1)^{l_j}$ for H-type stacking in the valence band and $\Delta m_z = 0$ else. Moreover, we have introduced $\theta_0 = t_{ij}(\tau K_j)$, which remains the only unknown parameter and can be extracted from ab initio calculations (cf. Sec. 9.4).

Tunneling at Γ and Λ

The above consideration does not hold for high-symmetry points deep within the first Brillouin zone, such as $\zeta_i = \Gamma_i, \Lambda_i$, since here the addition of a reciprocal lattice vector will always lead outside of the first Brillouin zone. Therefore, we can set $t_{ij}(\zeta_j + \mathbf{G}_j) << t_{ij}(\zeta_i)$ for all $\mathbf{G_j} \neq 0$ [62]. Hence, the sum in Eq. 9.9 reduces to the term with $\mathbf{G}_i, \mathbf{G}_j = 0$ yielding,

$$T_{ij}(\mathbf{q},\mathbf{k}) \approx \theta_0 \delta_{\mathbf{q},\zeta_j - \zeta_i}, \tag{9.12}$$

where again $\theta_0 = t_{ij}(\zeta_j)$. It is important to note at this point that the form of the tunneling Hamiltonian (Eq. 9.3) is indicating that this process is accompanied with a momentum transfer $H_T \propto a^\dagger_{i\mathbf{k}+\mathbf{q}} a_{j\mathbf{k}}$ with $\mathbf{q} = \zeta_j - \zeta_i$. This results from the chosen (valley local) coordinate system which measures momenta $\mathbf{k}$ with respect to the closest high-symmetry point. In global coordinates, i.e. $a_{i\mathbf{k}} = \tilde{a}_{l_i,\mathbf{k}+\zeta_i}$ the tunneling process is momentum conserving $H_T \propto \tilde{a}^\dagger_{l_i,\mathbf{k}+\mathbf{q}+\zeta_i} \tilde{a}_{l_j,\mathbf{k}+\zeta_j} = \tilde{a}^\dagger_{l_i,\mathbf{k}+\zeta_j} \tilde{a}_{l_j,\mathbf{k}+\zeta_j}$. Hence, the momentum selection rule in Eq. 9.12 is only compensating for the offset between the local coordinate systems of initial and final state. In contrast, when considering tunneling at the K point (Eq. 9.10), there are three allowed momentum transfers $\mathbf{q} = C_3^n(K_j - K_i)$, which even in global coordinates $H_T \propto \tilde{a}^\dagger_{l_i,\mathbf{k}+\zeta_j+\mathbf{b}_n^{ji}} \tilde{a}_{l_j,\mathbf{k}+\zeta_j}$ gives rise to a transferred momentum $\mathbf{b}_n^{ji} = (C_3^n - \mathbb{1})(K_j - K_i) = \mathbf{G}_j^n - \mathbf{G}_i^n$. This arises from the fact that there are three equivalent K points in the corners of the first Brillouin zone, which can be connected with a reciprocal lattice vector $\mathbf{G}_i^n$. Consequently, we can either tunnel directly from K_j to K_i or, alternatively from $K_j + \mathbf{G}_j$ (same as K_j) to $K_i + \mathbf{G}_j$, which in turn is equivalent to $K_i + \mathbf{G}_j - \mathbf{G}_i$. Hence, the fact that we can arbitrarily add reciprocal lattice vectors from both layers, is introducing a new reciprocal lattice vector $\mathbf{b}_n = \mathbf{G}_1^n - \mathbf{G}_0^n$, characterizing the superlattice in real space. This will be further discussed in Sec. 9.2.

Excitonic Tunneling Hamiltonian

With the tunneling matrix elements determined in the last section, we could in principle diagonalize the electronic Hamiltonian Eq. 9.2 and would obtain two

layer hybridized (valence/conduction) bands, instead of two degenerate bands localized in one of the two layers. However, if we then want to calculate excitonic eigenstates, we also need to transform the Coulomb interaction into hybrid basis, which would then mix all four hybrid bands (two valence and two conduction bands). Together with the complex momentum selection rules for the tunnelling, creating moiré minibands (cf. Sec. 9.2), the layer mixing would dramatically increase the numerical complexity of the exciton Wannier equation.

Therefore we first consider the Coulomb interaction and transform the bilayer Hamiltonian into exciton basis, with decoupled intra- and interlayer states. Subsequently, we transform into a hybrid exciton basis, which diagonalizes the excitonic Hamiltonian containing excitonic interlayer tunneling terms. Starting from the general form of the tunneling Hamiltonian (compound index $i = (l_i,\zeta_i)$)

$$H_T = \sum_{\lambda,i\neq j,\mathbf{kq}} T_{ij}^{\lambda}(\mathbf{q}) a^{\dagger}_{\lambda i\mathbf{k}+\mathbf{q}} a_{\lambda j\mathbf{k}} \tag{9.13}$$

we use the expansion into pair operators

$$A^{\dagger}_{i\mathbf{k},j\mathbf{k}'} = a^{\dagger}_{ci\mathbf{k}} a_{vj\mathbf{k}'}, \tag{9.14}$$

$$a^{\dagger}_{ci\mathbf{k}} a_{cj\mathbf{k}'} \approx \sum_{h\mathbf{p}} A^{\dagger}_{i\mathbf{k},h\mathbf{p}} A_{j\mathbf{k}',h\mathbf{p}} \tag{9.15}$$

$$a^{\dagger}_{vi\mathbf{k}} a_{vj\mathbf{k}'} \approx \delta^{ij}_{\mathbf{kk}'} - \sum_{h\mathbf{p}} A^{\dagger}_{h\mathbf{p},j\mathbf{k}'} A_{h\mathbf{p},i\mathbf{k}} \tag{9.16}$$

together with the exciton basis

$$A^{\dagger}_{i\mathbf{k},j\mathbf{k}'} = \sum_{\mu} X^{\mu\dagger}_{ij,\mathbf{k}-\mathbf{k}'} \Psi^{\mu}_{ij}(\alpha_{ij}\mathbf{k}' + \beta_{ij}\mathbf{k}) \tag{9.17}$$

Finally we restrict our consideration to the excitonic ground states $\mu = 1\mathrm{s}$ for intra and interlayer excitons, because for small twist angles the wave function overlap between the 1s and higher order states is negligible. However, if we want to calculate hybridized p-type states, the mixing between orbitals of different character can become the leading contribution (Paper 24). For tunneling between intra- and interlayer ground states we find,

$$\begin{aligned} H_0 = &\sum_{ij\mathbf{Q}} E_{ij\mathbf{Q}} X^{\dagger}_{ij\mathbf{Q}} X_{ij\mathbf{Q}} \\ &+ \sum_{i\neq j,h,\mathbf{Q},\mathbf{q}} \mathcal{T}^{c}_{ih,jh}(\mathbf{q}) X^{\dagger}_{jh,\mathbf{Q}+\mathbf{q}} X_{ih,\mathbf{Q}} \\ &- \sum_{i\neq j,h,\mathbf{Q},\mathbf{q}} \mathcal{T}^{v}_{hi,hj}(\mathbf{q}) X^{\dagger}_{hj,\mathbf{Q}+\mathbf{q}} X_{hi,\mathbf{Q}} \end{aligned} \tag{9.18}$$

with exciton tunnelling matrix elements

$$\mathcal{T}^{c}_{ih,jh}(\mathbf{q}) = T^{c}_{ji}(\mathbf{q})\mathcal{F}_{ih,jh}(\beta_{jh}\mathbf{q}) \tag{9.19}$$

$$\mathcal{T}^{v}_{hi,hj}(\mathbf{q}) = T^{v}_{ij}(\mathbf{q})\mathcal{F}_{hi,hj}(-\alpha_{jh}\mathbf{q}) \tag{9.20}$$

$$\mathcal{F}_{ij,nm}(\mathbf{q}) = \sum_{\mathbf{k}} \Psi_{ij}(\mathbf{k})^{*}\Psi_{nm}(\mathbf{k}+\mathbf{q}). \tag{9.21}$$

Hence, we obtain a mixing between excitonic states with different electron/hole layer configurations. Thereby, different exciton states only directly interact via tunneling terms if they either have an electron or a hole within the same layer. Therefore, e.g. two intralayer excitons in different layers would only indirectly interact, by mixing with the same interlayer exciton.

9.2 Mini-Brillouin Zones and Exciton Hybridization

In this section we will discuss the concept of the superlattice and the resulting formation of mini-Brillouin zones (mBZ). Based on the here introduced zone-folding approach we will then show how the excitonic tunneling Hamiltonian can be numerically diagonalized in order to obtain the interlayer hybrid eigenstates.

Moiré Pattern

In the following we discuss the physical interpretation of the derived tunneling matrix element. To this end, we again only consider one band and one valley so that the electronic tunneling Hamiltonian in global coordinates ($\tilde{a}_{l,\mathbf{k}} = a_{l,\mathbf{k}-\zeta}$) reads

$$H_T = \sum_{\mathbf{k},n} \theta^{(n)}_{01}\tilde{a}^{\dagger}_{0,\mathbf{k}+\mathbf{b}_n}\tilde{a}_{1,\mathbf{k}} + \text{h.c.}, \tag{9.22}$$

where only for the K point the sum over n contains three terms and otherwise we set $\theta^{(n)} \propto \delta_{n,0}$. Moreover we have introduced the reciprocal lattice vector of the moiré

$$\mathbf{b}_n = (C_3^n - \mathbb{1})(K_1 - K_0), \tag{9.23}$$

where $K_{0/1}$ represent two neighbouring K points in layer l = 0,1. In real space representation $\tilde{a}_{i\mathbf{k}} = \int d^2r \alpha_i(\mathbf{r})\exp(i\mathbf{k}\mathbf{r})$ the tunneling reads

$$H_T = \int d^2r V_{01}(\mathbf{r})\alpha^{\dagger}_0(\mathbf{r})\alpha_1(\mathbf{r}) + \text{h.c.}, \tag{9.24}$$

$$V_{01}(\mathbf{r}) = \sum_n \theta^{(n)}_{01}\exp(-i\mathbf{b}_n\mathbf{r}) \tag{9.25}$$

with the latter corresponding to a periodic "tunneling potential". This equation illustrates that the mixing of discrete momenta corresponds to the interaction with a spatially periodic potential [130]. Thereby the additional phase modulation given by the symmetry of d-orbitals at the K point (Eq. 9.11) dictates at which local atomic registries the interlayer tunneling is most favourable [130]. The spatial periodicity arises from the moiré pattern created by the overlap of the two twisted K point Bloch waves, containing spatial regions with larger and smaller overlap. In contrast, for electrons at Λ and Γ, we have $\theta^{(n)} \propto \delta_{n,0}$ and since $\mathbf{b}_0 = 0$ the tunneling is spatially independent and there is no mixing of momenta. While this can be explained with the more slowly varying phase factors of their Bloch waves, it is important to note that this is an approximation (Eq. 9.12). If we include terms with $\mathbf{G} \neq 0$ for Λ and Γ point electrons, we would obtain a similar spatial pattern for the tunneling. However, in contrast to the K point, this spatial oscillation would come on top of the constant term, where the latter should be orders of magnitude stronger and is therefore considered as the leading term.

Zone Folding

With the above consideration, it is now clear that the diagonalization of the excitonic Hamiltonian including the tunneling term is equivalent to the problem of finding the eigenstates of a particle in a periodic potential. A well known approach for this kind of problems is the so called zone folding, giving rise to multiple subbands as solutions. For simplicity we only show the details for the tunneling of electrons in the conduction band. The respective hole term can be treated in the same way. First, we rewrite the excitonic tunneling Hamiltonian in order to expose the momentum selection rules. Again we therefore use global coordinates for the center of mass momentum, i.e. $X_{ij,\mathbf{Q}} = \tilde{X}_{ij,\mathbf{Q}+[\zeta_i-\zeta_j]}$ (since $\mathbf{Q} = \mathbf{k}_e - \mathbf{k}_h$). Hence we obtain from Eq. 9.18 together with Eq. 9.19 the expression,

$$H = \sum_{ij\mathbf{Q}} \tilde{E}_{ij\mathbf{Q}} \tilde{X}^\dagger_{ij\mathbf{Q}} \tilde{X}_{ij\mathbf{Q}} + \sum_{n,i\neq j,h,\mathbf{Q}} \Theta^{c,n}_{ih,jh} \tilde{X}^\dagger_{jh,\mathbf{Q}+\mathbf{b}^{ij}_n} \tilde{X}_{ih\mathbf{Q}} + H^{(v)}_T, \tag{9.26}$$

$$\mathbf{b}^{ij}_n = (C^n_3 - \mathbb{1})(K_i - K_j) = (l_i - l_j)\tau_j \mathbf{b}_n \tag{9.27}$$

with the auxiliary definitions $\tilde{E}_{ij\mathbf{Q}} = \hbar^2(\mathbf{Q} - [\zeta_i - \zeta_j])^2/M_{ij} + E_{ij\mathbf{0}}$ and $\Theta^{c,n}_{ih,jh} = \theta^{(n)}_{ji} \mathcal{F}_{ih,jh}(\beta_{jh} C^n_3[\zeta_i - \zeta_j])$. Hence, the conduction band tunneling is mixing excitons with different electron layers and CoM momenta. However, since only discrete momenta are mixed, we can rewrite the equation into a mixing of discrete subbands. To this end, we define a mini Brillouin zone (mBZ) spanned by the fundamental reciprocal lattice vectors of the moiré pattern $\mathbf{g}_1$ and $\mathbf{g}_2$, which are defined slightly different then the before used vectors $\mathbf{b}_n$, but will be more useful later on. We

define,

$$\mathbf{g}_n = C_3^{n-1}(\mathbf{G}_1^{(0)} - \mathbf{G}_0^{(0)}) \tag{9.28}$$

$$\implies \mathbf{b}_1 = \mathbf{g}_1 \quad \text{and} \quad \mathbf{b}_2 = \mathbf{g}_1 + \mathbf{g}_2 \tag{9.29}$$

Figure 9.2 illustrates the definition of the mBZ with respect to the two twisted monolayer Brillouin zones. Based on this definition, we apply a zone folding,

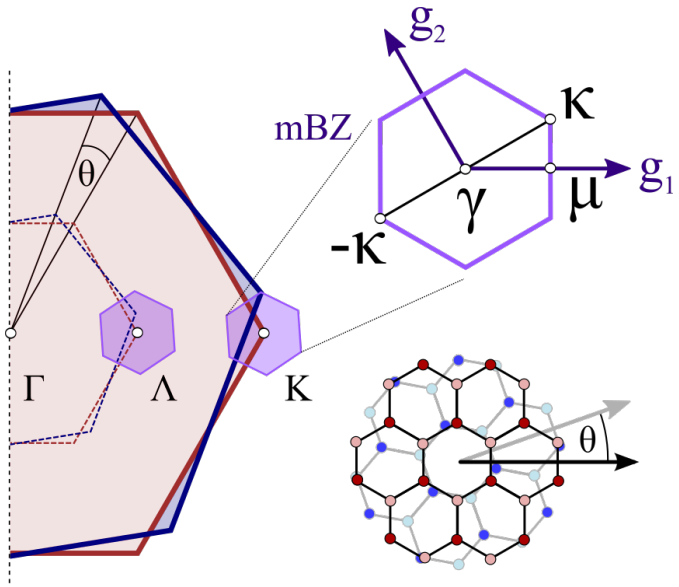

Figure 9.2: Definition of the mini-Brillouin zone (mBZ) and moire vectors $\mathbf{g}_i$. The high-symmetry points of the mBZ are defined analogue to their BZ counterparts but are denoted with small Greek letters. Figure adopted from Paper 4.

meaning that all exciton states with CoM momenta larger then the first mBZ are folded back into it, creating a new subband. According to this scheme, we define zone-folded operators with new compound indices $L = (l_e,l_h)$,$\zeta = (\zeta_e,\zeta_h)$ and $s = (s_1,s_2)$ (with s_i being integers) via

$$F^{\zeta}_{Ls\mathbf{Q}} = \tilde{X}_{l_e\zeta_e l_h\zeta_h,\mathbf{Q}+s_1\mathbf{g}_1+s_2\mathbf{g}_2}, \tag{9.30}$$

where $\mathbf{Q}$ is now restricted to the first mBZ. Thereby each exciton valley $\zeta = (\zeta_e,\zeta_h)$ obtains its own mBZ whose origin is located at the high-symmetry point $\zeta_e - \zeta_h$. Hence, the momentum $\mathbf{Q}$ is limited to small momenta in the vicinity of $\mathbf{Q}_0 = \zeta_e - \zeta_h$ (cf. mBZ around Λ and K within Fig. 9.2). This redefinition yields the convenient form,

$$H = \sum_{L\zeta s\mathbf{Q}} \tilde{E}_{L\zeta,\mathbf{Q}+s_1\mathbf{g}_1+s_2\mathbf{g}_2} F^{\zeta\dagger}_{Ls\mathbf{Q}} F^{\zeta}_{Ls\mathbf{Q}} + \sum_{\zeta LL'ss'\mathbf{Q}} \tilde{\mathcal{T}}^{\zeta}_{Ls,L's'} F^{\zeta\dagger}_{Ls\mathbf{Q}} F^{\zeta}_{L's'\mathbf{Q}} \tag{9.31}$$

$$\text{with} \quad \tilde{\mathcal{T}}^{\zeta}_{Ls,L's'} = \tilde{\mathcal{T}}^{\zeta(c)}_{Ls,L's'} - \tilde{\mathcal{T}}^{\zeta(v)}_{LsL's'} \tag{9.32}$$

$$\begin{aligned}\tilde{\mathcal{T}}^{\zeta(c)}_{Ls,L's'} = \delta(l_h,l'_h)[1-\delta(l_e,l'_e)]\Big[&\Theta^{c,0}_{\zeta,L'L}\delta(s_1,s'_1)\delta(s_2,s'_2) \\ &+ \Theta^{c,1}_{\zeta,L'L}\delta(s_1,s'_1+\tau_e(l'_e-l_e))\delta(s_2,s'_2) \\ &+ \Theta^{c,2}_{\zeta,L'L}\delta(s_1,s'_1+\tau_e(l'_e-l_e))\delta(s_2,s'_2+\tau_e(l'_e-l_e))\Big];\end{aligned} \tag{9.33}$$

$$\begin{aligned}\tilde{\mathcal{T}}^{\zeta(v)}_{Ls,L's'} = \delta(l_e,l'_e)[1-\delta(l_h,l'_h)]\Big[&\Theta^{c,0}_{\zeta,LL'}\delta(s_1,s'_1)\delta(s_2,s'_2) \\ &+ \Theta^{v,1}_{\zeta,LL'}\delta(s_1,s'_1-\tau_h(l'_h-l_h))\delta(s_2,s'_2) \\ &+ \Theta^{v,2}_{\zeta,LL'}\delta(s_1,s'_1-\tau_h(l'_h-l_h))\delta(s_2,s'_2+\tau_h(l'_h-l_h))\Big].\end{aligned} \tag{9.34}$$

The Hamiltonian Eq. 9.31 is now diagonalized via a basis transformation, defining intra-/interlayer hybrid moiré excitons bands η,

$$Y^{\dagger}_{\zeta\eta\mathbf{Q}} = \sum_{sL} C^{\zeta\eta}_{Ls}(\mathbf{Q})^* F^{\zeta\dagger}_{Ls,\mathbf{Q}}, \tag{9.35}$$

with mixing coefficients fulfilling the algebraic eigenvalue problem

$$\tilde{E}_{L\zeta,\mathbf{Q}+s_1\mathbf{g}_1+s_2\mathbf{g}_2} C^{\zeta\eta}_{Ls}(\mathbf{Q}) + \sum_{L's'} \tilde{\mathcal{T}}^{\zeta}_{Ls,L's'} C^{\zeta\eta}_{L's'}(\mathbf{Q}) = \mathcal{E}^{\zeta}_{\eta\mathbf{Q}} C^{\zeta\eta}_{Ls}(\mathbf{Q}), \tag{9.36}$$

$$\sum_{Ls} C^{\zeta\eta_1}_{Ls}(\mathbf{Q})^* C^{\zeta\eta_2}_{Ls}(\mathbf{Q}) = \delta_{\eta_1\eta_2} \tag{9.37}$$

$$\sum_{\eta} C^{\zeta\eta}_{Ls}(\mathbf{Q})^* C^{\zeta\eta}_{L's'}(\mathbf{Q}) = \delta_{LL'}\delta_{ss'} \tag{9.38}$$

which gives rise to the final Hamiltonian

$$H = \sum_{\zeta\eta\mathbf{Q}} \mathcal{E}^{\zeta}_{\eta\mathbf{Q}} Y^{\dagger}_{\zeta\eta\mathbf{Q}} Y_{\zeta\eta\mathbf{Q}}. \tag{9.39}$$

The eigenvalue problem Eq. 9.36 can now be solved numerically for a finite number of subbands, e.g. $s_i = -4, -3, ..., 0, ..., +3, +4$, which usually gives well converged results for twist-angles $> 0.5°$.
The resulting excitons are valley specific superpositions of different electron- and hole layer configurations as well as integer multiples of center-of-mass momenta $\mathbf{Q} + s_1\mathbf{g}_1 + s_2\mathbf{g}_2$, which in real space yields periodically modulated wave functions. This is analogue to the emergence of Bloch waves in a solid, just that the modulation periodicity is here given by the superlattice (moiré pattern). The information about the degree of hybridization of layer and momentum quantum numbers is thereby fully contained by the mixing coefficients $C^{\zeta\eta}_{Ls}(\mathbf{Q})$, which represent the projections of the moiré hybrids on layer localized plane waves.

The band structure of different intervalley excitons in a homobilayer is shown in Sec. 9.4. In the following, we first discuss the impact of the moiré hybridization on the excitons interaction with light and lattice vibrations.

9.3 Interaction Hamiltonians for Hybridized Moiré Excitons

After the above performed basis transformations which has helped to diagonalize H_0 for a twisted bilayer system, we consequently also have to transform the many-particle interaction Hamiltonians such as the exciton-light and exciton-phonon coupling.

Exciton-Photon Coupling

First we consider the exciton-photon coupling (Eq. 5.20), which for the decoupled bilayer system reads (only 1s states),

$$H_{x-pt} = \sum_{\sigma\mathbf{q},\zeta L} \tilde{\mathcal{M}}^{\zeta L}_{\sigma\mathbf{q}} c^\dagger_{\sigma\mathbf{q}} X_{\zeta L,\mathbf{q}_\parallel} + \text{h.c.} \tag{9.40}$$

$$\text{with} \quad \tilde{\mathcal{M}}^{\zeta L}_{\sigma\mathbf{q}} = \delta_{\zeta_e,\zeta_h} \tilde{M}^{\zeta_e l_e l_h}_{\sigma\mathbf{q}} \sum_{\mathbf{k}} \Psi^*_{\zeta L}(\mathbf{k}), \tag{9.41}$$

where we, in addition to the degrees of freedom considered in Sec. 3.2, included a layer index L containing electron and hole position. The oscillator strength of interlayer transitions is extremely low, since the electron and hole are spatially separated. In the following sections we are interested in how the oscillator strength of the bright intralayer exciton is shared with the interlayer excitons. Therefore we simply set $\tilde{M}^{\zeta_e l_e l_h}_{\sigma\mathbf{q}} \propto \delta_{l_e,l_h}$. Now we first apply a zone folding $X \to \tilde{X} \to F$ and

then use the transformation into hybrid states (Eq. 9.35), which yields

$$H_{x-pt} = \sum_{\zeta\eta,\sigma\mathbf{q}} \tilde{m}^{\zeta\eta}_{\sigma\mathbf{q}} c^\dagger_{\sigma\mathbf{q}} Y_{\zeta\eta\mathbf{q}_\parallel} + \text{h.c.} \tag{9.42}$$

$$\text{with} \quad \tilde{m}^{\zeta\eta}_{\sigma\mathbf{q}} = \sum_{Ls} C^{\zeta\eta *}_{Ls}(\mathbf{q}_\parallel) \tilde{\mathcal{M}}^{\zeta L}_{\sigma\mathbf{q}} \delta_{s,0}, \tag{9.43}$$

where we assumed that the momentum of the photon is small compared to moiré vectors $|\mathbf{q}| << |\mathbf{g}_n|$, meaning that the moiré period is small compared to the wavelength, which is even fulfilled for very small twist-angles $< 0.5°$. From Eq. 9.42 we can deduce interesting new features of the hybrid excitons. In the monolayer only intralayer excitons with vanishing CoM momentum couple to light, giving rise to a single excitonic resonance in optical spectra. In contrast, the mixing of different layer configurations and mini-subbands in the case of the moiré hybrid yields a whole series of new resonances η = 0,1,2,... Thereby, the oscillator strength of the hybrid state η depends on its projection onto the original bright state $C^{\zeta\eta *}_{L,s=0}(\mathbf{q}_\parallel \approx 0)$, i.e. on the bright states contribution to the hybrid. From the form of the Hamiltonian (Eq. 9.42) we can read-off the linear optical response of the system (cf. Sec. 4.1). A simple generalization of the previously derived excitonic Elliot formula yields the absorption coefficient,

$$\alpha_\sigma(\omega) \propto \sum_{\zeta\eta} \text{Im}\left(\frac{|\tilde{m}^{\zeta\eta}_\sigma|^2}{\mathcal{E}_{\zeta\eta\mathbf{0}} - \hbar\omega - i\Gamma_{\zeta\eta}} \right), \tag{9.44}$$

where we have introduced the phonon dephasing $\Gamma_{\zeta\eta}$ determining the broadening of excitonic resonances.

Exciton-Phonon Coupling

Next we transform the exciton-phonon coupling into hybrid moiré basis. Starting point is again the simple exciton-phonon Hamiltonian for a decoupled bilayer system. Using a super compound for excitons $\nu = (\zeta_\nu, L_\nu) = (\zeta^e_\nu, \zeta^h_\nu, l^e_\nu, l^h_\nu)$ and for phonons $j = (\kappa_j, \zeta^{ph}_j, l^{ph}_j)$, the Hamiltonian can be expressed as,

$$H_{\text{x-ph}} = \sum_{\mathbf{Q},\mathbf{Q}'\nu\mu j} \mathcal{D}^{\mu\nu}_{j\mathbf{Q}'-\mathbf{Q}} X^\dagger_{\nu\mathbf{Q}'} X_{\mu\mathbf{Q}} b_{j\mathbf{Q}'-\mathbf{Q}} + \text{h.c.}, \tag{9.45}$$

with the generalized matrix element,

$$\begin{aligned} \mathcal{D}^{\mu\nu}_{j\mathbf{q}} = & D^{j,c}_{\zeta^e_\nu\zeta^e_\mu,\mathbf{q}} \delta_{\zeta^h_\nu\zeta^h_\mu} \delta_{\zeta^{\text{ph}}_j,\zeta^e_\nu-\zeta^e_\mu} \delta_{L_\nu,L_\mu} \delta_{l^e,l^{ph}_j} \mathcal{F}^{\mu\nu}(\beta_\nu\mathbf{q}) \\ & - D^{j,v}_{\zeta^h_\mu\zeta^h_\nu,\mathbf{q}} \delta_{\zeta^e_\nu\zeta^e_\mu} \delta_{\zeta^{\text{ph}}_j,\zeta^h_\mu-\zeta^h_\nu} \delta_{L_\nu,L_\mu} \delta_{l^h,l^{ph}_j} \mathcal{F}^{\mu\nu}(-\alpha_\nu\mathbf{q}). \end{aligned} \tag{9.46}$$

The above form of the Hamiltonian contains the restriction discussed in Sec. 8.1, only allowing phonon-guided transitions between electronic states within the same

layer (that of the phonon). It is also important to note that the above equations are defined in valley local coordinates, i.e. the momentum $\mathbf{Q}$ ($\mathbf{q}$) defining the operator $X_{\nu\mathbf{Q}}$ ($b_{j\mathbf{q}}$) is measured with respect to the closest high-symmetry point $\zeta^e_\nu - \zeta^h_\nu$ (ζ^{ph}_j). In order to transform into hybrid basis we again first go to global coordinates $X_{ij,\mathbf{Q}} = \tilde{X}_{ij,\mathbf{Q}+[\zeta_i-\zeta_j]}$ and $b_{j\mathbf{q}} = \tilde{b}_{j\mathbf{q}+\zeta^{ph}_j}$ and then apply the zone folding for excitons (Eq. 9.30), which we also define for phonons

$$\beta^\dagger_{js\mathbf{q}} = \tilde{b}^\dagger_{j\mathbf{q}+s_1\mathbf{g}_1+s_2\mathbf{g}_2}, \tag{9.47}$$

where again, just as for excitons, $\mathbf{q}$ is limited to the first mBZ shifted to ζ^{ph}. With this definition we obtain a convenient form in hybrid basis,

$$H_{\text{x-ph}} = \sum_{\mathbf{Q},\mathbf{Q}'\eta\zeta\eta'\zeta' js^{ph}} \tilde{\mathcal{D}}^{\eta\zeta\eta'\zeta'}_{js^{ph}}(\mathbf{Q},\mathbf{Q}') Y^\dagger_{\eta'\zeta'\mathbf{Q}'} Y_{\eta\zeta\mathbf{Q}} \beta_{js^{ph}\mathbf{Q}'-\mathbf{Q}} + \text{h.c.}, \tag{9.48}$$

$$\begin{aligned}\text{with} \quad \tilde{\mathcal{D}}^{\eta\zeta\eta'\zeta'}_{js^{ph}}(\mathbf{Q},\mathbf{Q}') = \sum_{L,ss'} & \mathcal{D}^{L\zeta,L\zeta'}_{j\mathbf{Q}'-\mathbf{Q}-\zeta^{ph}_j+s^{ph}_1\mathbf{g}_1+s^{ph}_2\mathbf{g}_2} \\ & \times C^{\zeta'\eta'}_{Ls'}(\mathbf{Q}') C^{\zeta\eta}_{Ls}(\mathbf{Q})^* \delta_{s^{ph}_1,s'_1-s_1} \delta_{s^{ph}_2,s'_2-s_2}.\end{aligned} \tag{9.49}$$

The above equation describes scattering between different hybrid moiré minibands in different exciton valleys via absorption/emission of zone-folded phonons. The probability is thereby given by the overlap of initial and final states, which is quantified via the mixing coefficients $C^{\zeta\eta}_{Ls}$. Hence, a transition $\eta \to \eta'$ via a phonon of subband s^{ph} is only allowed, if their constituting subband mixture contains compatible components with $s' = s + s^{ph}$.
Most importantly, the scattering between different hybrid states now also allows excitons to scatter between states with different layer configurations. The probability of such a process is however again limited by the projection of the hybrid states onto a common layer configuration, since the original phonon-scattering was layer conserving. With the above equation, one can now quantify phonon-assisted charge transfer processes, such as the scheme suggested in Ref. [62].
An exciton which is strongly localized in one layer, i.e. a pure intra layer exciton (e.g. K-K), can scatter to a valley which is a 50:50 mixture of intra- and interlayer exciton (e.g. K-Λ). Finally the hybrid exciton scatters back to a pure interlayer exciton e.g. in K-K, so that the electron has effectively moved from one layer to the other, using the layer mixed state as a gateway. As we will show in the next section, the degree of hybridization can be controlled through the twist-angle which potentially enables the external tunability of charge transfer dynamics and other important properties of the bilayer.

9.4 Hybridized Intervalley Excitons in Twisted WSe_2 Bilayers

In the following we discuss the hybridization of different exciton species in a twisted WSe_2 homobilayer, based on the formalism introduced in the last section. In Paper 4 we provide a detailed discussion of the hybridization induced changes in optical properties and compare our results with experiments. Here we just give a short summary of the main results.

Extraction of Tunneling Parameters From ab initio Calculations

Starting point of the theory is the excitonic band structure and corresponding transition matrix elements of two decoupled monolayers, which can host intra- and interlayer excitons as discussed in Sec. 8. In order to obtain a realistic model, which can make quantitative predictions about the degree of hybridization, we need to determine the interlayer tunneling strength θ_0 (Eq. 9.11) for different valleys of valence and conduction band. To this end we consider a homobilayer with zero-twist angle and AA stacking (R_h^h) so that $\Delta m_z = 0$ (difference in magnetic quantum number of d-orbitals),$\mathbf{D} = 0$ (lateral displacement) and the valleys of both layers are at the same position. Hence, Eq. 9.10 reduces to

$$T^{\lambda\zeta}(\mathbf{q}) = T_0^{\lambda\zeta}\delta_{\mathbf{q},0} \quad \text{with} \quad T_0^{\lambda\zeta} = \begin{cases} 3\theta_0^{\lambda,K} & \text{for } \zeta = K \\ \theta_0^{\lambda\zeta} & \text{for } \zeta = \Lambda,\Gamma \end{cases}. \tag{9.50}$$

With this the electronic Hamiltonian (Eq. 9.2) becomes simple,

$$H_0 = \sum_{\lambda\zeta l\mathbf{k}} \varepsilon_{l\mathbf{k}}^{\lambda\zeta} a_{\lambda\zeta l\mathbf{k}}^\dagger a_{\lambda\zeta l\mathbf{k}} + \sum_{\lambda\zeta, l\neq l', \mathbf{k}} T_0^{\lambda\zeta} a_{\lambda\zeta l\mathbf{k}}^\dagger a_{\lambda\zeta l'\mathbf{k}}. \tag{9.51}$$

The eigenenergies of this Hamiltonian can be calculated analytically by diagonalizing a two-by-two matrix (with respect to the layer index) for each fixed valley, band and momentum, which yields the hybrid energies,

$$\mathcal{E}_{\pm,\mathbf{k}}^{\lambda\zeta} = \frac{1}{2}(\varepsilon_{0,\mathbf{k}}^{\lambda\zeta} + \varepsilon_{1,\mathbf{k}}^{\lambda\zeta}) \pm \frac{1}{2}\sqrt{(\varepsilon_{0,\mathbf{k}}^{\lambda\zeta} - \varepsilon_{1,\mathbf{k}}^{\lambda\zeta})^2 + 4|T_0^{\lambda\zeta}|^2}; \tag{9.52}$$

$$= \varepsilon_{0/1,\mathbf{k}}^{\lambda\zeta} \pm T_0^{\lambda\zeta}; \tag{9.53}$$

$$\implies T_0^{\lambda\zeta} = \frac{1}{2}(\mathcal{E}_{+,\mathbf{k}}^{\lambda\zeta} - \mathcal{E}_{-,\mathbf{k}}^{\lambda\zeta}), \tag{9.54}$$

where in the second step we used that the decoupled bands in a homobilayer are degenerate. Hence, the valley and band dependent tunneling parameter can be

extracted from the splitting of bands in a bilayer bandstructure calculated with DFT. Such calculations have been performed by Roland Gillen from the University of Erlangen (coauthor of Paper 4). Details on the ab inito calculations are given in the supplementary of Paper 4. For the following discussion the most important hopping parameters are $\theta_0^{c,\Lambda} \approx 170$ meV and $\theta_0^{c,K} \approx 0.2$ meV. In contrast to the conduction band, there is also a significant hopping for holes at the K-point $\theta_0^{v,K} \approx 10$ meV. These values are comparable to the order of magnitude found for different valleys and bands in MoS_2 bilayer in the important Ref. [62].
The strong difference between values at Λ and K result from the different orbital character of the wave function composing the conduction band states at these high-symmetry points, which are depicted in Fig. 9.3. The conduction and valence band states at K are composed of d orbitals located at metal atoms and are therefore protected from the environment. In contrast, states at Λ have a significant contribution at chalcogen atoms and are therefore subject to much stronger interlayer hybridization.

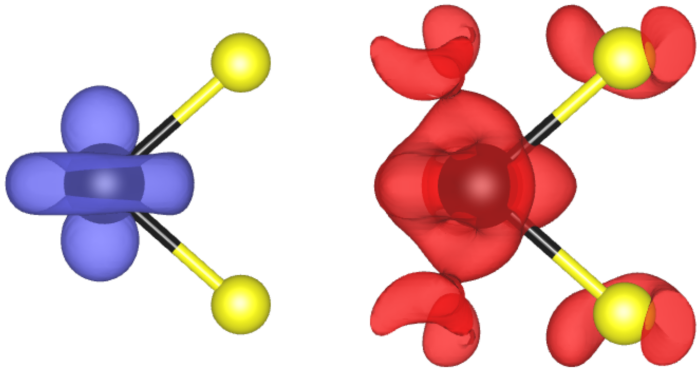

Figure 9.3: Wannier functions composing the bloch waves in the conduction band at K (left) and Λ (right). Figures provided by Roland Gillen (Paper 4).

Exciton Hybridization

With the above material parameters and the microscopic model presented in the last sections, we calculate the excitonic band structure of hybrid moiré excitons in a twisted bilayer.
Figure 9.4 illustrates the calculated exciton CoM dispersion for K-K and K-Λ within their respective mBZ for a twisted WSe_2 bilayer on a SiO_2 substrate. Note that the γ-point of the K-Λ mBZ corresponds to a global momentum of $\mathbf{Q}_0^{K-\Lambda} = \Lambda - K = -\Lambda$. Two representative configurations are demonstrated: Figure 9.4(a) and (b) show K-K and K-Λ dispersions at 2° twist angle (R-type), while (c) and (d) correspond to 58° (H-type). The line colour reflects the projection of the exciton

state onto an intralayer exciton. The colors of the curves indicate the nature of exciton states (red: pure intralayer excitons, blue: pure interlayer exciton) which has been extracted from the mixing coefficients $C_{Ls}^{\zeta\eta}$.

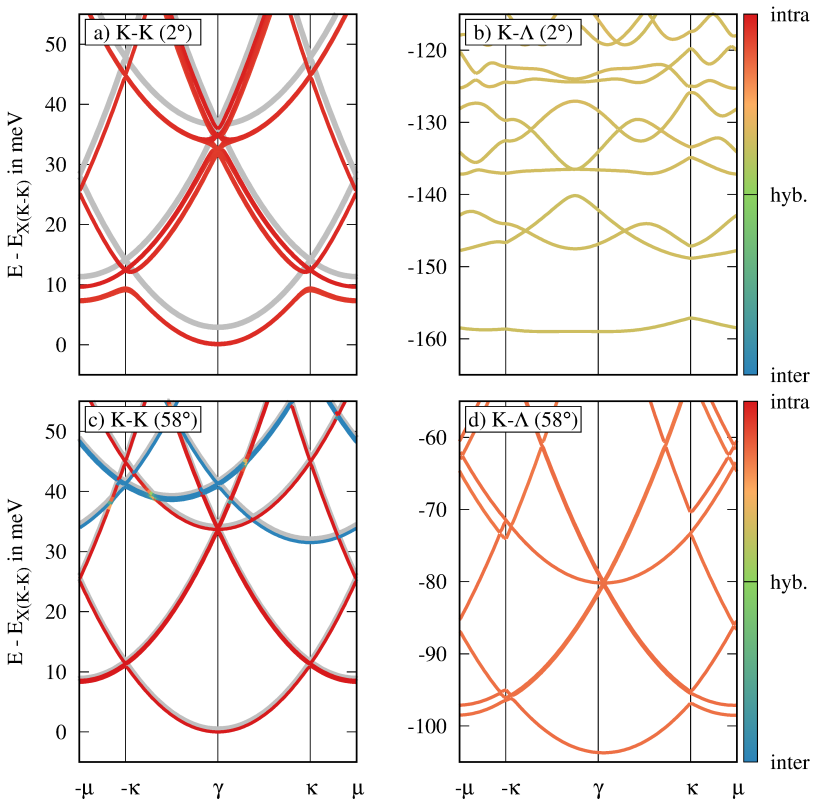

Figure 9.4: Excitonic center-of-mass dispersion for 2° twisted (a)-(b) and 58° twisted (c)-(d) bilayer WSe_2 on SiO_2. For the bright K-K excitons electrons and holes are pinned to one layer (either pure intra-[red] or interlayer states [blue]). The grey lines show the zone folded dispersion without hybridization. For K-Λ [b,d] the large overlap of atomic orbitals gives rise to a strong hybridization [green]. Figure adopted from Paper 4

First we focus on the bright K-K exciton. For both configurations, we find very weak exciton hybridization and the obtained dispersions barely deviate from the decoupled bands (grey lines).

For R-stacking the electronic bands of both layers are initially degenerate, but when accounting for the Coulomb interaction, a significant detuning arises between intra- and interlayer excitons due to their different binding energies (Sec. 8.3). This offset further quenches hybridization which is already weak in the electronic picture due to the small atomic overlaps. For H-stacking, the order of the spin-polarized bands in the two layers is flipped. Therefore, the tunneling in the valence band is completely suppressed due to the large spin-orbit-splitting. Consequently,

even the small red shift observed for R-stacking, vanishes for the H-type bilayer.

Now, we consider the K-Λ excitons, where we find a very strong hybridization of intra- and interlayer states in particular for R-stacking. For the R-type bilayer, the delocalization of electrons across both layers leads to a massive redshift of about 125 meV. In contrast, the splitting of different moiré subbands only results from spatial fluctuation of the tunneling strength and is therefore entirely determined by the tunneling of holes at the K point (T=10 meV), cf. discussion in Sec. 9.2 Including both, electron and hole tunneling, gives rise to an almost flat K-Λ band at approximately 160 meV below the bright K-K exciton. The interpretation of flat bands in the context of excitons is in detail discussed in Sec. 10.3.
Finally, considering H-stacking, both the hybridization and moiré splitting are strongly reduced, which results from the large spin-orbit-splitting in the conduction band at Λ and in the valence band at the K. This creates a large detuning between compatible intra- and interlayer states and quenches the interlayer hopping. However, despite the large detuning, the strong electronic overlap at Λ still yields a significant red-shift of about 100 meV.

Twist-Tunability of Phonon-Sidebands in PL

With the interaction Hamiltonians derived in Sec. 9.3 we can now also calculate the optical response of hybridized moiré excitons. In Paper 4 we discuss the twist-angle dependent modifications of the optical absorption due to the weak interlayer hybridization of the bright K-K exciton. A much more prominent tunability is however observed when considering changes in the PL signal, which also contains features stemming from the phonon-assisted recombination of momentum-dark intervalley states as discussed in Sec. 6.3. With the generic form of exciton-light and exciton-phonon interaction derived for moiré-hybrids in Sec. 9.3, we can generalize the phonon-assisted PL formula Eq. 6.16 in a straightforward way and can calculate the PL of the twisted homobilayer (cf. Paper 4).

Figure 9.5 shows the twist-angle dependent PL of the above discussed bilayer system. The band gap at the K point has been adjusted to match the peak position of the bright exciton in the experiment (cf. Paper 4). Both for R- and H-type stacking, there are two distinct PL features. Thereby the bright K-K resonance (around 1.7 eV) is independent of the twist angle due to a negligible hybridization.

In contrast, the lower peak is a result of the phonon-assisted recombination of the K-Λ exciton and exhibits a large twist angle-dependent shift of about 50 meV, reflecting the tunability of the hybridization.

Within our microscopic model, there are two aspects leading to a decreased hy-

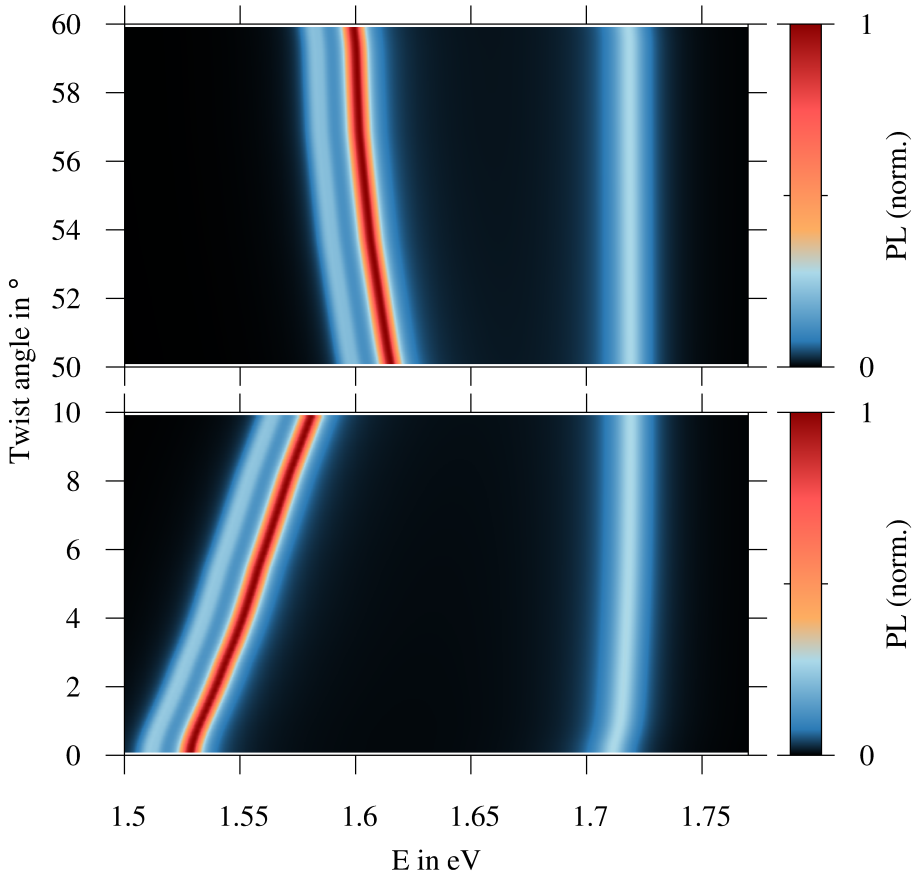

Figure 9.5: PL spectra of twisted WSe_2 on SiO_2 calculated at small twist-angles for H-type (top) and R-type stacking (bottom) at T=4 K. Figure adopted from Paper 4

bridization with increasing stacking angles (with respect to commensurate alignment at 0 and 60°) and the accompanied blue-shift. The twist angle controls the relative rotation of the monolayer Brillouin zones, so that a growing angle corresponds to an increased momentum shift between the high-symmetry points/exciton dispersions. That in turn results in (i) an enhanced detuning between intra- and interlayer states at the γ point of the mBZ, and (ii) a decreasing exciton tunnel matrix element due to a decreased overlap of excitonic wave functions (form factor $\mathcal{F}$ in Eq. 9.19). Finally, we again observe significant difference between the R- and H-type stacking. As discussed Fig. 9.4 above this asymmetry results of the reversed order of spin-polarized states in the H-type bilayer, which creates a large detuning and suppresses hybridization.

In Paper 4 we further show that the emergence of moiré minibands under specific conditions can lead to additional phonon-side peaks stemming from higher order moiré bands. Moreover, the flatness of the K-Λ ground state should be reflected in a different temperature-induced broadening behavior of the phonon-side band at

small angles (where flat bands occur) compared to larger angles (where excitons can occupy a continuous density of states).

CHAPTER 10

MOIRÉ LOCALIZATION IN TWISTED HETEROBILAYERS

The exciton hybridization in homobilayers discussed in the previous chapter is representing an interesting platform to tailor the properties of quasi particles and certainly has a large potential to be exploited in new technological concepts. However, most current optoelectronic device components are based on heterojunctions between two different semiconducting materials, which created a built-in field that can be utilized for many applications. Such an internal bias can also be created in TMD bilayers, by stacking two different monolayers on top of each other. Such a heterobilayer can exhibit a staggered (type II) band alignment, where electron and hole have their energetic minima in different layers, cf. Fig. 10.1. There-

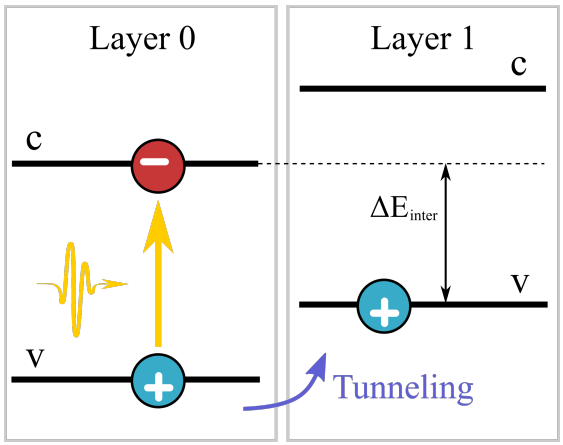

Figure 10.1: Schematic illustration of the type II band alignment and the charge separation after optical excitation.

fore, electron-hole pairs generated in one layer (intralayer exciton) can relax into a charge separated state (interlayer exciton), which is energetically more favourable due to the reduced interlayer band gap.

In Paper 18 we have investigated such a charge transfer process combining our microscopic model with mid-infrared pump probe experiments, revealing tunneling timescales in the picosecond range by observing an ultrafast shift of the 1s-2p resonance from intra- to interlayer exciton binding energies. A large number of pioneering studies [25–27, 131] have demonstrated that TMD heterostructures host interlayer excitons as the ground state for electron-hole pairs. Due to their spatially indirect character, the recombination rate of interlayer excitons is by orders of magnitude smaller compared to direct intralayer states, which makes them technologically highly relevant for information storage and energy harvesting technologies.

Recent experiments [31–35] and theoretical works [30, 132, 133] have studied artificial moiré superlattices created by vertical stacks of two different monolayers and showed that exciton features in optical spectra can be modified through the stacking angle. Theoretical studies on homo- [62] and heterobilayers with resonant band alignment [130] have shown that the twist-tunability can be attributed to the stacking-dependent hybridization of intra- and interlayer excitons discussed in Sec 9.

However, ab initio studies on heterostructures with a large band-offset, such as the type II aligned $MoSe_2/WSe_2$, show that the interlayer hybridization at the K point is negligible [134, 135]. Nevertheless, a spatially varying electronic bandgap [132, 136, 137] is still observed in these systems. Consequently, non-hybridized intra- and interlayer excitons can experience a moiré periodic potential, which similar to the case discussed for homobilayers in Sec. 9 can be exploited to manipulate exciton properties. In particular, it was suggested that the moiré potential can be exploited to create tunable quantum emitter arrays [30] or enable exotic transport properties [133].

In this section we present a theoretical model for pure intra- or interlayer moiré excitons and their optical properties. We thereby focus excitons at the K point, where hybridization was already weak for homobilayers, but will be even further suppressed by the band-offset in a hetero bilayer.

10.1 Interlayer Moiré Potential

In the following, we derive a microscopic model for the electrostatic potential experienced by electrons in one layer due to the presence of the second layer. In Sec.

9.1 we have already introduced the single particle Hamiltonian H_0 of a bilayer projected on to the subspace of the monolayer eigenstates (Eq. 9.2). Thereby we identified two terms $H_T + H_M$ that introduce modifications to the simplified system of two decoupled monolayers. While the tunneling/hybridization (H_T) is important when the electronic bands in both layers are close in energy, this term will be weak for systems with large band offset, such as type II heterostructures and/or for electronic valleys with protected orbitals such as the K point. Nonetheless, a significant stacking dependent energy variation was observed also in these systems, so that we now want to focus on the second Term H_M. Apart from a wave function overlap, the stacking of two layers also leads to an additional electrostatic potential in layer l created by the electrical field of the nuclei of the other layer $1-l$, reading,

$$H_M = \sum_{\lambda l \mathbf{k}\mathbf{q}} \mathcal{V}_l^{\lambda}(\mathbf{q},\mathbf{k}) a^{\dagger}_{\lambda l \mathbf{k}+\mathbf{q}} a_{\lambda l \mathbf{k}};$$
$$\text{with} \qquad \mathcal{V}_l^{\lambda}(\mathbf{q},\mathbf{k}) = \langle \lambda l \mathbf{k}+\mathbf{q} | V_{1-l} | \lambda l \mathbf{k} \rangle. \tag{10.1}$$

In the following we suppress the band index λ for simplicity and write $\neg l = 1-l$. Since we want to extract the stacking dependence of this potential, which we will from now on call "moiré potential", we need to introduce the two lattice geometries. To this end we write the effective lattice potentials as sum of its atomic contributions v_l,

$$V_l(\mathbf{r}) = \sum_{\mathbf{R}_l} v_l(\mathbf{r}-\mathbf{R}_l). \tag{10.2}$$

Together with the tight-binding expansion in Eq. 9.5, we thus find

$$\mathcal{V}_l(\mathbf{q}) = \sum_{\mathbf{G}_l,\mathbf{G}_{\neg l}} m_l(\mathbf{G}_{\neg l}) e^{i(\mathbf{G}_l+\mathbf{G}_{\neg l})\mathbf{D}_l/2} \delta_{\mathbf{q},\mathbf{G}_{\neg l}-\mathbf{G}_l} \tag{10.3}$$

with the atomic interaction energy $m_l(\mathbf{q}) = 1/A_{UC} \int dz \tilde{\rho}_l(-\mathbf{q},z)\tilde{v}_l(\mathbf{q},z)$ using the charge density $\rho_l(\mathbf{r}) = |\Phi_l(\mathbf{r})|^2$ and the in-plane Fourier transformation $\tilde{f}(\mathbf{q},z) = \int d^2r_{\parallel} f(\mathbf{r}) e^{i\mathbf{q}\mathbf{r}_{\parallel}}$. The displacement vector $\mathbf{D}_l$ has already been introduced in Sec. 9.1.

Now we assume that the effective atomic potentials v_l in the neighbouring layer appear as long-ranged potential, as the interlayer forces are of van der Waals type. Therefore, the interaction length is large compared to the unit cell a_0 and the potential in momentum space decays quickly compared to $\mathbf{G} \propto 1/a_0$. Therefore, we can again restrict the $\mathbf{G}$-sum in Eq. (10.3) to the first shell. Thereby terms with $\mathbf{G}_l = \mathbf{G}_{\neg l} = 0$ lead to stacking-independent (hence spatially constant) band shifts. Since we are interested in the spatially varying ($\mathbf{q}$-dependent) moiré potential, we disregard the constant $\mathbf{G} = 0$ terms and attribute them to the band alignment terms $\varepsilon^{\lambda}_{l\zeta 0}$ of the two monolayer bandstructures (Eq. 8.1). The remaining sum over the six $\mathbf{G}$-vectors of the first shell $C_6^n \mathbf{G}^0$ ($n = 0,1,..5$) is split into two parts,

where one is summing over $C_3^n\mathbf{G}^0$ ($n = 0,1,2$) and the others corresponding to the hermitian conjugated Hamiltonian.

Moreover, in order to extract the rotational symmetries of the atomic potential, we decompose it into parts stemming from metal- or chalcogen atoms,

$$v_l(\mathbf{r}) = v_l^M(\mathbf{r}) + v_l^X(\mathbf{r} - \mathbf{b}_l), \tag{10.4}$$

with $\mathbf{b}_l$ being the next neighbour vector of the hexagonal atomic lattice. Here we define the direction of $\mathbf{b}_l$ according to the choice of $\mathbf{G}_l^0$ such that $\mathbf{G}_l^0 \cdot \mathbf{b}_l = 4\pi/3\sigma_l$, where $\sigma_l = 1$ for R-type stacking (both layers have same orientation) and $\sigma_l = (-1)^l$ for H-type stacking ($l = 1$ is mirrored/180° rotated). Finally, we exploit the C_3 invariance of the M/X orbitals and atomic potentials in the hexagonal lattice, which yields

$$H_M = \sum_{l\mathbf{kq}} \mathcal{V}_l(\mathbf{q}) a^\dagger_{l\mathbf{k}+\mathbf{q}} a_{l\mathbf{k}} + \text{h.c.}, \tag{10.5}$$

$$\mathcal{V}_l(\mathbf{q}) = v_l \sum_{n=0}^{2} e^{iC_3{}^n(\mathbf{G}_l^{(0)} + \mathbf{G}_{\neg l}^{(0)})\cdot \mathbf{D}_l/2} \delta_{\mathbf{q}, C_3{}^n(\mathbf{G}_{\neg l}^{(0)} - \mathbf{G}_l^{(0)})}, \tag{10.6}$$

$$v_l = \alpha_l + e^{2\pi i \sigma_{\neg l}/3}\beta_l \tag{10.7}$$

Hence, the potential is characterized by the two real parameters α_l and β_l, given by the interaction energy of the K-point orbitals in one layer with the effective potential of metal- (α) and chalcogen-atoms (β) of the other layer, respectively. Interestingly, for the tunneling Hamiltonian, the strength was parametrized with a single number characterizing the hopping probability between orbitals in different layers. Here we need at least two parameters, since the metal- and chalcogen-atoms can create different potentials in the adjacent layer. Apart from that we find the same spatial geometry as for the tunneling matrix element in Sec. 9.1, quantified by the moiré lattice vectors $\mathbf{g}_n = C_3^{n-1}(\mathbf{G}_1^{(0)} - \mathbf{G}_0^{(0)})$, whose real space counterparts coincide with the fundamental translations of the super lattice.

The parameters α and β can again be obtained from first principle calculations, similar to the tunnelling strength. Assuming a twist-angle of 0° and neglecting the small missmatch between lattice constants of different TMDs, the moiré potential collapses into rigid band shift,

$$H_M\big|_{0^\circ} = \sum_{l\mathbf{k}} \varepsilon_l^{\text{ren}} a^\dagger_{l\mathbf{k}} a_{l\mathbf{k}} \tag{10.8}$$

$$\text{with} \quad \varepsilon_l^{\text{ren}} = 2\text{Re}\{(\alpha_l + e^{2\pi i\sigma_{\neg l}/3}\beta_l) \sum_{n=0}^{2} e^{i[C_3{}^n\mathbf{G}^0].\mathbf{D}_l}\} \tag{10.9}$$

Hence, the band shift depends on the lateral displacement of the two layers. Therefore, the three parameters α_l, β_l and the stacking independent alignment ε_{l0} can be obtained extracted from ab initio calculations, by calculating the respective band edge energies for three different stackings. Here, it is convenient to use high-symmetry stackings such as R_h^h ($\mathbf{D}_l = 0$),R_h^M ($\mathbf{D}_l = \pm\mathbf{b}_0$) and R_h^X ($\mathbf{D}_l = \pm 2\mathbf{b}_0$). Knowing these three energies, the above mentioned three parameters can be obtained by solving the system of three linear equations $E_{\mathrm{DFT}}(\mathbf{D}) = \varepsilon_0 + \varepsilon^{\mathrm{ren}}(\alpha,\beta,\mathbf{D})$. In Paper 5 this procedure was applied to the $MoSe_2/WSe_2$ heterostructure using the GW corrected DFT calculations performed by Christopher Linderälv. The obtained band edge energies and extracted parameters are given in the supplementary of Paper 5.

The obtained moiré values are consistent with the microscopic interpretation of the parameters derived above. In particular, we obtained larger values for the valence band, which can be explained by the larger extension of the valence band orbitals in z-direction, which already gave rise to larger tunneling rates in Sec. 9.4. Moreover, α values are consistently larger than β values, which is consistent with the larger partial charge of metal atoms in the in-plane ionic bond between metal and chalcogen-atoms. Finally, there are larger differences for α values comparing different layer, e.g. in the two valence bands, than for the β values, which is reflecting the fact that both layers have the same chalcogen, but different metal atoms. Figure 10.2a shows the bandgap differences between high-symmetry stackings obtained from DFT+GW calculations next to the fitted microscopic model. The calculated shifts agree with values reported in Ref. [135] and our model reproduces the functional dependence by fixing only two numbers per band.

The benefit of the microscopic model is that we now have a simple analytical expression predicting the moiré potential in a twisted system. Figure 10.2b shows a map of the interlayer bandgap throughout the moiré supercell (R-type), where $\mathbf{a}_i$ are lattice vectors of the supercell ($\mathbf{g}_i \cdot \mathbf{a}_j = 2\pi\delta_{ij}$. Based on this analytical model, we can now study exciton properties in the moiré potential of a twisted heterostructure.

10.2 Moiré Exciton Transformation

In the next step we want to determine the intra- and interlayer exciton eigenstates in the electrostatic potentials created by the moiré pattern. Thereby, the form of the moiré Hamiltonian Eq. 10.3 is analogous to the tunneling Hamiltonian Eq. 9.3, just that the moiré potential only mixes different momenta, while the interlayer hopping additionally changed the layer index. Therefore we can apply the same procedure as described in Sec. 9.2, but only have to consider one possible layer configuration at a time. First, we transform the electronic moiré Hamiltonian into

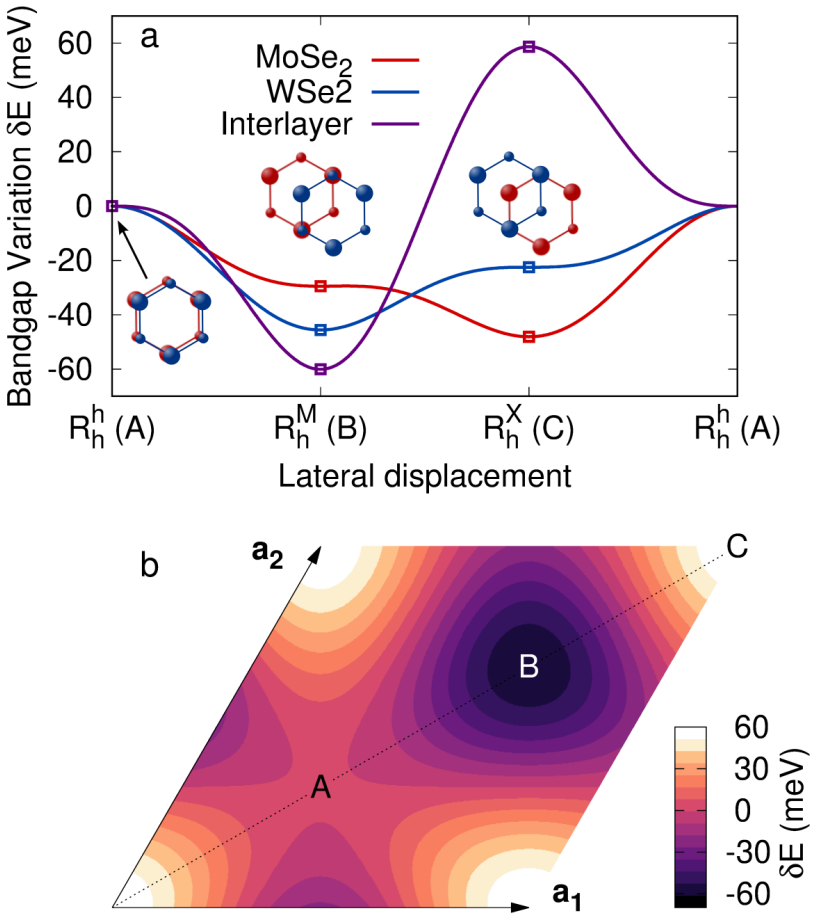

Figure 10.2: Moiré potential in the $MoSe_2/WSe_2$ heterostructure. **a** Bandgap changes of the two intralayer excitons at K (red and blue) and the lower interlayer transition (purple) for different lateral shift **D**. Dots show DFT+ G_0W_0 results, while lines show the microscopic model with extracted parameters. **b** Spatial map of the interlayer bandgap in a twisted heterostructure, where $\mathbf{a}_i$ are the two fundamental translations of the moiré superlattice. Figure adopted from Paper 5.

exciton basis, via the expansion Eq. 9.14 and restrict the exciton basis to the 1s ground state, which yields,

$$H_M = \sum_{ll'\mathbf{Q},\mathbf{q}} \mathcal{M}^{ll'}_{\mathbf{q}} X^{\dagger}_{ll'\mathbf{Q}+\mathbf{q}} X_{ll'\mathbf{Q}} \tag{10.10}$$

$$\text{with} \quad \mathcal{M}^{ll'}_{\mathbf{q}} = \mathcal{V}^{c}_{l}(\mathbf{q})\mathcal{F}_{ll'}(\beta_{ll'}\mathbf{q}) - \mathcal{V}^{v}_{l'}(\mathbf{q})\mathcal{F}^{*}_{ll'}(\alpha_{ll'}\mathbf{q}). \tag{10.11}$$

In order to interpret this effective excitonic potential it is useful to change into a real space representation of the CoM motion $\mathbf{Q} \to \mathbf{R}$ and the relative electron hole motion $\mathbf{k} \to \mathbf{r}$ via a Fourier transformation. In real space, the potential acting on the CoM coordinate of the exciton reads

$$\mathcal{M}^{\mu}(\mathbf{R}) = \int d^2r [V^c(\mathbf{R}+\beta\mathbf{r}) - V^v(\mathbf{R}-\alpha\mathbf{r})]|\Psi_\mu(\mathbf{r})|^2. \tag{10.12}$$

Hence, the excitonic potential is given by the difference of effective electron and effective hole potential. Since the bound electron is smeared out throughout the excitonic orbital, the effective electronic potential is thereby given by a weighted average over all possible electron positions $\mathbf{R}+\beta\mathbf{r}$ whose probabilities are given by the wave function $\Psi_\mu(\mathbf{r})$. When the moiré potential varies slowly on the lengthscale of the excitonic Bohr radius, the effective excitonic potential is simply given by the fluctuations of the band gap $\mathcal{M}(\mathbf{R}) \approx V^c(\mathbf{R}) - V^v(\mathbf{R})$. However, for shorter moiré period (large twist-angles) in a smaller range as the exciton Bohr radius, the exciton does not interact with the potential like a point particle anymore but the effective excitonic potential is then a weighted average of the potential landscape occupied by the exciton. This analysis does not only apply to the moiré potential but to all excitonic interaction mechanisms, which is reflected by the recurring presence of the exciton form factors $\mathcal{F}$.

Next we diagonalize $H_0 + H_M$ to obtain eigenenergies and CoM wavefunctions in the moiré potential. Here we again rewrite the Hamiltonian in order to expose the momentum selection rules ($L = (l_e,l_h)$),

$$H_M = \sum_{L\mathbf{Q},n} \Xi_L X^\dagger_{L\mathbf{Q}+(-1)^{l_e}\mathbf{g}_n} X_{L\mathbf{Q}} \tag{10.13}$$

$$\Xi_L = \begin{cases} v^c_{l_e}\mathcal{F}_L(\beta_L\mathbf{g}_0) - v^v_{l_h}\mathcal{F}_L(\alpha_L\mathbf{g}_0) & \text{for } l_e = l_h \\ v^c_{l_e}\mathcal{F}_L(\beta_L\mathbf{g}_0) - v^{v*}_{l_h}\mathcal{F}_L(\alpha_L\mathbf{g}_0) & \text{for } l_e \neq l_h \end{cases}, \tag{10.14}$$

where we have set $\mathbf{D} = 0$ (without loss of generality) and exploited the isotropy of the excitonic wave functions. Now we can again apply the zone folding scheme Eq. 9.30, which yields the simple form

$$H = \sum_{Ls\mathbf{Q}} \tilde{E}_{L,\mathbf{Q}+s_1\mathbf{g}_1+s_2\mathbf{g}_2} F^\dagger_{Ls\mathbf{Q}} F_{Ls\mathbf{Q}} + \sum_{Lss'\mathbf{Q}} \tilde{\mathcal{M}}^L_{ss'} F^\dagger_{Ls\mathbf{Q}} F^\zeta_{Ls'\mathbf{Q}}, \tag{10.15}$$

with the moiré mixing matrix,

$$\begin{aligned} \tilde{\mathcal{M}}^L_{ss'} = \Xi_L \Big(& \delta(s_1,s'_1+(-1)^{l_e})\delta(s_2,s'_2) + \delta(s_1,s'_1)\delta(s_2,s'_2+(-1)^{l_e}) \\ & + \delta(s_1,s'_1+(-1)^{l_e})\delta(s_2,s'_2+(-1)^{l_e}) \Big) \\ & + \Xi^*_L \Big(\delta(s_1,s'_1-(-1)^{l_e})\delta(s_2,s'_2) + \delta(s_1,s'_1)\delta(s_2,s'_2-(-1)^{l_e}) \\ & + \delta(s_1,s'_1-(-1)^{l_e})\delta(s_2,s'_2-(-1)^{l_e}) \Big). \end{aligned} \tag{10.16}$$

Hence the Hamiltonian is diagonal for the moiré excitons,

$$Y^{\dagger}_{L\eta\mathbf{Q}} = \sum_{s} C^{\eta}_{Ls}(\mathbf{Q})^{*} F^{\dagger}_{Ls\mathbf{Q}}, \tag{10.17}$$

when the momentum mixing coefficients fulfill the eigenvalue equation

$$\tilde{E}_{L,\mathbf{Q}+s_1\mathbf{g}_1+s_2\mathbf{g}_2} C^{\eta}_{Ls}(\mathbf{Q}) + \sum_{s'} \tilde{\mathcal{M}}^{L}_{ss'} C^{\eta}_{Ls'}(\mathbf{Q}) = \mathcal{E}_{L\eta\mathbf{Q}} C^{\eta}_{Ls}(\mathbf{Q}), \tag{10.18}$$

which gives rise to the final Hamiltonian

$$H = \sum_{L\eta\mathbf{Q}} \mathcal{E}_{L\eta\mathbf{Q}} Y^{\dagger}_{L\eta\mathbf{Q}} Y_{L\eta\mathbf{Q}}. \tag{10.19}$$

The above procedure is completely analogue to the hybridization problem, just that we do not have to take care of the layer mixing, so that L is just a parameter in all equations. Although it was not necessary to transform into a global momentum coordinate system in the above problem, it is still a useful step, since now the γ point of the mBZ is the same physical momentum for intra- and interlayer excitons that coincides with the light cone.

The eigenvalue problem Eq. 10.18 is now solved numerically, where we consider the 225 lowest subbands (s_1,$s_2 \in [-7:7]$). This provides converged results and a good spatial resolution for the CoM wave function (cf. Sec. 10.3). Figure 10.3 illustrates the calculated band structure for an hBN encapsulated twisted $MoSe_2/WSe_2$ bilayer based on the moiré potentials shown in Sec. 10.1. As characteristic examples we have chosen the $MoSe_2$ intralayer exciton and the lowest interlayer exciton for 1° and 3°. For 1° twist-angle, there are flat exciton bands for both exciton species. As we will show in Sec. 10.3 these states correspond to moiré-trapped, localized states, which is directly reflected by the vanishing group velocity $\propto \nabla_{\mathbf{Q}} \mathcal{E}_{L\eta\mathbf{Q}}$. The deeper interlayer moiré potential (Fig. 10.2) yields several flat bands, while for the intralayer exciton only the ground state is localized and the excited states have a dispersion and can therefore move through the crystal. These dispersed moiré bands correspond to scattering states of the moiré potential, i.e. free exciton Bloch waves with a moiré-periodic amplitude modulation. For 3°, all moiré-bands are delocalized and exhibit a parabolic dispersion close to the unperturbed exciton. This is a result of the decreasing size of the moiré supercell with increasing twist angle. That corresponds to a smaller confinement length, which enhances the kinetic energy of the ground state (zero-point energy). The latter increases with the twist angle up to a point where the exciton has enough energy to hop between neighboring moiré supercells. Moreover, the dispersion at 3° contains gaps at intersections of the zone-folded branches. This effect can in real space be interpreted as the emergence of standing waves, resulting from the Bragg reflection of the exciton at the moiré pattern. Here the lowest interlayer exciton at the γ point is a standing wave at B sites, while the second state has the largest probability at A sites.

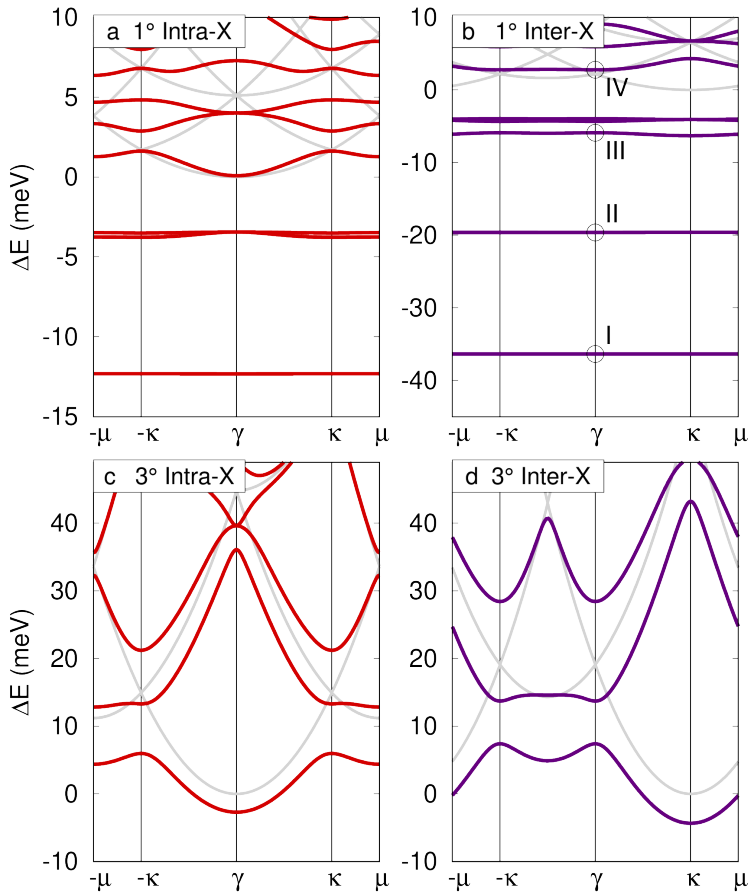

Figure 10.3: Exciton moiré bands for a twisted $MoSe_2/WSe_2$ bilayer encapsulated in hBN. a) and b) contain intra-($MoSe_2$) and interlayer exciton for 1°, c) and d) show the bands at 3°. For 1° both excitons exhibit flat bands, while for the larger twist-angle the dispersion is close to the unperturbed parabolic bands (gray curves). Figure adopted from Paper 5.

To summarize, we find that the CoM wavefunction and thereby the transport properties of the exciton is very sensitive to the twist-angle of the TMD heterostructures. An angle difference of just 2° can induce a transition from localized to free moiré excitons.

10.3 Optical Moiré Resonances

As already shown in Sec. 9.3, the mixing of CoM momenta gives rise to modified optical selection rules for excitons in a moiré potential. In particular, we found that each moiré subband can obtain a finite oscillator strength, while for the unperturbed exciton only the $\mathbf{Q} = 0$ state gives rise to a single peak.

Selection Rules

In Sec. 9.3 we have neglected the oscillator strength of the interlayer exciton, since we where focusing on the hybridization and the connected redistribution of the intralayer excitons dipole moment. However, in the type II heterostructure considered in this section hybridization is weak and we need to consider the interlayer excitons own dipole strength and optical selection rules.

To this end, we generalize the derivation of the optical matrix element for interband transitions within a single layer (Sec. 3.2). When considering that the high-symmetry point of initial and final state can be different, Eq. 3.7 becomes,

$$\mathbf{M}^{cv}_{ll'}(\mathbf{q}) = \frac{\sqrt{2}}{3} M^0_{ll'} \sum_{n=0}^{2} \frac{C_3^n \mathbf{K}_l}{|\mathbf{K}_l|} e^{-i2\pi n \tau_{l'}/3} \delta_{\mathbf{q}, C_3^n(\mathbf{K}_{l'} - \mathbf{K}_l)}, \tag{10.20}$$

which for $l = l'$ gives the same result as for the monolayer, but represents a broken circular dichroism for the interlayer exciton, resulting from the broken C_3 symmetry [137, 138].

Now we transform the semi-classical exciton-light coupling (vector-potential components A_σ),

$$H_{\text{x-l}} = \sum_{\sigma l l' \mathbf{Q}} \Omega_{\sigma l l'}(\mathbf{Q}) A_\sigma(t) X^\dagger_{l l' \mathbf{Q}} + \text{h.c.} \tag{10.21}$$

with $\Omega_{\sigma l l'}(\mathbf{Q}) = \frac{e_0}{m_0} \mathbf{M}^{cv}_{ll'}(\mathbf{Q}) \mathbf{e}_\sigma \sum_{\mathbf{k}} \Psi_{ll'}(\mathbf{k})$, into moiré exciton basis. With the

transformation rules discussed in Sec. 10.2 we find,

$$H_{\text{mX-l}} = \sum_{\sigma\eta} \tilde{\Omega}_{\sigma}^{L\eta} A_{\sigma}(t) Y_{L\eta\mathbf{0}}^{\dagger} + \text{h.c.} \tag{10.22}$$

$$\text{with} \quad \tilde{\Omega}_{\sigma}^{L\eta} = \sum_{s} \mathcal{C}_{Ls}^{\eta}(\mathbf{Q}=0)\Omega_{\sigma L}(s_1\mathbf{g}_1 + s_2\mathbf{g}_2 - K_l + K_l') \tag{10.23}$$

Using Eq. (10.22) we can directly deduce the absorption spectrum of moiré excitons for σ-polarized light via the Elliot formula (Eq. 9.44), which again yields a series of Lorentzian resonances at energies $\mathcal{E}_{L\eta,\mathbf{Q}=\mathbf{0}}$ and oscillator strength $|\tilde{\Omega}_{\sigma}^{L\eta}|^2$.

In order to interpret the above result, it is useful to represent the exciton CoM wave function and optical matrix element in terms of the real space (CoM) coordinate $\mathbf{R}$. Recalling that the CoM wave function of the unperturbed exciton is given by a plane wave with momentum $\mathbf{Q}$, the moiré wave function can be written as,

$$\begin{aligned} \Psi_{\mathbf{Q}}^{\eta}(\mathbf{R}) &= \frac{1}{\sqrt{A}} \sum_{s} \mathcal{C}_{s}^{\eta}(\mathbf{Q}) e^{i(s_1\mathbf{g}_1 + s_2\mathbf{g}_2 + \mathbf{Q})\mathbf{R}} \\ &= \chi_{\mathbf{Q}}^{\eta}(\mathbf{R}) e^{i\mathbf{Q}\mathbf{R}}, \end{aligned} \tag{10.24}$$

where $\chi_{\mathbf{Q}}^{\eta}$ is the moiré-periodic envelope, analogue to the Bloch function. With this transformation and the completeness/orthogonality of the mixing coefficients, we can write the moiré oscillator strength as a spatial overlap integral

$$\tilde{\Omega}_{\sigma}^{L\eta} = \int d^2R \chi_{\mathbf{0}}^{\eta}(\mathbf{R}) \Omega_{\sigma L}(\mathbf{R}) \tag{10.25}$$

$$\text{with} \quad \Omega_{\sigma L}(\mathbf{R}) = \frac{1}{\sqrt{A}} \sum_{\mathbf{q}} \Omega_{\sigma L}(\mathbf{q}) e^{-i\mathbf{q}\mathbf{R}}. \tag{10.26}$$

Hence, the mixing of momenta can be interpreted as a spatial wave function modulation and the $\mathbf{q}$-dependent matrix element corresponds to locally varying optcial selection rules. The latter can be well understood by the spatially varying atomic registry and the connected changes in transition symmetries [27]. It is important to note that the intralayer excitons optical matrix element is not $\mathbf{q}$-dependent and therefore the optical selection rules are constant, reflecting the circular dichroism (Eq. 3.9). We now evaluate the above equations in order to analyse the optical selection rules of moiré excitons for the system discussed in the last sections.

In Fig. 10.4 we show the optical matrix element for the interlayer recombination along with the exciton CoM wave function at 1° for states I–IV defined in Fig. 10.3.

We find that coupling to σ_+ light is strongest at A sites (cf. Fig. 10.2), while it vanishes at B sites, and the inverse is true for the other polarization, which has

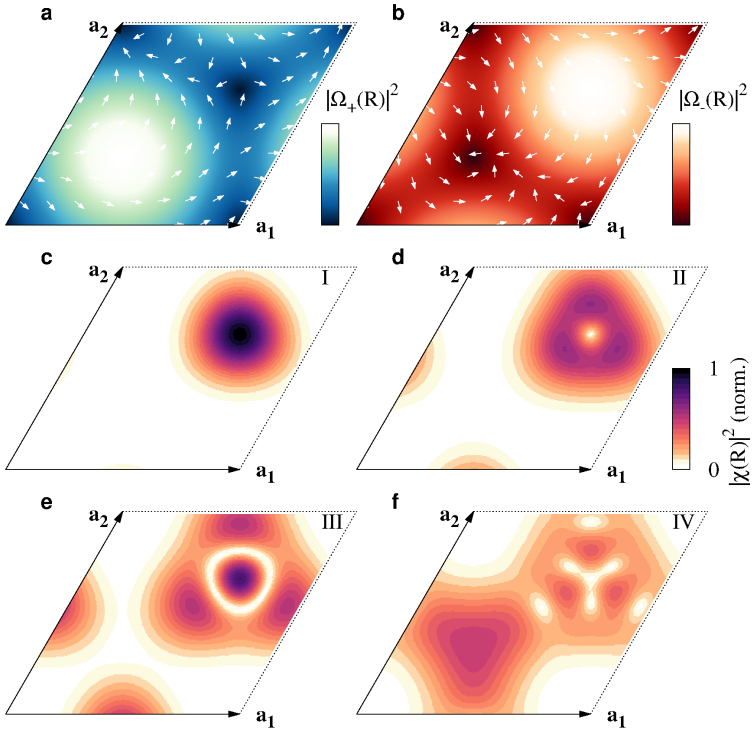

Figure 10.4: **a** and **b** Spatial distribution of the optical matrix element for σ_+ and σ_- polarized light. The superimposed vector field show the complex phase of the dipole matrix element. **c-f** Exciton center-of-mass wave functions for the states I–IV denoted in Fig. 10.3. Figure adopted from Paper 5.

already been predicted in Refs. [30, 137, 138]. This new "spatial dichroism" now has important consequences on the optical selection rules of moiré resonances.

We find that the CoM wave functions for states I–III are concentrated at the minimum of the moiré potential (B site), whereas IV is spread over the whole crystal, but has its largest amplitude at A sites. The overlap between wave functions and the spatial distribution of oscillator strength already indicates that the peaks of state I, III (σ_-) and IV (σ_+) will have different polarizations.

Moreover, we find that state II has p-type symmetry, which should result in a vanishing oscillator strength, because of the angular momentum (phase $\exp i\phi$). However, as we will see below, state II has a σ_+-polarized peak. This is because the complex phase of the σ_+ matrix element (white vector field) has the opposite winding number, leading to the unusual behaviour that p-type states obtain a (small) oscillator strength in this spatial region.

Evolution with Twist-Angle

Finally, we investigate how the absorption spectrum changes for intra- and interlayer transitions, when we continuously vary the stacking angle. Figure 10.5 displays the calculated absorption spectra of intra- and interlayer excitons along with the interlayer degree of polarization for a range of relatively small twist-angles for the $MoSe_2/WSe_2$ bilayer. We find a large number of moiré resonances, whose number slowly decreases with increasing twist-angle. This results from a decreased momentum mixing between subbands s, whose detuning becomes larger as the size of the mBZ increases. Thereby the overall dipole strength of all peaks remains conserved and is distributed to fewer and fewer states as the angle increases.

The intriguing shift-behaviour of the moiré resonances, can be explained by distinguishing between two different moiré phases: i) moiré-localized states and ii) delocalized scattering states. For localized states with energies far below the unperturbed exciton (dashed lines), the peaks shift linearly with the twist-angle. With increasing twist-angles, the moiré period and therefore the confinement length is decreasing. This results in enhanced kinetic energies, leading to a linear increase of the ground state energy as well as the splitting between moiré-trapped resonances.

At some point, when a localized state is too close to the free particle energy, its wave function will overlap with neighboring moiré-cells and the exciton becomes mobile. In the second regime, the delocalized scattering states, we obtain quadratic shifts with the twist angle. This reflects the quadratic dispersion of the scattering states, because with increasing twist-angles the length of the mBZ grows ($\mathbf{g}_0 = \Delta\mathbf{G}$) and the intersection between zone-folded branches and the light cone at γ moves along the dispersion towards higher energies. Thereby, the intralayer exciton

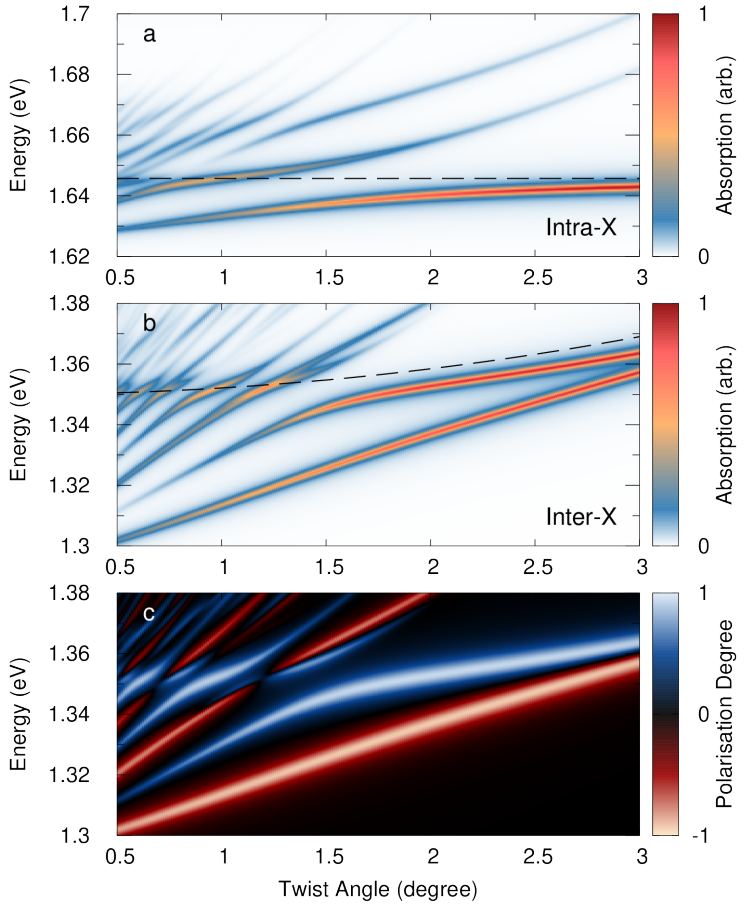

Figure 10.5: Absorption spectrum of **a** intra- and **b** interlayer excitons. Here the intralayer exciton spectrum is fully circularly polarized, while the interlayer moiré excitons exhibit an alternating degree of polarization, illustrated in **c**. Figure adopted from Paper 5.

resonance stops shifting at the energy of the unperturbed bright exciton resonance ($\mathbf{Q} = 0$). In contrast, the interlayer exciton is shifting further up in energy as its CoM dispersion is shifted away from the lightcone ($\mathbf{Q}_0^{\text{inter}} = \Delta K$).

Finally, the splitting between the two interlayer exciton peaks at angles $> 2.5°$ (A and B waves discussed in Fig. 10.3) is becoming smaller with the twist angle. This splitting is a measure for the depth of the effective excitonic moiré potential, discussed in Sec. 10.2. For long moiré periods the effective excitonic potential landscape is directly given by the band gap fluctuations $\mathcal{M} \approx V^c - V^v$. As the angle increases, the length scale of the moiré period becomes comparable with the exciton Bohr radius and the exciton starts to average over potential minima and maxima occupied by the excitonic orbital. Therefore the effective potential becomes shallower with increasing angles, which is reflected by the decreasing splitting in Fig. 10.5 for angles ¿2.5°.

With the presented approach we have gained insights into exciton localization and optics in the moiré of twisted van der Waals heterostructures. This will potentially guide future experimental and theoretical studies in this still very young field of research. In particular, the developed theoretical framework can be used to calculate material-specific interaction matrix elements (cf. Sec. 9.3), which allows us to model the spatiotemporal relaxation dynamics of moiré excitons.

CHAPTER 11

OUTLOOK AND CONCLUSION

In this work we have provided a quantitative and material-specific theoretical model of the exciton landscape in atomically-thin TMDs and provided microscopic insights into the exciton dynamics and optical response of these technologically promising materials. We have developed a microscopic model of the exciton-phonon and exciton-photon interaction for a large variety of exciton types and their impact on the excitation dynamics in TMD mono- and bilayers. In particular, we applied our models to explain and predict spectral features in several optical experiments. For the case of monolayer TMDs, our work provides insights into i) the broadening of excitonic resonances in linear absorption spectra including higher order (excited) exciton states, ii) the formation of side peaks in photoluminescence spectra resulting from phonon-assisted recombination of momentum-dark intervalley excitons and iii) we performed dynamical simulations to study the formation of bound excitons out of a free electron-hole gas. After this we showed how the exciton-light interaction is modified when two TMD monolayers are vertically stacked into homo- and heterobilayers. Here we describe the modifications of optical spectra in bilayer systems by controlling the stacking angle. In particular, we iv) show how the interlayer hybridization of momentum-dark excitons can be controlled through the stacking angle and v) investigate how the localization phase of moiré excitons can be tuned.

While the research focus of the 2D materials community has started to move from monolayer research towards stacked bilayer systems, there are still some open challenges in the fundamental theoretical description of excitons, even for the simple case of momentum direct excitons in a monolayer. For example, in this work we have been focusing on the low density limit, where excitons can be treated as effective point-like and non-interacting bosons. However, for increased densities

the Coulomb-induced scattering between excitons becomes important and introduces new aspects to the excitation dynamics, resulting from the competition of different scattering channels as well as dynamic energy renormalizations. In particular, the nature of an exciton, as a composite particle, has some interesting consequences on the exciton-exciton scattering characteristics compared to pure electron-electron scattering (Paper 30), which need to be further investigated in the future. In general, for all kinds of scattering mechanisms, it is interesting to ask which quantum statistics hold for excitons in the intermediate density regime. While excitons as compounds behave like bosons, their substructure consists of fermions, and it is an open question which character will dominate the quantum statistic at intermediate densities, i.e. stimulated transitions (bunching) vs. pauli-blocking (anti-bunching). For even higher densities excitons will dissociate due to an enhanced many-particle screening, also known as Mott transition. The transition regime between bound excitons and plasma and the dynamic conversion between these different phases is also not well understood, in particular when it comes to the temporal dynamics of such processes.
The microscopic approach developed in this work (and its precursors) provides an adequate theoretical foundation to investigate the exciton dynamics at low densities. In particular, the exciton-phonon scattering and the intervalley scattering channels highlighted in this thesis have been shown to be the dominant mechanisms in a large variety of optical experiments at low densities. In future works the acquired knowledge could be used to extend the modelling efforts towards spatiotemporal dynamics. In particular, the experimental design of dielectric and/or strain gradients enables the control of exciton transport, e.g., in order to funnel excitons into certain regions of an electronic device [139, 140].

When it comes to bilayers TMDs, the research field is still very young and the small pieces of knowledge provided in this work only represent a first step towards the understanding of the complex exciton physics. In particular, one of the most important and still widely unclear questions is which kind of exciton species is constituting the energetic ground states in different hetero-/homobilayers. From a theoretical viewpoint, it will be essential in the future to extend the efforts towards combining first principle methods with more simplified, effective models, such as the density matrix formalism presented in this work. Only a combination of these theory branches will provide insights into the excitonic structure of an arbitrary material combination, at arbitrary twist-angles and across the whole Brillouin zone, including momentum-/spin-direct and -indirect transitions, in order to find the energetically most favourable states and their properties. In particular, future studies should combine the two bilayer aspects studied in this work, i.e. hybridization in homobilayers and the electrostatic moiré potential used for the heterostructure. In most systems both effects will play a more or less strong role and their interplay might lead to interesting so far unknown effects.

Finally, it will of course also be beneficial to set up a numerical simulation of the

full exciton relaxation dynamics in a bilayer system, including scattering processes across differently hybridized valleys and moiré subbands. In particular, the spatiotemporal dynamics of excitons across moiré-trapped states and higher energy scattering states has not been investigated in literature yet, but plays a key role for the technological application of moiré lattices. The most challenging but probably also most rewarding problem is the dynamics of excitons/electrons inside a flat band. Here the build up of long ranged Coulomb correlations is pushing the limits of state of the art computational methods, but a sophisticated understanding of these strongly correlated systems might enable the intentional creation of exotic effects [141–144] such as the superconductivity in magic angle graphene [23, 24]. This work has contributed to a better understanding of the exciton dynamics in TMD mono- and bilayers and has helped to explain the observations in a large variety of experiments. Hopefully, it will also contribute to the development of more advanced theoretical models in the future that will help to decipher the secrets of moiré physics in twisted quantum materials.

ACKNOWLEDGMENTS

Finally, I cordially want to thank all the people who helped me to write this thesis.

First and foremost I thank my supervisor Ermin Malic, whose expertise was invaluable for the formulation of research questions and for the solution of problems. Your passion, farsightedness and the honest feedback pushed me to think out of the box and brought my work to a higher level.

I would like to acknowledge all my fellow PhD students and the postdocs in our work group, who have always been supportive and made Chalmers to a friendly place. In particular, I want to thank Malte Selig, who introduced me to the world of exciton physics in the beginning of my PhD studies. Without your insights and tips it would have been much more difficult to get on track. Also, I want to single out Ivan Bernal, Maja Feierabend and Raul Perea Causin, who always had an open ear and became much more than colleagues to me over the last years.

I would also like to thank my examiner Jari Kinaret and second supervisor Paul Erhart for their guidance throughout my studies.

In addition, I would like to thank my parents and my brother for their unwavering support and motivation. You are always there for me. Finally, I could not have finished this dissertation without the love and support of my fiance Lea Käbitz, who motivated me to keep fighting but also provided happy distractions to rest my mind.

BIBLIOGRAPHY

[1] Wei Han, Roland K Kawakami, Martin Gmitra, *et al.*: Graphene spintronics. *Nature Nanotechnology* 9(10), 794–807 (2014).

[2] John R Schaibley, Hongyi Yu, Genevieve Clark, *et al.*: Valleytronics in 2D materials. *Nature Reviews Materials* 1(11), 16055 (2016).

[3] Ruben Mas-Balleste, Cristina Gomez-Navarro, Julio Gomez-Herrero, *et al.*: 2D materials: to graphene and beyond. *Nanoscale* 3(1), 20–30 (2011).

[4] Sheneve Z. Butler, Shawna M. Hollen, Linyou Cao, *et al.*: Progress, Challenges, and Opportunities in Two-Dimensional Materials Beyond Graphene. *ACS Nano* 7(4), 2898–2926 (2013).

[5] Sajedeh Manzeli, Dmitry Ovchinnikov, Diego Pasquier, *et al.*: 2D transition metal dichalcogenides. *Nature Reviews Materials* 2(8), 17033 (2017).

[6] Kin Fai Mak, Changgu Lee, James Hone, *et al.*: Atomically Thin MoS_2: A New Direct-Gap Semiconductor. *Physical Review Letters* 105, 136805 (2010).

[7] Wang Qing Hua, Kalantar-Zadeh Kourosh, Kis Andras, *et al.*: Electronics and optoelectronics of two-dimensional transition metal dichalcogenides. *Nature Nanotechnology* 7(11), 699–712 (2012). ISSN 1748-3387.

[8] Andreas Pospischil, Thomas Mueller: Optoelectronic devices based on atomically thin transition metal dichalcogenides. *Applied Sciences* 6(3), 78 (2016).

[9] Kin Fai Mak, Jie Shan: Photonics and optoelectronics of 2D semiconductor transition metal dichalcogenides. *Nature Photonics* 10(4), 216–226 (2016).

[10] Thomas Mueller, Ermin Malic: Exciton physics and device application of two-dimensional transition metal dichalcogenide semiconductors. *npj 2D Materials and Applications* 2(1), 29 (2018).

[11] Gang Wang, Alexey Chernikov, Mikhail M Glazov, *et al.*: Colloquium: Excitons in atomically thin transition metal dichalcogenides. *Reviews of Modern Physics* 90(2), 021001 (2018).

[12] Branimir Radisavljevic, Aleksandra Radenovic, Jacopo Brivio, *et al.*: Single-layer MoS_2 transistors. *Nature Nanotechnology* 6(3), 147 (2011).

[13] Ashwin Ramasubramaniam: Large excitonic effects in monolayers of molybdenum and tungsten dichalcogenides. *Physical Review B* 86(11), 115409 (2012).

[14] Keliang He, Nardeep Kumar, Liang Zhao, *et al.*: Tightly bound excitons in monolayer WSe_2. *Physical Review Letters* 113(2), 026803 (2014).

[15] Miguel M Ugeda, Aaron J Bradley, Su-Fei Shi, *et al.*: Giant bandgap renormalization and excitonic effects in a monolayer transition metal dichalcogenide semiconductor. *Nature Materials* 13(12), 1091 (2014).

[16] Alexey Chernikov, Timothy C Berkelbach, Heather M Hill, *et al.*: Exciton binding energy and nonhydrogenic Rydberg series in monolayer WS_2. *Physical Review Letters* 113(7), 076802 (2014).

[17] Heather M Hill, Albert F Rigosi, Cyrielle Roquelet, *et al.*: Observation of excitonic Rydberg states in monolayer MoS_2 and WS_2 by photoluminescence excitation spectroscopy. *Nano Letters* 15(5), 2992–2997 (2015).

[18] A Steinhoff, J-H Kim, F Jahnke, *et al.*: Efficient excitonic photoluminescence in direct and indirect band gap monolayer MoS_2. *Nano Letters* 15(10), 6841–6847 (2015).

[19] Andreas V Stier, Nathan P Wilson, Kirill A Velizhanin, *et al.*: Magnetooptics of Exciton Rydberg States in a Monolayer Semiconductor. *Physical Review Letters* 120(5), 057405 (2018).

[20] C Robert, MA Semina, F Cadiz, *et al.*: Optical spectroscopy of excited exciton states in MoS_2 monolayers in van der Waals heterostructures. *Physical Review Materials* 2(1), 011001 (2018).

[21] Christoph Pöllmann, P Steinleitner, U Leierseder, *et al.*: Resonant internal quantum transitions and femtosecond radiative decay of excitons in monolayer WSe_2. *Nature Materials* 14(9), 889–893 (2015).

[22] Andre K Geim, Irina V Grigorieva: Van der Waals heterostructures. *Nature* 499(7459), 419–425 (2013).

[23] Yuan Cao, Valla Fatemi, Shiang Fang, *et al.*: Unconventional superconductivity in magic-angle graphene superlattices. *Nature* 556(7699), 43–50 (2018).

[24] Rafi Bistritzer, Allan H MacDonald: Moiré bands in twisted double-layer graphene. *Proceedings of the National Academy of Sciences* 108(30), 12233–12237 (2011).

[25] Pasqual Rivera, John R Schaibley, Aaron M Jones, *et al.*: Observation of long-lived interlayer excitons in monolayer $MoSe_2$–WSe_2 heterostructures. *Nature Communications* 6(1), 1–6 (2015).

[26] Bastian Miller, Alexander Steinhoff, Borja Pano, *et al.*: Long-lived direct and indirect interlayer excitons in van der Waals heterostructures. *Nano Letters* 17(9), 5229–5237 (2017).

[27] Pasqual Rivera, Hongyi Yu, Kyle L Seyler, *et al.*: Interlayer valley excitons in heterobilayers of transition metal dichalcogenides. *Nature Nanotechnology* 13(11), 1004–1015 (2018).

[28] Jens Kunstmann, Fabian Mooshammer, Philipp Nagler, *et al.*: Momentum-space indirect interlayer excitons in transition-metal dichalcogenide van der Waals heterostructures. *Nature Physics* 14(8), 801–805 (2018).

[29] P Merkl, F Mooshammer, P Steinleitner, *et al.*: Ultrafast transition between exciton phases in van der Waals heterostructures. *Nature Materials* p. 1 (2019).

[30] Hongyi Yu, Gui-Bin Liu, Jianju Tang, *et al.*: Moiré excitons: From programmable quantum emitter arrays to spin-orbit–coupled artificial lattices. *Science Advances* 3(11), e1701696 (2017).

[31] Nan Zhang, Alessandro Surrente, Michał Baranowski, *et al.*: Moiré intralayer excitons in a $MoSe_2/MoS_2$ heterostructure. *Nano Letters* 18(12), 7651–7657 (2018).

[32] Chenhao Jin, Emma C Regan, Aiming Yan, *et al.*: Observation of moiré excitons in WSe_2/WS_2 heterostructure superlattices. *Nature* 567(7746), 76–80 (2019).

[33] Kha Tran, Galan Moody, Fengcheng Wu, *et al.*: Evidence for moiré excitons in van der Waals heterostructures. *Nature* 567(7746), 71–75 (2019).

[34] Kyle L Seyler, Pasqual Rivera, Hongyi Yu, *et al.*: Signatures of moiré-trapped valley excitons in $MoSe_2/WSe_2$ heterobilayers. *Nature* 567(7746), 66–70 (2019).

[35] Evgeny M Alexeev, David A Ruiz-Tijerina, Mark Danovich, *et al.*: Resonantly hybridized excitons in moiré superlattices in van der Waals heterostructures. *Nature* 567(7746), 81–86 (2019).

[36] Fausto Rossi, Tilmann Kuhn: Theory of ultrafast phenomena in photoexcited semiconductors. *Reviews of Modern Physics* 74(3), 895 (2002).

[37] M Kira, SW Koch: Many-body correlations and excitonic effects in semiconductor spectroscopy. *Progress in Quantum Electronics* 30(5), 155–296 (2006).

[38] V M Axt, T Kuhn: Femtosecond spectroscopy in semiconductors: a key to coherences, correlations and quantum kinetics. *Reports on Progress in Physics* 67(4), 433 (2004).

[39] Hartmut Haug, Stephan W Koch: *Quantum theory of the optical and electronic properties of semiconductors: fivth edition*. World Scientific Publishing Company (2009).

[40] Gerald D Mahan: *Many-particle physics*. Springer Science & Business Media (2013).

[41] Paul Adrien Maurice Dirac: *The principles of quantum mechanics*. 27. Oxford University Press (1981).

[42] Edward G Harris: *A pedestrian approach to quantum field theory*. Courier Corporation (2014).

[43] Werner Vogel, Dirk-Gunnar Welsch: *Quantum optics*. John Wiley & Sons (2006).

[44] M Lindberg, Stephan W Koch: Effective Bloch equations for semiconductors. *Physical Review B* 38(5), 3342 (1988).

[45] Jens Fricke: Transport equations including many-particle correlations for an arbitrary quantum system: A general formalism. *Annals of Physics* 252(2), 479–498 (1996).

[46] Mackillo Kira, Stephan W Koch: *Semiconductor quantum optics*. Cambridge University Press (2011).

[47] Ermin Malic, Andreas Knorr: *Graphene and carbon nanotubes: ultrafast optics and relaxation dynamics*. John Wiley & Sons (2013).

[48] Filip A Rasmussen, Kristian S Thygesen: Computational 2D materials database: electronic structure of transition-metal dichalcogenides and oxides. *The Journal of Physical Chemistry C* 119(23), 13169–13183 (2015).

[49] Andor Kormányos, Guido Burkard, Martin Gmitra, *et al.*: k· p theory for two-dimensional transition metal dichalcogenide semiconductors. *2D Materials* 2(2), 022001 (2015).

[50] Wang Yao, Di Xiao, Qian Niu: Valley-dependent optoelectronics from inversion symmetry breaking. *Physical Review B* 77, 235406 (2008).

[51] Zeng Hualing, Dai Junfeng, Yao Wang, *et al.*: Valley polarization in MoS_2 monolayers by optical pumping. *Nature Nanotechnology* 7(8), 490–493 (2012). ISSN 1748-3387.

[52] Cao, Ting, Wang, Gang, Han, Wenpeng, *et al.*: Valley-selective circular dichroism of monolayer molybdenum disulphide. *Nature Communications* 3, 887 (2012).

[53] Xu Xiaodong, Yao Wang, Xiao Di, *et al.*: Spin and pseudospins in layered transition metal dichalcogenides. *Nature Physics* 10(5), 343–350 (2014). ISSN 1745-2473.

[54] T. Yu, M. W. Wu: Valley depolarization due to intervalley and intravalley electron-hole exchange interactions in monolayer MoS_2. *Physical Review B* 89, 205303 (2014).

[55] Selig, Malte, Berghäuser, Gunnar, Raja, Archana, *et al.*: Excitonic linewidth and coherence lifetime in monolayer transition metal dichalcogenides. *Nature Communications* 7, 13279 (2016).

[56] Dominik Christiansen, Malte Selig, Gunnar Berghäuser, *et al.*: Phonon Sidebands in Monolayer Transition Metal Dichalcogenides. *Physical Review Letters* 119(18), 187402 (2017).

[57] Maja Feierabend, Gunnar Berghäuser, Andreas Knorr, *et al.*: Proposal for dark exciton based chemical sensors. *Nature Communications* 8 (2017).

[58] Iris Niehues, Robert Schmidt, Matthias Druppel, *et al.*: Strain Control of Exciton–Phonon Coupling in Atomically Thin Semiconductors. *Nano Letters* 18(3), 1751–1757 (2018).

[59] Malte Selig, Gunnar Berghäuser, Marten Richter, *et al.*: Dark and bright exciton formation, thermalization, and photoluminescence in monolayer transition metal dichalcogenides. *2D Materials* 5(3), 035017 (2018).

[60] E Cappelluti, Rafael Roldán, JA Silva-Guillén, *et al.*: Tight-binding model and direct-gap/indirect-gap transition in single-layer and multilayer MoS_2. *Physical Review B* 88(7), 075409 (2013).

[61] Rafael Roldán, Jose A Silva-Guillén, M Pilar López-Sancho, *et al.*: Electronic properties of single-layer and multilayer transition metal dichalcogenides MX_2 (M= Mo, W and X= S, Se). *Annalen der Physik* 526(9-10), 347–357 (2014).

[62] Yong Wang, Zhan Wang, Wang Yao, *et al.*: Interlayer coupling in commensurate and incommensurate bilayer structures of transition-metal dichalcogenides. *Physical Review B* 95(11), 115429 (2017).

[63] Di Xiao, Gui-Bin Liu, Wanxiang Feng, *et al.*: Coupled spin and valley physics in monolayers of MoS_2 and other group-VI dichalcogenides. *Physical Review Letters* 108(19), 196802 (2012).

[64] Johannes Steiner: *Microscopic Theory of Linear and Nonlinear Terahertz Spectroscopy of Semiconductors*. Ph.D. thesis, Philipps-University Marburg (2008).

[65] Pierluigi Cudazzo, Ilya V. Tokatly, Angel Rubio: Dielectric screening in two-dimensional insulators: Implications for excitonic and impurity states in graphane. *Physical Review B* 84, 085406 (2011).

[66] Simone Latini, Thomas Olsen, Kristian Sommer Thygesen: Excitons in van der Waals heterostructures: The important role of dielectric screening. *Physical Review B* 92(24), 245123 (2015).

[67] Alexey Chernikov, Timothy C. Berkelbach, Heather M. Hill, *et al.*: Exciton Binding Energy and Nonhydrogenic Rydberg Series in Monolayer WS_2. *Physical Review Letters* 113, 076802 (2014).

[68] Natalia S Rytova: Screened potential of a point charge in a thin film. *arXiv preprint arXiv:1806.00976* (2018).

[69] LV Keldysh: Coulomb interaction in thin semiconductor and semimetal films. *JETPL* 29, 658 (1979).

[70] Akash Laturia, Maarten L Van de Put, William G Vandenberghe: Dielectric properties of hexagonal boron nitride and transition metal dichalcogenides: from monolayer to bulk. *npj 2D Materials and Applications* 2(1), 6 (2018).

[71] Zhenghe Jin, Xiaodong Li, Jeffrey T Mullen, *et al.*: Intrinsic transport properties of electrons and holes in monolayer transition-metal dichalcogenides. *Physical Review B* 90(4), 045422 (2014).

[72] Kristen Kaasbjerg, Kristian S Thygesen, Antti-Pekka Jauho: Acoustic phonon limited mobility in two-dimensional semiconductors: Deformation potential and piezoelectric scattering in monolayer MoS 2 from first principles. *Physical Review B* 87(23), 235312 (2013).

[73] J Bardeen, W Shockley: Deformation potentials and mobilities in non-polar crystals. *Physical Review* 80(1), 72 (1950).

[74] Hartwin Peelaers, Chris G Van de Walle: Effects of strain on band structure and effective masses in MoS_2. *Physical Review B* 86(24), 241401 (2012).

[75] Alexey Chernikov, Claudia Ruppert, Heather M Hill, *et al.*: Population inversion and giant bandgap renormalization in atomically thin WS_2 layers. *Nature Photonics* 9(7), 466 (2015).

[76] Paul D Cunningham, Aubrey T Hanbicki, Kathleen M McCreary, *et al.*: Photoinduced bandgap renormalization and exciton binding energy reduction in WS_2. *ACS Nano* 11(12), 12601–12608 (2017).

[77] A Steinhoff, M Rosner, F Jahnke, *et al.*: Influence of excited carriers on the optical and electronic properties of MoS_2. *Nano Letters* 14(7), 3743–3748 (2014).

[78] SW Koch, M Kira, G Khitrova, *et al.*: Semiconductor excitons in new light. *Nature Materials* 5(7), 523–531 (2006).

[79] Gunnar Berghäuser, Ermin Malic: Analytical approach to excitonic properties of MoS_2. *Physical Review B* 89, 125309 (2014).

[80] A Thränhardt, S Kuckenburg, A Knorr, *et al.*: Quantum theory of phonon-assisted exciton formation and luminescence in semiconductor quantum wells. *Physical Review B* 62(4), 2706 (2000).

[81] A Knorr, S Hughes, T Stroucken, *et al.*: Theory of ultrafast spatio-temporal dynamics in semiconductor heterostructures. *Chemical Physics* 210(1-2), 27–47 (1996).

[82] Archana Raja, Andrey Chaves, Jaeeun Yu, *et al.*: Coulomb engineering of the bandgap and excitons in two-dimensional materials. *Nature Communications* 8, 15251 (2017).

[83] Akshay Singh, Andreas Knorr, Chandriker Kavir Dass, *et al.*: Intrinsic homogeneous linewidth and broadening mechanisms of excitons in monolayer transition metal dichalcogenides. *Nature Communications* 6, 8315 (2015).

[84] Maurizia Palummo, Marco Bernardi, Jeffrey C Grossman: Exciton radiative lifetimes in two-dimensional transition metal dichalcogenides. *Nano Letters* 15(5), 2794–2800 (2015).

[85] Prasenjit Dey, Jagannath Paul, Zefang Wang, *et al.*: Optical coherence in atomic-monolayer transition-metal dichalcogenides limited by electron-phonon interactions. *Physical Review Letters* 116(12), 127402 (2016).

[86] Zahra Khatibi, Maja Feierabend, Malte Selig, *et al.*: Impact of strain on the excitonic linewidth in transition metal dichalcogenides. *2D Materials* 6(1), 015015 (2018).

[87] Tomasz Kazimierczuk, Dietmar Fröhlich, Stefan Scheel, *et al.*: Giant Rydberg excitons in the copper oxide Cu_2O. *Nature* 514(7522), 343 (2014).

[88] Heinrich Stolz, Florian Schöne, Dirk Semkat: Interaction of Rydberg excitons in cuprous oxide with phonons and photons: optical linewidth and polariton effect. *New Journal of Physics* 20(2), 023019 (2018).

[89] Yutaka Toyozawa: Theory of line-shapes of the exciton absorption bands. *Progress of Theoretical Physics* 20(1), 53–81 (1958).

[90] Hartmut Haug, Stefan Schmitt-Rink: Electron theory of the optical properties of laser-excited semiconductors. *Progress in Quantum Electronics* 9(1), 3–100 (1984).

[91] AL Ivanov, H Haug: Self-consistent theory of the biexciton optical nonlinearity. *Physical Review B* 48(3), 1490 (1993).

[92] Florian Katsch, Malte Selig, Alexander Carmele, *et al.*: Theory of Exciton–Exciton Interactions in Monolayer Transition Metal Dichalcogenides. *Physica Status Solidi B* 255(12), 1800185 (2018).

[93] Florian Katsch, Malte Selig, Andreas Knorr: Exciton-scattering-induced dephasing in two-dimensional semiconductors. *Physical Review Letters* 124(25), 257402 (2020).

[94] Xiao-Xiao Zhang, Yumeng You, Shu Yang Frank Zhao, *et al.*: Experimental evidence for dark excitons in monolayer WSe_2. *Physical Review Letters* 115(25), 257403 (2015).

[95] Thorsten Deilmann, Kristian Sommer Thygesen: Finite-momentum exciton landscape in mono-and bilayer transition metal dichalcogenides. *2D Materials* (2019).

[96] M Kira, F Jahnke, SW Koch: Microscopic theory of excitonic signatures in semiconductor photoluminescence. *Physical Review Letters* 81(15), 3263 (1998).

[97] M Kira, F Jahnke, W Hoyer, *et al.*: Quantum theory of spontaneous emission and coherent effects in semiconductor microstructures. *Progress in Quantum Electronics* 23(6), 189–279 (1999).

[98] Walter Hoyer: *Quantentheorie zu Exzitonbildung und Photolumineszenz in Halbleitern*. Ph.D. thesis, Philipps-University Marburg (2002).

[99] Philipp Tonndorf, Robert Schmidt, Philipp Böttger, *et al.*: Photoluminescence emission and Raman response of monolayer MoS_2, $MoSe_2$, and WSe_2. *Optics Express* 21(4), 4908–4916 (2013).

[100] Haining Wang, Changjian Zhang, Weimin Chan, *et al.*: Radiative lifetimes of excitons and trions in monolayers of the metal dichalcogenide MoS_2. *Physical Review B* 93(4), 045407 (2016).

[101] T Feldtmann, M Kira, Stephan W Koch: Phonon sidebands in semiconductor luminescence. *Physica Status Solidi B* 246(2), 332–336 (2009).

[102] T Feldtmann, M Kira, Stephan W Koch: Theoretical analysis of higher-order phonon sidebands in semiconductor luminescence spectra. *Journal of Luminescence* 130(1), 107–113 (2010).

[103] A Chernikov, V Bornwasser, M Koch, *et al.*: Phonon-assisted luminescence of polar semiconductors: Fröhlich coupling versus deformation-potential scattering. *Physical Review B* 85(3), 035201 (2012).

[104] Jessica Lindlau, Malte Selig, Andre Neumann, *et al.*: The role of momentum-dark excitons in the elementary optical response of bilayer WSe_2. *Nature Communications* 9(1), 2586 (2018).

[105] Jessica Lindlau, Cedric Robert, Victor Funk, *et al.*: Identifying optical signatures of momentum-dark excitons in transition metal dichalcogenide monolayers. *arXiv preprint arXiv:1710.00988* (2017).

[106] E Courtade, M Semina, M Manca, *et al.*: Charged excitons in monolayer WSe_2: experiment and theory. *Physical Review B* 96(8), 085302 (2017).

[107] Ziliang Ye, Lutz Waldecker, Eric Yue Ma, *et al.*: Efficient generation of neutral and charged biexcitons in encapsulated WSe_2 monolayers. *Nature Communications* 9(1), 3718 (2018).

[108] Matteo Barbone, Alejandro R-P Montblanch, Dhiren M Kara, *et al.*: Charge-tuneable biexciton complexes in monolayer WSe_2. *Nature Communications* 9(1), 3721 (2018).

[109] Kin Fai Mak, Keliang He, Changgu Lee, *et al.*: Tightly bound trions in monolayer MoS_2. *Nature Materials* 12(3), 207 (2013).

[110] Gerd Plechinger, Philipp Nagler, Julia Kraus, *et al.*: Identification of excitons, trions and biexcitons in single-layer WS_2. *Physica Status Solidi RRL* 9(8), 457–461 (2015).

[111] Tobias Korn, Stefanie Heydrich, Michael Hirmer, *et al.*: Low-temperature photocarrier dynamics in monolayer MoS_2. *Applied Physics Letters* 99(10), 102109 (2011).

[112] Philipp Tonndorf, Robert Schmidt, Robert Schneider, *et al.*: Single-photon emission from localized excitons in an atomically thin semiconductor. *Optica* 2(4), 347–352 (2015).

[113] Dinh Van Tuan, Aaron M Jones, Min Yang, *et al.*: Virtual trions in the photoluminescence of monolayer transition-metal dichalcogenides. *Physical Review Letters* 122(21), 217401 (2019).

[114] Zhipeng Li, Tianmeng Wang, Chenhao Jin, *et al.*: Momentum-dark intervalley exciton in monolayer tungsten diselenide brightened via chiral phonon. *ACS Nano* 13(12), 14107–14113 (2019).

[115] Minhao He, Pasqual Rivera, Dinh Van Tuan, *et al.*: Valley phonons and exciton complexes in a monolayer semiconductor. *Nature Communications* 11(1), 1–7 (2020).

[116] K Siantidis, VM Axt, T Kuhn: Dynamics of exciton formation for near band-gap excitations. *Physical Review B* 65(3), 035303 (2001).

[117] Robert A Kaindl, Marc A Carnahan, D Hägele, *et al.*: Ultrafast terahertz probes of transient conducting and insulating phases in an electron–hole gas. *Nature* 423(6941), 734–738 (2003).

[118] Mackillo Kira, Walter Hoyer, Stephan W Koch: Microscopic theory of the semiconductor terahertz response. *Physica Status Solidi B* 238(3), 443–450 (2003).

[119] M Kira, W Hoyer, SW Koch: Terahertz signatures of the exciton formation dynamics in non-resonantly excited semiconductors. *Solid State Communications* 129(11), 733–736 (2004).

[120] JT Steiner, M Kira, Stephan W Koch: Optical nonlinearities and Rabi flopping of an exciton population in a semiconductor interacting with strong terahertz fields. *Physical Review B* 77(16), 165308 (2008).

[121] Soonyoung Cha, Ji Ho Sung, Sangwan Sim, *et al.*: 1s-intraexcitonic dynamics in monolayer MoS_2 probed by ultrafast mid-infrared spectroscopy. *Nature Communications* 7, 10768 (2016).

[122] Philipp Steinleitner, Philipp Merkl, Philipp Nagler, *et al.*: Direct Observation of Ultrafast Exciton Formation in a Monolayer of WSe_2. *Nano Letters* 17(3), 1455–1460 (2017).

[123] Simon Ovesen: *Modeling of interlayer excitons in van der Waals heterostructures*. Master's thesis, Chalmers University of Technology (2017).

[124] Simon Ovesen, Samuel Brem, Christopher Linderälv, *et al.*: Interlayer exciton dynamics in van der Waals heterostructures. *Communications Physics* 2(1), 1–8 (2019).

[125] Arend M van der Zande, Jens Kunstmann, Alexey Chernikov, *et al.*: Tailoring the electronic structure in bilayer molybdenum disulfide via interlayer twist. *Nano Letters* 14(7), 3869–3875 (2014).

[126] Horacio Coy Diaz, Jose Avila, Chaoyu Chen, *et al.*: Direct observation of interlayer hybridization and Dirac relativistic carriers in graphene/MoS_2 van der Waals heterostructures. *Nano Letters* 15(2), 1135–1140 (2015).

[127] Po-Chun Yeh, Wencan Jin, Nader Zaki, *et al.*: Direct measurement of the tunable electronic structure of bilayer MoS_2 by interlayer twist. *Nano Letters* 16(2), 953–959 (2016).

[128] Hui Fang, Corsin Battaglia, Carlo Carraro, *et al.*: Strong interlayer coupling in van der Waals heterostructures built from single-layer chalcogenides. *Proceedings of the National Academy of Sciences* 111(17), 6198–6202 (2014).

[129] Jonas Kiemle, Florian Sigger, Michael Lorke, *et al.*: Control of the orbital character of indirect excitons in MoS_2/WS_2 heterobilayers. *Physical Review B* 101(12), 121404 (2020).

[130] David A Ruiz-Tijerina, Vladimir I Fal'ko: Interlayer hybridization and moiré superlattice minibands for electrons and excitons in heterobilayers of transition-metal dichalcogenides. *Physical Review B* 99(12), 125424 (2019).

[131] Chenhao Jin, Eric Yue Ma, Ouri Karni, *et al.*: Ultrafast dynamics in van der Waals heterostructures. *Nature Nanotechnology* 13(11), 994–1003 (2018).

[132] Fengcheng Wu, Timothy Lovorn, Allan H MacDonald: Topological exciton bands in moiré heterojunctions. *Physical Review Letters* 118(14), 147401 (2017).

[133] Fengcheng Wu, Timothy Lovorn, Emanuel Tutuc, *et al.*: Hubbard model physics in transition metal dichalcogenide moiré bands. *Physical Review Letters* 121(2), 026402 (2018).

[134] Roland Gillen, Janina Maultzsch: Interlayer excitons in $MoSe_2$/WSe_2 heterostructures from first principles. *Physical Review B* 97(16), 165306 (2018).

[135] Xiaobo Lu, Xiaoqin Li, Li Yang: Modulated interlayer exciton properties in a two-dimensional moiré crystal. *Physical Review B* 100(15), 155416 (2019).

[136] Chendong Zhang, Chih-Piao Chuu, Xibiao Ren, *et al.*: Interlayer couplings, Moiré patterns, and 2D electronic superlattices in MoS_2/WSe_2 heterobilayers. *Science Advances* 3(1), e1601459 (2017).

[137] Fengcheng Wu, Timothy Lovorn, AH MacDonald: Theory of optical absorption by interlayer excitons in transition metal dichalcogenide heterobilayers. *Physical Review B* 97(3), 035306 (2018).

[138] Hongyi Yu, Yong Wang, Qingjun Tong, *et al.*: Anomalous light cones and valley optical selection rules of interlayer excitons in twisted heterobilayers. *Physical Review Letters* 115(18), 187002 (2015).

[139] Menghao Wu, Xiaofeng Qian, Ju Li: Tunable exciton funnel using moiré superlattice in twisted van der waals bilayer. *Nano Letters* 14(9), 5350–5357 (2014).

[140] Hyowon Moon, Gabriele Grosso, Chitraleema Chakraborty, *et al.*: Dynamic exciton funneling by local strain control in a monolayer semiconductor. *arXiv preprint arXiv:1906.10077* (2019).

[141] Liu Zheng, Liu Feng, Wu Yong-Shi: Exotic electronic states in the world of flat bands: From theory to material. *Chinese Physics B* 23(7), 077308 (2014).

[142] Lei Wang, En-Min Shih, Augusto Ghiotto, *et al.*: Correlated electronic phases in twisted bilayer transition metal dichalcogenides. *Nature Materials* pp. 1–6 (2020).

[143] Liheng An, Xiangbin Cai, Ding Pei, *et al.*: Interaction effects and superconductivity signatures in twisted double-bilayer WSe_2. *Nanoscale Horizons* 5(9), 1309–1316 (2020).

[144] Zhiming Zhang, Yimeng Wang, Kenji Watanabe, *et al.*: Flat bands in twisted bilayer transition metal dichalcogenides. *Nature Physics* pp. 1–4 (2020).